

12-2017

Materials Properties of the Lepidopteran Proboscis and a Bio-Inspired Characterization Method of Capillary Adhesion

Luke Michael Sande
Clemson University

Follow this and additional works at: https://tigerprints.clemson.edu/all_theses

Recommended Citation

Sande, Luke Michael, "Materials Properties of the Lepidopteran Proboscis and a Bio-Inspired Characterization Method of Capillary Adhesion" (2017). *All Theses*. 2770.
https://tigerprints.clemson.edu/all_theses/2770

This Thesis is brought to you for free and open access by the Theses at TigerPrints. It has been accepted for inclusion in All Theses by an authorized administrator of TigerPrints. For more information, please contact kokeefe@clemson.edu.

MATERIALS PROPERTIES OF THE LEPIDOPTERAN PROBOSCIS AND A
BIO-INSPIRED CHARACTERIZATION METHOD OF CAPILLARY ADHESION

A Thesis
Presented to
the Graduate School of
Clemson University

In Partial Fulfillment
of the Requirements for the Degree
Master of Science
Materials Science and Engineering

by
Luke Michael Sande
December 2017

Accepted by:
Dr. Konstantin G. Kornev, Committee Chair
Dr. Olga Kuksenok
Dr. Peter Adler

ABSTRACT

The feeding device of butterflies and moths, Lepidoptera, is called the “proboscis” and it consists of two complex-shaped fibers, galeae, which get linked together when the insects emerge from the pupa. The proboscis has been extensively studied by biologists, but has never been investigated from the materials science point of view. The following questions remain to be answered: What are the materials properties of the proboscis? How does the proboscis assemble and repair and what role do capillary forces play? What are the adhesion forces holding the galeae together during this assembly process?

We have investigated and are exhibiting a methodology for studying the self-assembly and self-repair mechanism of the split lepidopteran proboscis in active and sedated butterflies. The proposed method can be extended to a bio-inspired characterization method of capillary adhesion for use with other samples. To probe the repair capabilities, we have separated the proboscis far from the head with a metal post of diameter comparable to the butterfly galea and moved the post ever closer to the head in increments of 500 microns until the proboscis was fully split. Once split, we brought the post back towards the tip in steps and observed the convergence of the two galeae back into one united proboscis. To determine the materials properties of the proboscis, the process of galeae gathering was filmed with a high speed camera. The galea profile, extracted from each frame of the videos, was then fitted with a mathematical model based on the Euler-Bernoulli beam theory where each galea was treated as a beam undergoing small deflections. The theory was augmented by introducing the bending moments modeling the muscular action and by a capillary force due to the saliva meniscus.

Experiments on sedated butterflies, when the muscular action was diminished but saliva was present, show the crucial role of the saliva meniscus in bringing galeae together. The model sheds light on the evolutionary development of the butterfly proboscis.

ACKNOWLEDGMENTS

We would like to acknowledge the National Science Foundation (NSF) for their continued support on these works. This project was funded by NSF Projects: *POL-S1305338 and IOS-1354956*.

This research was also supported in part by an appointment to the Student Research Participation Program at the U.S. Air Force Civil Engineering Center (AFCEC) administered by the Oak Ridge Institute for Science and Education (ORISE) through interagency agreement between the U.S. Department of Energy and AFCEC.

Furthermore, I would like to acknowledge the following people: Dr. Kornev and the Kornev group members, Pavel Aprelev and Chengqi Zhang, who have helped me every step of the way during the course of my graduate school career; all of the Clemson undergraduate students, Allison Kaczmarek, Alex Chernyk, and Madisen Weaver (a Research Experiences for Undergrads (REU) summer student from Texas State University) who assisted in data collection for my thesis; collaborators from the Department of Plant & Environmental Sciences at Clemson University, Dr. Peter Adler, Dr. Charles (Eddie) Beard, and Suellen Pometto; and the MS&E Director of Analytical Services, Kim Ivey, for all of the help with dynamic mechanical analysis of the butterfly proboscises.

TABLE OF CONTENTS

	Page
TITLE PAGE	i
ABSTRACT.....	ii
ACKNOWLEDGMENTS	iv
LIST OF TABLES	vii
LIST OF FIGURES	ix
CHAPTER	
I. INTRODUCTION	1
1.1 Principles of Adhesion.....	1
1.2 The Peel Test.....	4
1.3 Introduction to Lepidoptera: The Butterfly Proboscis	9
II. RESEARCH OBJECTIVE	13
2.1 Motivation of Study	13
2.2 Bio-Inspired Adhesion Characterization Method	13
III. RESEARCH METHODOLOGY.....	17
3.1 Splitting of the Butterfly Proboscis.....	17
3.2 Data Acquisition and Analysis.....	42
IV. RESULTS AND DISCUSSION.....	51
4.1 Materials Properties of the Butterfly Proboscis	51
V. CONCLUSIONS.....	68

Table of Contents (Continued)

	Page
VI. SIGNIFICANCE OF WORK	71
6.1 Reference Adhesion Experiment Using Ribbons of Well Characterized Materials	71
APPENDICES	79
A: Table of Collected Data	80
B: Glossary of Parameters	81
C: DMA Data.....	83
D: Wolfram Mathematica® Code.....	84
E: Integration Constants for Solutions to Differential Equations.....	94
F: National Instruments LabVIEW® Code.....	96
REFERENCES	105

LIST OF TABLES

Table		Page
1	<p>Ranges of usable γ values when changing parameters B and L, or the crack length, are shown by n1/n2 in the table; any B-L pairs where waves always propagate in our solution are unusable and are shown by the red blocks in the table. This table can be read as follows: for a certain B-L pair, we have n1/n2 in the table and the n1, or number before the backslash, is the first γ value that can be used for this pair. Similarly, n2, or the number after the backslash, is the largest value that can be used for this pair. These $\gamma=n1$ and $\gamma=n2$ values were found by plugging the designated B and L values into our solution, setting the meniscus length, or length of the wet region, equal to the length of the crack L, and then searching through γ values until profiles matching our physical case were found. If the profile dipped below the axis of symmetry (shown by the dotted line in Figures 4 and 5) at any point, then we couldn't use that γ value. Additionally, if waves start to propagate in our solution for a certain γ, then we also cannot use this γ value. This table was made for $\theta = \pi/2$ and values are subject to change for other θ values. The cells in green display that for different B-L pairs corresponding to different fiber shapes, lengths, and rigidities, ranges of gamma values can remain similar. Therefore, in our data fitting we have used $\gamma=0.62$ which seems to fit the most fiber types.</p>	33
2	<p>B values (data shown in Figure 17) collected for each butterfly with their corresponding standard deviations. The standard deviations were found by considering each video and taking measurements of B frame by frame. In this data set, 6 Monarchs and 5 Painted Ladies were tested to make up the 8 and 10 videos tested for each species, respectively. All other collected data can be found in the appendices.</p>	57

List of Tables (Continued)

Table	Page
3 The Modulus of Elasticity, E, values calculated from equation [30] with average B values for each butterfly species tested. The column indicated 'Average' is calculated with the Average B value for each species whereas the 'Low Estimate' and 'High Estimate' are calculated with the upper and lower B values that would be found based on our standard deviation respectively. For further clarification, higher B values lead to lower E values.....	59
4 Comparison between the Modulus of Elasticity E values found from the theoretical curve fitting and the mechanical testing after calculating the moment of inertia with parameter values for Rg1, Rg2, and h found near the middle of the proboscis. Values for these parameters can be found in Table 5. This table shows that when using shape estimates for the galeae near the middle of the proboscis instead of the tip, we find much better agreement between our theory and mechanical experiments in both the averages and the lower and upper bounds (when using one standard deviation to calculate them).	62
5 Tabulated parameters used in modulus of elasticity E calculations where the symbol is shown in parenthesis and the corresponding units are shown in brackets.	63
6 Contact angle measurements on the surface of treated tungsten wires.	78

LIST OF FIGURES

Figure		Page
1	Energy model of the peel test where P is the pulling force at angle θ from the substrate. da is the length that the film debonded from the surface, b is the width of the film, and h is the thickness of the film.	6
2	Force model of the peel test where P is the pulling force at angle θ from the substrate and F_{adx} and F_{ady} are the resisting forces in the x and y directions respectively. Additionally, b and h are the width and thickness of the film, respectively.....	8
3	a) Scanning Electron Microscope (SEM) image of the butterfly proboscis in the coiled state, b) the cross section, and c) the single galea curled up. These images were taken from (43). d) A cross section of a single galea where the white circular tube is the trachea, and the semi-circular cut-out at the top is one half of the food canal. e) Displays the emergence from the pupa, or ‘eclosion’, and that the two galeae are separated at this moment and come together with a series of coiling-uncoiling motions along with saliva pumping (courtesy of D. Monaenkova).	11

List of Figures (Continued)

Figure		Page
4	Experimental Schematic for the adhesion characterization method. Two fibers are separated by a wire where the beam is shown by the black profile, the wire is shown by the brown circle, the liquid meniscus is shown by the blue curved line, and angles α_1 , α_2 , ϕ , and θ are dependent upon the slope of the profile at the point of contact with the wire, point A. Additionally, L_{crack} is the length of the crack from $x=0$ to A' , l_{wet} is the length of the wet region from $x=0$ to the meniscus location, and l_{dry} is the length of the dry region or air-gap between the meniscus and A' . V_{adx} and V_{ady} are the tangential, x, and normal, y, components of adhesion force, respectively. F_n is the normal force created at the post. The $Y(X)$ is the beam profile and dy/dx is the slope of the beam at the point A.	15
5	a) Idealized profiles of two fibers (black) separated by a wire (brown) at one end but together at the other. Three different loading scenarios on the beam ends: b) $\theta = \pi/2$, purely normal force F_{nx} acting on the beam, c) $\theta < \pi/2$, compression of the beam created by inward horizontal component of the normal force, F_{nx} , and d) $\theta > \pi/2$, tension of the beam due to the outward acting horizontal components of the force, F_{nx}	16

List of Figures (Continued)

Figure	Page
6	<p>a) Schematic for butterfly galeae separation experiment where the butterfly is shown in black and orange in the top right, its proboscis is shown in black, is extending to the left, and is separated by a wire shown as a red circle between the black profiles. Positions $x=0$, $x=l_{wet}$, and $x=L_{crack}$ are the crack location, meniscus location relative to the crack location, and the position of contact between the galea and the wire, respectively. The wet region is displayed by zone 1 which has liquid and is shown with details in the insert below the schematic of the butterfly. The dry region is shown by zone 2 which has no liquid and thus, only has the distributed moment. b) Zoom in of zone 1 where the orange arrows represent the capillary force that varies linearly with respect to the deflection of the proboscis away from the neutral axis (shown by the equation for $p(x)$) and the green curled arrows represent the distributed moment m in the beam which accounts for muscular action. c) Free-body-diagram of the cut region from b) (shown by the dashed blue lines), where M and V signify the internal moment and shear force, respectively.</p>
7	<p>Sensitivity of the model against fitting parameter B. a) Deflection profiles with $\theta = \pi/2$, $L=30$, $\gamma=.62$, and varying B from .05 to .13. b) Second derivative of the deflection profile (curvature) with the same parameters as mentioned in a). c) Deflection profiles with the same parameters as in a), but varying B from .0001 to .1 to investigate the effects of B at very low values. d) Deflection profiles with same parameters as in a), but varying B from .1 to .4 to show that waves start to propagate in our solution above a certain threshold of B. For different inputted parameters, we will have different usable ranges of B.</p>
	19
	29

List of Figures (Continued)

Figure	Page
8	Sensitivity of fittings to other parameters where $L=30$, $B=.13$, and other parameters are varied. a) Varying length of the wet region from $l=0$ to $l=20$ for $\gamma=.62$ and $\theta = \pi/2$. b) Varying the angle θ from $\theta =23\pi/48$ to $\theta =25\pi/48$ for $l=20$ and $\gamma=.62$. c) While keeping other parameters stable and $l=15$, varying the dimensionless parameter γ from $\gamma=.52$ to $\gamma=.77$ by changing the values of the post radius in the parameter. For $\gamma=.52$, $.62$, and $.77$, post radii of $R=50\text{ }\mu\text{m}$, $62.5\text{ }\mu\text{m}$, and $75\text{ }\mu\text{m}$ were used, respectively.31
9	Displaying the effect of γ on the profile. Varying γ from $.001$ up to 1.5 . Parameters used were $\theta = \pi/2$, $L=30$, $B=.13$, and l is being varied from a) $l=0$, b) $l=10$, c) $l=20$, and d) $l=30$32
10	Displaying the effect of γ on the profile. In this case we are varying γ from $.001$ up to 1.5 . Parameters used were $\theta = \pi/2$, $L=60$, $B=.13$, and l is being varied from a) $l=0$, b) $l=20$, c) $l=40$, d) $l=60$33

List of Figures (Continued)

Figure	Page
11	Experimental setup for proboscis separation and butterfly sedation. a) Side view of the setup where the butterfly is shown with its wings in paper (shown by the transparent rectangle) and held together with a clothespin (brown). The proboscis (black line extending off of the head of the butterfly) was extended and placed in a PDMS clamp (not pictured) to ensure stability of the galeae. The butterfly was sedated by using dry ice in a warm water bath (beaker on a hot-plate shown to right of the butterfly) to create a CO ₂ gas which flowed out of the tube (green) via a showerhead configuration to surround the butterfly with the gas. After sedation the butterfly recovers completely within a few minutes. b) Top view of the galea separation experiment where the blue regions between the galeae represent the saliva menisci and the red signifies the separation post. c) Experimental frames of the separated galeae showing saliva propagation of a butterfly in the “active” state, or before it has been dosed with CO ₂ .
	39
12	Flow-chart displaying data flow between LabVIEW (green) and Mathematica (red) to outline the general steps used in video/data analysis. The steps for LabVIEW analysis can be found in this chapter, but those used for data analysis in Mathematica can be found in Chapter 3.2.3.
	44
13	a) Original, sample image of the butterfly proboscis which had been split by a tungsten wire and b) the binary (black and white) image with contours (thick green lines) on the exterior of the proboscis and the regions of interest shown by the thin green rectangles situated at an angle parallel to the length of the proboscis.
	45

List of Figures (Continued)

Figure	Page
14	Displaying the escape of saliva from the tip of the proboscis and its propagation inside of the PDMS clamp over time. The video was recorded at 30 FPS.....
	52
15	Displaying the increasing of the meniscus retraction length (L_R) (normalized by the diameter of the post) over time (t) and where the L_R is measured by the change in distance between the meniscus front and the center of the post for butterflies in the sedation process. The data (hollow circle points) were fit with square-root-of-time kinetics as can be seen by the solid colored lines. In this graph, each color is representative of a single butterfly in a single video and the data points were taken at each frame in the videos where saliva retraction was seen.
	53
16	Butterflies undergoing sedation process: a) M213 141820 Sedating BG Frame 123, b) M213 141820 Sedating TG Frame 142. Video 2: c) M213 141820 Sedating BG Frame 124. Active butterflies: d) M12 120131 Awake BG Frame 0, e) M12 120131 Awake TG Frame 14, and f) M18 170354 Awake BG Frame 301.....
	55
17	Displaying the average B values for Monarchs (shown in orange and M on the legend) and Painted Ladies (shown in purple and PL on the legend) in the active state (A on legend), sedating state (Se), and sleeping (anesthetized) state (Sl). It can be seen by the error bars overlaying the data bars that for the case of active butterflies, there is much more variability than there is for sedated butterflies. Also, it is worth noting that TG and BG signify Top Galea and Bottom Galea, respectively.
	56

List of Figures (Continued)

Figure		Page
18	Modulus of Elasticity values taken from DMA tensile testing. This bar graph follows previous conventions; orange represents monarchs tested, purple represents the painted ladies tested, and the green represents the average modulus of all butterflies tested with an error bar showing one standard deviation above and below the average. The legend can be read as such; M stands for Monarch and PL stands for Painted Lady, the number afterwards represents the number of butterflies tested, and A or B signifies the galea that was tested from that butterfly.	61
19	Displaying the Capillary force (F_c) against the length of the wet region along the length of the galeae. As capillary length increases, we have a corresponding increase in magnitude of capillary force and, thus, a greater restoring force. In this figure, the orange and purple dots represent data from Monarchs and Painted Ladies, respectively. Additionally, the error bars in the x and y directions are showing one standard deviation for each of the data points. The larger error bars correspond to tests on active butterflies while those with smaller error bars are typically sedated or sleeping butterflies. The linear trendlines were added to guide the eye as to how the data was acting. This raw data can be found in supplemental information.	65
20	Adhesion forces plotted against θ in the a) Horizontal direction (V_{adx}) and b) Vertical direction (V_{ady}). In these figures, orange and purple dots correspond to tests with Monarchs and Painted Ladies, respectively. Error bars use the same conventions as in previous figures.	66

List of Figures (Continued)

Figure		Page
21	Experimental setup for the reference experiment. a) Side view of the experiment showing the wooden clothespins, the syringe holder, syringe, and 90° angled needle used to send water between the ribbons, the 500 μm separation tungsten wire (shown by the vertical wire in the middle), the tungsten ribbons (shown by the horizontal metallic strip), and the tape holding them together at the ends. b) Top view of the experiment showing the top edge of the ribbons which have been separated by the wire (500 μm).....	73
22	Typical contact angle measurement on the tungsten ribbon. This particular image was taken of a ribbon surface treated with trimethylethoxysilane and had a contact angle of 49.5°	77

CHAPTER ONE

INTRODUCTION

1.1 Principles of Adhesion

Adhesion can be defined as the tendency for two objects to be attracted to one another when brought into close contact with each other (1, 2). This is true on the nano-scale where atoms and molecules form quite strong bonds, but there is a paradox in that statement because it is not always true on the macro, or engineering, scale. For instance, if one placed two ceramic blocks together they would not simply stick together; one would have to place an ‘adhesive’ such as glue, epoxy, or cement in between them to enhance the interfacial attraction. Conversely, the molecules and atoms making up these ceramic blocks adhere very well to each other, otherwise they would not form the large components that they are comprising (1). Thus, the concept of adhesion is not well understood as of yet.

The task of theoretically describing the work of adhesion between two objects, a property which is ideally a characteristic of the joint and independent geometric parameters of specimens, has been a significant challenge and thus, it is instructive to turn to the simplest scenario of adhesion characterization, the peel test (Figure 1). Initially, scientists attempted to analyze the peel test by considering the stress distribution around the peel front but were met with little success due to the complex stress distributions around the peel front (3-5). Others have attempted to use a fracture-mechanics method that considers a stress intensity factor based upon a stress-singularity argument; however, this did not prove successful either (3, 6, 7). Therefore, most people have adopted a simpler approach

that is not based on the complex stress distribution around the peel front or the determination of the stress-intensity factor, and we will do the same (discussed in Chapter 1.2.1).

1.1.1 Benefits of Higher Adhesion at Fiber-Matrix Interface

In the past few decades, the use of fibers as reinforcements in matrices, including polymers and ceramics, to create multifunctional materials has greatly increased due to the capacity for such fibers to enhance the structural (strength, energy absorption, damping, and fracture toughness among others) as well as non-structural properties of a material (thermal conductivity, electromagnetic shielding, and energy storage for example) (8). Since these fibers are now used for such a wide range of applications in multifunctional materials, it is imperative to understand the role that the fiber-matrix interface plays on such properties.

The interface between fibers and their surrounding matrix is a critical region that determines many of the desired mechanical properties of a composite material, for it is responsible for the load transfer from the matrix to the fibers and, hence, the quality of the reinforcement itself (9, 10). At this interface, an interaction between two dissimilar materials, depending on the chemical structure of both phases as well as their chemical affinities for one another, will greatly affect measured adhesion energies. By surface treating the reinforcing fibers, one can adjust the level of interactions at the interface to increase or decrease the adhesion energy accordingly. Hoecker demonstrated this in 1995 by using various surface treatments on carbon-fibers in carbon-fiber-reinforced epoxy

resins and performing transverse and shear tests on the samples; with an improvement in adhesion came an increase in mechanical properties (11). Likewise, the failure mode changed from interfacial failure between the fibers and matrix to one of matrix failure when adhesion was increased. Another study from 2011 performed by Lopez-Buendia added to this correlation, with polypropylene (PP) fibers embedded in concrete (12). In addition to an increase in mechanical properties, an enhanced fiber-matrix interface also leads to increased energy dissipation, damping, and impact absorption as found by multiple researchers in the past couple of decades (13-21). As discussed above, the strength of the fiber-matrix interface in composites is an important aspect of the reinforcement and, thus, a reliable and reproducible means for testing this interface, especially when performed in different laboratories, is required to advance the state of the art.

The interface between a fiber and its surrounding matrix is critical in the transfer of stress of the composite material (22); hence, it is important to have a reliable, repeatable, and versatile characterization method that can be easily adapted to many different types of samples.

1.1.2 Recent Advances in the Field of Adhesion

Of late, researchers have made many developments on the adjustment or enhancement of the common adhesion tests such as the peel test and pull-out test among others. For instance, Hassoune-Rhabbour has adjusted the pull-out technique by changing the shape of the matrix so that it necks towards the fiber at the point of embedment on one end and is perpendicular to the insertion of the fiber on the other end; this was intended to

lead to controlled, localized crack development at the flat end where the stress concentration is higher (23). Moreover, Ostrowicki and Sitaraman created an interesting variant of the peel test called the Magnetically Actuated Peel Test (MAPT) in which they applied a permanent magnet to a specimen, placed it above an electromagnet a known distance, and then ran a current through the electromagnet to create a controlled repulsive force that imposes a peeling of the films from the substrate at a critical load; afterwards, the delamination lengths of the films were measured and correlated with adhesion (24). Additionally, there have been efforts to use vibrations and the inherent vibration damping as a means for measuring the fiber-matrix adhesion of fiber reinforced composites (19, 25, 26). A method proposed by Narkis in 1988 relied on bending jigs to create curvature changes in the fiber for adhesion characterization purposes; this was done to create a desirable method that doesn't depend on the longitudinal fiber strength or embedment length to successfully perform experiments unlike other commonly used testing methods, but it required further theoretical and experimental optimization before it could actually be put to use (27). Only a brief review of the recent advances in the field of adhesion has been mentioned above but, most of these are slight adjustments to existing methods and, thus, are not groundbreaking new characterization methods viable for many applications.

1.2 The Peel Test

The most common testing method used for the measurement of adhesion between thin films and a rigid substrate is the peel test; it has been used for adhesion characterization applications ranging from solar cells (28) to polymer dielectrics (29) and is applicable for

quality control of many multilayered thin film systems that are prone to delamination (24, 28). The peel test is carried out by placing a flexible, thin film onto a substrate and pulling the end of the film with a force acting at an adjustable angle from the substrate surface (24, 30). Like the others previously mentioned, this test is quite straightforward and relatively cheap to perform, but when using films with thickness of less than a few tens of microns, the peel test can result in rupture of the film.

This method has been shown to greatly depend on the mechanical properties of the materials used as well as the dimensions of the specimens (29). Additionally, the angle of peel has a large impact on the measured peel strengths and there has not been a consistent means to compare peel test results at different angles until recently when Eitner used the theory of adhesive fracture originally developed by Kinloch (31) to convert the force values into adhesive fracture energies. Before this, however, it was easy for manufacturers to report higher adhesion values than one would typically find by peeling the film at low angles; in this way they would obtain high adhesion values despite the bond being of the same strength (28). Also, recently a few variations of the peel test have been put into effect, most notably those working with wires (32) and large plastic deformations of the adherends or substrates (33).

1.2.1 Energy Model of the Peel Test

This approach considers an energy balance which leads to a term for adhesive fracture energy, G_a , the energy needed to propagate a crack through a unit area of the joint. The problem of the peel test is defined as follows: a peel force, P , is applied to the end of

the film, or peel arm, at a certain angle, θ , which then propagates the crack front a certain distance da and debonds the film from the substrate. For this example, we will be following similar methods to those laid out by Kinloch previously (31). The movement of the applied force can be defined by the distance $da(1 - \cos \theta)$ and, thus, the work done by the applied force is $dU_{ext} = Pda(1 - \cos \theta)$.

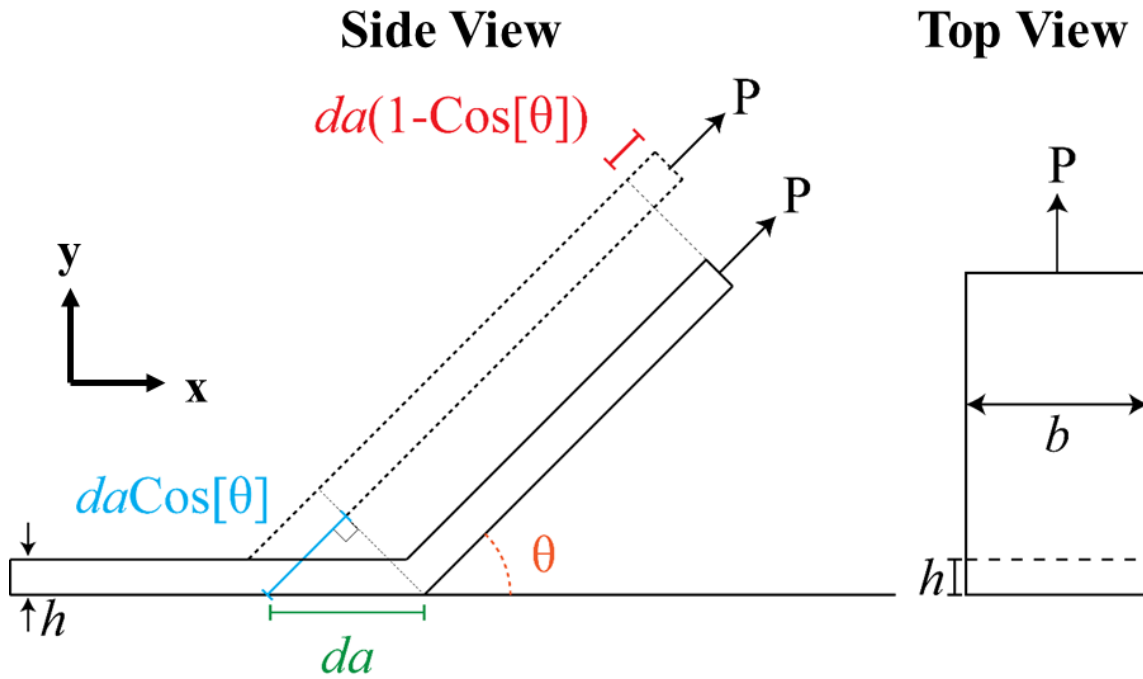


Figure 1. Energy model of the peel test where P is the pulling force at angle θ from the substrate. da is the length that the film debonded from the surface, b is the width of the film, and h is the thickness of the film.

Now, to establish an energy-based analysis of this system, we must first lay out the assumptions. First, we will consider the case where the film is perfectly flexible in bending and inextensible in tension. Also, we will be considering a steady-state process in which the debonding region remains the same while the crack is propagating at a constant rate V . These assumptions are not always present, but comprise a natural starting point for this

particular fracture mechanics problem. Now the energy analysis of this problem can be initiated and written in terms of the energy release rate, G , where the adhesive fracture energy density, G_a , can be found through [1]:

$$\begin{aligned} G_a dA &= G_a b da = dU_{ext} \\ dA &= b da \end{aligned} \quad [1]$$

Where dA is the increment of area created (b is the width of the film). Henceforth, for the simple case that is infinitely rigid in axial tension (given a superscript of ∞E), we have an adhesive energy of fracture per unit area shown by equation [2] below.

$$G_a^{\infty E} = \frac{P da (1 - \cos \theta)}{b da} = \frac{P}{b} (1 - \cos \theta) \quad [2]$$

This methodology can be extended to more complex cases such as one in which tensile deformation of the peeling arm occurs due to the tensile stress (3); however, we will not be using these results in these works and thus will not be going into further detail.

1.2.2 Force Model of the Peel Test

Now instead of an energy approach that was taken in the previous section, we will be considering a quasi-static force balance for the peel test. When using a modified setup as found by Figure 2, we can see that for the peel test a peeling force, P , is applied to one end of the film while the other end is adhered to a substrate and the resisting forces, F_{adx} and F_{ady} , act in the x and y directions, respectively.

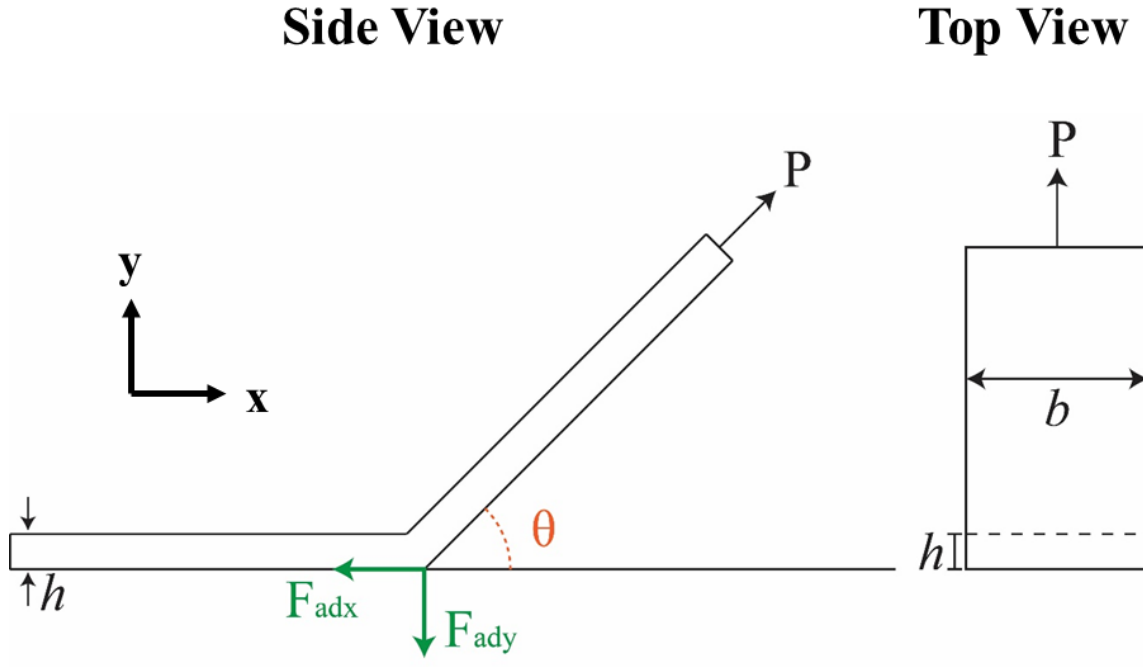


Figure 2. Force model of the peel test where P is the pulling force at angle θ from the substrate and F_{adx} and F_{ady} are the resisting forces in the x and y directions respectively. Additionally, b and h are the width and thickness of the film, respectively.

When pulling on this film, one has to overcome a certain force threshold before the film detaches from the surface of the substrate in any direction, but this force is not acting completely in one direction; it has components in both the normal and tangential directions due to the angle θ . Therefore, we can say that there is an adhesion force acting at the crack location that holds the film to the substrate and resists the peeling force P in both the y , normal, and x , tangential, directions relative to the substrate when assuming the substrate surface extends in the x -direction. First, we will look at the force balance in the x -direction:

$$\begin{aligned}
 &\rightarrow \sum F_x = 0: \\
 &P \cos(\theta) - F_{adx} = 0 \\
 &F_{adx} = P \cos(\theta)
 \end{aligned}
 \tag{3}$$

Where $P\cos(\theta)$ is the x-component of the peeling force P and F_{adx} is the force due to adhesion acting in the x, or tangential, direction. Likewise, we can introduce the force balance in the y-direction, where F_{ady} is the force due to adhesion acting in the y-direction and $P\sin(\theta)$ is the y-component of the peeling force:

$$\begin{aligned}\uparrow \sum F_y &= 0: \\ P\sin(\theta) - F_{ady} &= 0 \\ F_{ady} &= P\sin(\theta)\end{aligned}\tag{4}$$

For the static case before the crack starts to propagate through the system, we can establish the x and y components of the adhesion force by simply considering the force balance.

This simple method is advantageous over the energy approach due to the fact that energy only considers the vertical bond between the film and the substrate while this method also considers the horizontal; however, to extend it to dynamic systems where movement of the crack is present, one would have to add the acceleration term in Newtonian mechanics in place of the zero on the right hand side of the force balance and this would be another unknown that would have to be measured experimentally.

1.3 Introduction to Lepidoptera: The Butterfly Proboscis

The mouthparts of lepidopterans, the order of insects composed of moths and butterflies (34), are complex feeding apparatuses that make use of unique material properties to keep the organs clean while the organism is drinking sticky and viscous liquids. Specifically, the dichotomy of the wetting properties (35) along the length of the lepidopteran proboscis, an interesting bio-fiber composed of two separate, semi-elliptical

organs known as galeae (Figure 3), is thought to assist in this process. The external surface of the proboscis has a drinking region near the tip with hydrophilic properties and a non-drinking region for the rest of the length (35). These wetting properties, combined with its elliptical shape (Figure 3.b), help to create a larger meniscus in the hydrophilic region which facilitates the entrance of the liquid into the food canal along with the feeding from various types of sustenance ranging from floral nectar and sap to blood and dung (36). All of the while, the butterfly proboscis remains clean from debris that could impede fluid uptake due to the hydrophobic nature of the majority of the external surface (37-39). However, the feeding functionality of the proboscis is not the only interesting mechanism in the proboscis; the coiling and uncoiling capabilities for storage, usage, and assembly (38, 40, 41), is a biomechanical feature that helps to create an intricate organ with many possible bio-medical and mimetic applications in drug delivery and micro-fluidics (37, 42). Before engineers will be able to replicate the fascinating capabilities of the butterfly proboscis, however, the materials properties and assembly mechanism must be investigated, quantified, and understood and thus, that is one particular goal of this work.

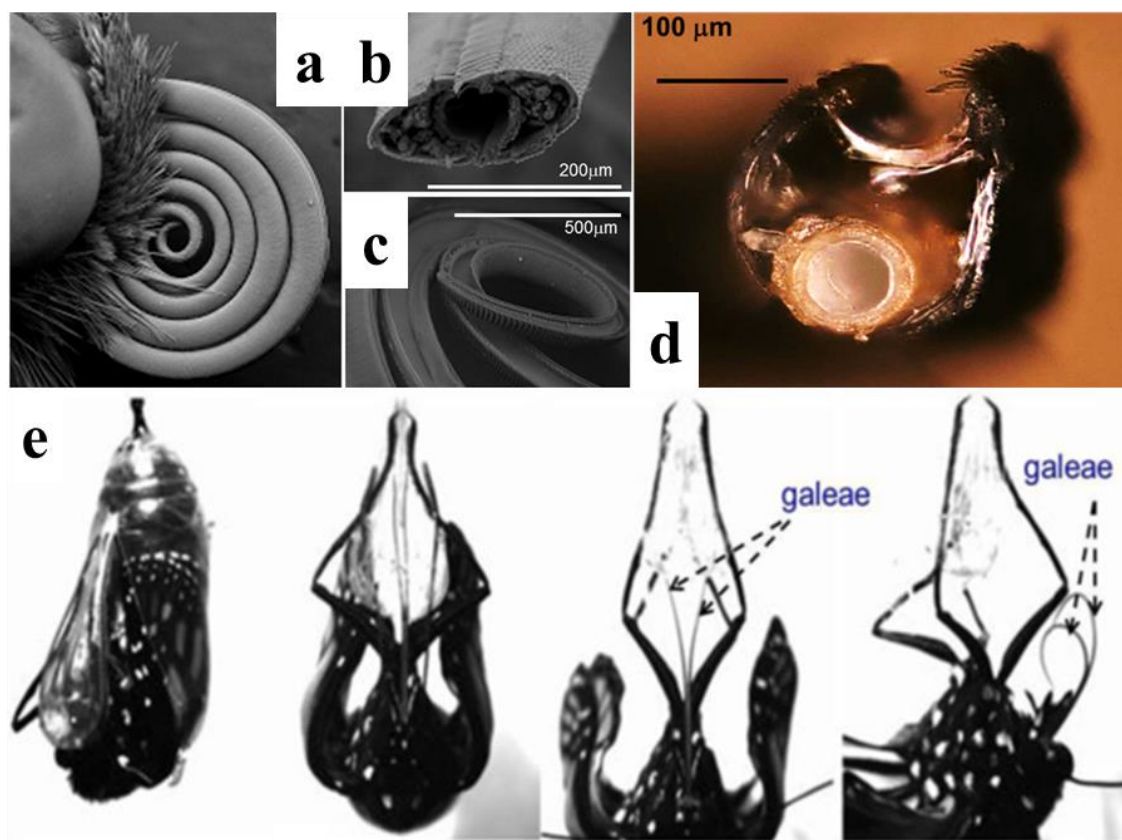


Figure 3. a) Scanning Electron Microscope (SEM) image of the butterfly proboscis in the coiled state, b) the cross section, and c) the single galea curled up. These images were taken from (43). d) A cross section of a single galea where the white circular tube is the trachea, and the semi-circular cut-out at the top is one half of the food canal. e) Displays the emergence from the pupa, or 'eclosion', and that the two galeae are separated at this moment and come together with a series of coiling-uncoiling motions along with saliva pumping (courtesy of D. Monaenkova).

In the past, the lepidopteran proboscis was thought to assemble only once during the insect's lifetime (40). This initial linking is facilitated via a series of coiling and uncoiling motions immediately after eclosion (shown in Figure 3.e) during which the cuticular structures known as the dorsal (top) and ventral (bottom) legulae interlock (38, 40); however, throughout this process, saliva is omnipresent which leads one to come to a realization that saliva may actually play a significant role in the assembly of the split/damaged proboscis. Recently, it was discovered that if the butterfly mouthparts are separated, the butterfly can actually bring the galeae back together and repair the proboscis

back into one fiber (44). We hypothesize that by using a combination of muscular action in the galeae, internal pressure from the hemolymph canals running through the galeae, and capillary forces from liquid saliva which is being pumped from the head into the split proboscis region, the butterfly can successfully bring the split galea back together into one component. Our goal is to determine the role that saliva plays in the repair of the proboscis and estimate the longitudinal Young's Modulus of Elasticity (E) of the single galea as well as the adhesion force between the galeae for use in bio-mimetic and micro-fluidic transportation devices (37, 42) further down the road.

CHAPTER TWO

RESEARCH OBJECTIVE

2.1 Motivation of Study

The proboscis has been well described by biologists in regard to its shape and behavior across many species of Lepidoptera (34, 45). However, the proboscis has never been studied from the materials science point of view and thus, there are many unknowns that lead to questions such as: What are the role of capillary forces in proboscis assembly or repair? What is the Modulus of Elasticity (E) of the proboscis? What are the adhesion forces holding the galeae together in this repair process? Therefore, the goals of this study are to find solutions to these problems by using the separated galeae profiles along with Euler-Bernoulli beam theory. Additionally, due to the lack of repeatable adhesion characterization techniques currently available, it is our goal to create an adhesion characterization method founded on the deflection of fibers and useable with fiber-fiber interactions or fiber-matrix adhesion cases.

2.2 Bio-Inspired Adhesion Characterization Method

After its emergence from the pupa or in the case of separation later in life, the butterfly tries to unite the two galeae with a series of coiling-uncoiling motions along with saliva pumping as shown by Figure 3.e. In this series of events, a saliva meniscus can be seen propagating between the two fibers and it is hypothesized that this saliva column helps to bring the galeae together with capillary and adhesion forces. This idea is supported by recent findings that show that capillary forces are strong enough to bend and greatly deform

slender structures, such as fibers and wires (46-49). The butterfly proboscis is modeled by this scenario due to its high aspect ratio (long and thin) and the saliva propagation in the assembly/repair process. Henceforth, we have studied the self-repair mechanism by separating the galeae, straightening the fibers, keeping them separated with a wire far away from its head, and then observing any repair that occurred. The similarities in geometry between this galeae separation experiment and the peel test sparked the idea to create a new experiment founded on the concepts of fiber separation and adhesion.

Therefore, we have created a novel adhesion characterization method inspired by this repair of the split Lepidopteran proboscis (Figure 4) and related to the force balance that was displayed for the peel test in Figure 2. The experiment is comprised of two fibers that are separated far away from their point of contact with each other by a wire of known diameter, as depicted by the schematic in Figure 4. Hence, the fiber deflection relative to the x-axis (black horizontal line in Figure 4) is known at the point of incidence A' . In the previous peel test case, the force P and angle at which the film was being pulled, θ , were known parameters; however, in our case, the normal force created by the contact between the post and the fiber is not known and must be quantified to determine the unknown adhesion forces at the point of fiber contact, $x=0$. To classify these forces, we have implemented the Euler-Bernoulli beam theory (50) which is a simplification of the Euler-Elastica theory (51) for the case of small deflections of the beam relative to its length. This beam theory uses the profile and deflection of the fibers to calculate the shear forces in the fibers or 'beams' and thus, allows us to calculate the normal force created at the post position along with the interfacial adhesion forces between the two fibers in both the

normal and tangential directions. Further details as to how this problem was solved can be found in Chapter 3.1.2.

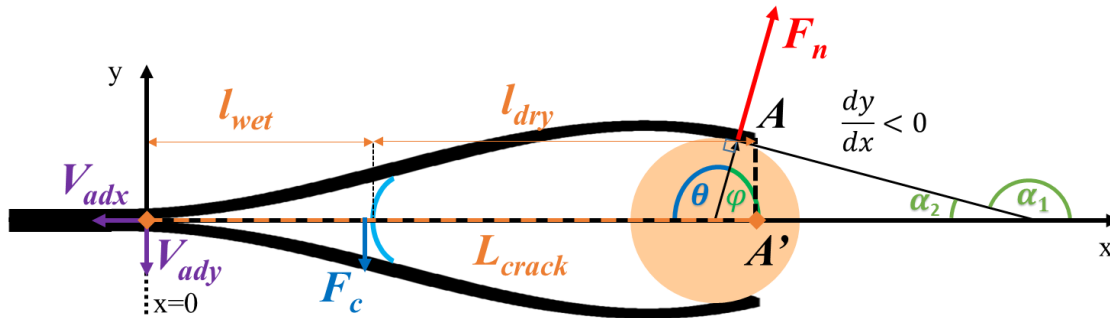


Figure 4. Experimental Schematic for the adhesion characterization method. Two fibers are separated by a wire where the beam is shown by the black profile, the wire is shown by the brown circle, the liquid meniscus is shown by the blue curved line, and angles α_1 , α_2 , φ , and θ are dependent upon the slope of the profile at the point of contact with the wire, point A. Additionally, L_{crack} is the length of the crack from $x=0$ to A' , l_{wet} is the length of the wet region from $x=0$ to the meniscus location, and l_{dry} is the length of the dry region or air-gap between the meniscus and A' . V_{adx} and V_{ady} are the tangential, x , and normal, y , components of adhesion force, respectively. F_n is the normal force created at the post. The $Y(X)$ is the beam profile and dy/dx is the slope of the beam at the point A.

For this problem, we have three different cases of profile shape that could occur due to the stiffness of the beams and the wire position and as such, we could have three different loading scenarios: purely vertical forces, axial compression, and axial tension. These scenarios are demonstrated by Figure 5 where V_{adx} , V_{ady} , F_{nx} , F_{ny} , and F_c are the x and y components of adhesion force, the x and y components of the normal force F_n at the position A' (Figure 5), and the capillary force, respectively. Additionally, θ is the angle between the x-axis and the vector A (Figures 4 and 5).

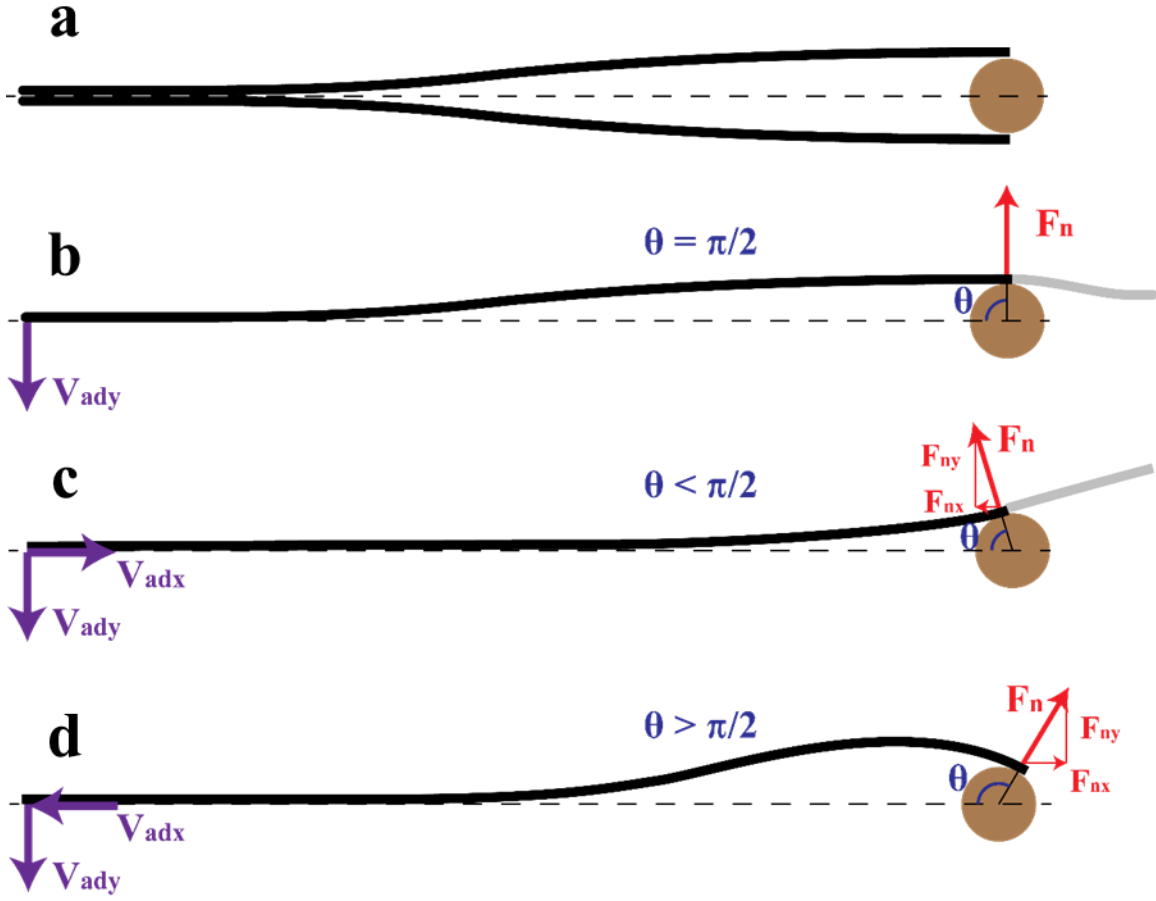


Figure 5. a) Idealized profiles of two fibers (black) separated by a wire (brown) at one end but together at the other. Three different loading scenarios on the beam ends: b) $\theta = \pi/2$, purely normal force F_{nx} acting on the beam, c) $\theta < \pi/2$, compression of the beam created by inward horizontal component of the normal force, F_{nx} , and d) $\theta > \pi/2$, tension of the beam due to the outward acting horizontal components of the force, F_{nx} .

CHAPTER THREE

RESEARCH METHODOLOGY

3.1 Splitting of the Butterfly Proboscis

3.1.1 Motivation

Determining the mechanical properties of the butterfly galeae is a difficult task due to the complex geometry and small size of the fibers, its need to revert back to its natural, coiled state once straightened, and the hydrophobicity of its exterior surface. Additionally, once separated from the rest of the butterfly for tensile testing, one has to be careful not to create any disturbances in the galeae that would cause a stress concentration and create premature breakage of the fiber. Therefore, it is necessary to develop non-conventional methods for the characterization of the galeae and as such, we have devised another method of testing that does not rely on separating the galeae from the head and actually uses live butterflies instead. This method is based on a modification of the Euler-Bernoulli beam theory approach for considering the profile of beams, or galeae in our case, undergoing small deflections. By using this method, we can also evaluate the shear forces along the beam caused by the adhesion forces at the galea-galea interface as well as the normal force caused by the wire.

3.1.2 Theoretical Model Describing Galeae Deflection and Adhesion

In the following sections, we describe the experimental protocol of splitting the butterfly proboscis along with the procurement of videos. To gather information from these videos we must analyze them for galea profile changes over time by extracting the

contour lines of the dark border separating the outer walls of the galeae from background in the images. This video analysis algorithm will be further described in Chapter 3.2; however, at this time it is important to introduce the mathematical model underlying the contour fitting of the deflected galeae for the extraction of materials properties.

To characterize the materials properties of the butterfly proboscis, we have chosen to use an augmented version of the well-understood Euler-Bernoulli beam theory, which is used primarily to determine the load-bearing and deflection characteristics of beams when subjected to lateral loads and small deflections (50). The reasoning behind the use of this theory will become evident after establishing the force and moment balances acting on a galea during the repair process. The galea profile is described by function $y=y(x)$, Figure 6.

When splitting the proboscis of the butterfly and keeping them separated at a distance far from the head, a liquid column of saliva can be seen propagating through the food canal during which muscular contractions and expansions inside of the galeae work to bring the galeae back together and eventually lock the legulae in place. The forces from the muscular movements are being approximated by a distributed moment m of uniform amplitude acting along the entire length of each galeae and the capillary force is being modeled by [5] where F_1 and F_2 are constants. However, the capillary force is only acting up to the saliva meniscus, and thus, we have two distinct zones to consider.

$$p(x) = F_1 - F_2 y(x) \quad [5]$$

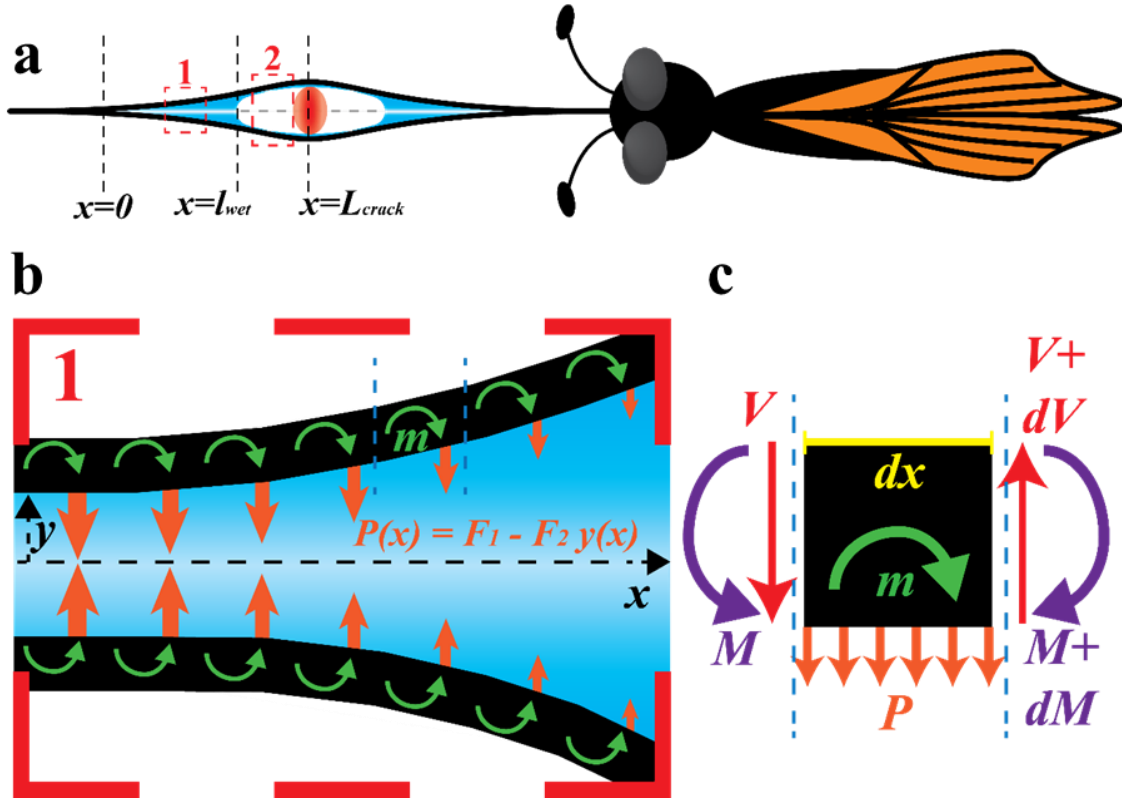


Figure 6. a) Schematic for butterfly galeae separation experiment where the butterfly is shown in black and orange in the top right, its proboscis is shown in black, is extending to the left, and is separated by a wire shown as a red circle between the black profiles. Positions $x=0$, $x=l_{wet}$, and $x=L_{crack}$ are the crack location, meniscus location relative to the crack location, and the position of contact between the galea and the wire, respectively. The wet region is displayed by zone 1 which has liquid and is shown with details in the insert below the schematic of the butterfly. The dry region is shown by zone 2 which has no liquid and thus, only has the distributed moment. b) Zoom in of zone 1 where the orange arrows represent the capillary force that varies linearly with respect to the deflection of the proboscis away from the neutral axis (shown by the equation for $p(x)$) and the green curled arrows represent the distributed moment m in the beam which accounts for muscular action. c) Free-body-diagram of the cut region from b) (shown by the dashed blue lines), where M and V signify the internal moment and shear force, respectively.

3.1.2.1 Zone 1: Meniscus Region

For this zone, we have to incorporate all of the forces due to capillary action since the liquid column is present here; thus, we will be taking into account the surface tension as well as the capillary pressure inside of the liquid column approximated by [5]. Hence, after making two cuts in the galea to expose internal forces (Figure 6) on each side of a segment dx in length, the vertical force balance is as follows:

$$\uparrow \Sigma F_{y^+} = 0 \Rightarrow -V - p(x)dx + (V + dV) = 0. \quad [6]$$

After simplifying [6], we are left with an expression for the change in internal shear force, denoted by V :

$$\frac{dV}{dx} = p(x). \quad [7]$$

Similarly, we can sum moments on the galea to get an equilibrium expression with the leftmost side of the cut portion with two exposed sides shown in Figure 6 with counter-clockwise as our positive sign convention. This summation is shown in

$$\rightarrow \uparrow \Sigma M = 0 \Rightarrow M - mdx - (M + dM) + (V + dV)dx - \frac{p(x)dx^2}{2} = 0. \quad [8]$$

Simplifying [8] and neglecting higher order terms yields an expression for the change in internal moment denoted by M :

$$\frac{dM}{dx} = -m + V. \quad [9]$$

Since we know that the internal shear force V changes along the x-direction, we can take the first derivative of [9] which leads:

$$\frac{d^2M}{dx^2} = -\frac{dm}{dx} + p(x) \quad [10]$$

Remembering the expression for the well-known Euler-Bernoulli relation:

$$M \cong -EIy''(x), \quad [11]$$

where E is the longitudinal Young's elastic modulus (a material property) and I is the area moment of inertia (structural property) which is dependent on the cross sectional shape

(52). Taking the second derivative of [11] with respect to x gives an expression into which we can input [5] and [10]. Thus, we arrive at our fourth order differential equation

$$\begin{aligned} EIy_1''''(x) &= -p(x) + \frac{dm}{dx} \Rightarrow \\ EIy_1''''(x) &= -F_1 + F_2 y(x) \end{aligned} \quad [12]$$

In [12], we can neglect dm/dx by assuming that the butterfly is sedated; in this case, m is a constant amplitude along the length of the galea and, thus, the 1st derivative of m with respect to x would go to zero.

3.1.2.2 Zone 2: Air Gap

Similarly, we can set up the model for zone 2 where the liquid column has not reached yet; thus, there are no capillary forces present, i.e. $p(x)=0$ and we only have to consider the distributed moment m along the galea. As discussed directly above, this distributed moment is of constant amplitude and therefore, the first derivative goes to zero in this zone as well. Hence, we are left with the characteristic equation for zone 2:

$$EIy_2''''(x) = 0. \quad [13]$$

3.1.2.3 Normalizing Differential Equations

Since both of these characteristic equations, [12] and [13], are fourth order differential equations, we will need a series of boundary and continuity conditions, specifically 8, to solve them together and create a fitting model from them. Before establishing the boundary conditions, however, it is convenient to normalize equations [12] and [13] by the radius of the post R ; thus, we have $y = YR$ and $x = XR$ where Y and X

are dimensionless parameters for deflection and horizontal position along the length of the proboscis respectively. The normalized equations can now be rewritten as:

$$\text{Zone 1:} \quad Y_1'''(X) = -\frac{F_1 R^3}{EI} + \frac{F_2 R^4}{EI} Y_1(X) \quad [14]$$

$$\text{Zone 2:} \quad Y_2'''(X) = 0. \quad [15]$$

Also, the ratios $F_2 R^4 / EI$ and $F_1 R^3 / EI$ are both dimensionless parameters. Note that the dm/dx has been dropped prior to normalization due to reasons discussed previously.

3.1.2.4 Boundary Conditions

The angle θ , an important parameter which helps to define the shape of our beams near the post, has been introduced in Figures 4 and 5. The boundary conditions are specified as

$$\begin{array}{ll} Y_1(0) = 0 & Y_1'(0) = 0 \\ Y_2(L) = \sin \theta & Y_2'(L) = \cot \theta \\ [Y(l)] = 0 & [Y'(l)] = 0 \\ [Y''(l)] = 0 & [Y'''(l)] = 0 \end{array} \quad [16]$$

where $L = L_{crack} / R$ and $l = l_{wet} / R$. In this equation set, $Y_2(L)$ & $Y_2'(L)$ define the deflection and slope of the beam at point A (Figure 4) and $[Y''(l)] = Y_1''(l) - Y_2''(l) = 0$ is a continuity condition that signifies that the second derivative of the deflection equations in zones 1 and 2 must be equal at position l . Additionally, the zeroth, first, second, and third derivatives of $Y(X)$ correspond to the deflection, slope, moment, and shear force distributions in the beam, respectively. The same conventions apply to the rest of the

conditions in equation set [16] where L is the normalized length from the crack position (at $X=0$) to point A and l is the length from $X=0$ to the meniscus position where zones 1 and 2 meet. The two locations L and l are unknown and perpetually moving during the videos due to the saliva pumping by the butterfly; thus, we have to introduce two more equations specifying the galea deflection at the meniscus:

$$\begin{aligned} Y_1(l) &= y_{cr} \\ Y_2(l) &= y_{cr} \end{aligned} \quad [17]$$

where $y_{cr} = y(l_{wet})/R$. The critical separation distance, y_{cr} , is found by measuring the displacement of the galea from the horizontal axis at the meniscus front. The conditions in the first row of equation set [16] state that the deflection and slope of the galea at point $X=0$ must be met for the galeae to have symmetry about the X -axis, which is required in our model. This X -axis extends from some point where the galeae are together to the center of the separation post. At this point, we have a system of 10 equations and 10 unknowns and henceforth, our system of equations is well established.

3.1.2.5 Solution

First, we will start with equation [14]. By using standard methods of solving the 4th order differential equations (50, 53), we can determine the general form of the equation for zone 1:

$$Y_1 = \gamma + A_1 \sinh(BX) + A_2 \cosh(BX) + A_3 \sin(BX) + A_4 \cos(BX) \quad [18]$$

where B is a non-dimensional term consisting of

$$B = \sqrt[4]{\frac{F_2 R^4}{EI}} = \sqrt[4]{\frac{F_2 R^4}{D}} \quad , \quad [19]$$

EI has been replaced by the flexural rigidity, D , since it is a measure of the resistance to beam deflection (51), and γ is the particular solution found to be $\gamma = \frac{F_1}{F_2 R}$. By simple integration of [15], we can come to the general solution for zone 2:

$$Y_2 = C_1 X^3 + C_2 X^2 + C_3 X + C_4 \quad [20]$$

where all of the A and C terms in [18] and [20] are integration constants. To solve for these 8 integration constants, along with the two unknown positions, l and L , we must use the system of equations established for the boundary conditions [16] paired with a combination of analytical and numerical methods in Wolfram Mathematica[®]. The solutions for [18] and [20], which are used in the fitting algorithm, are shown by the equations [21] and [22] below:

$$Y_1 = \gamma + \cos(BX) \left(\frac{N_{11}}{D_{11}} - \gamma \right) - \cosh(BX) \frac{N_{11}}{D_{11}} + \sin(BX) \frac{N_{21}}{D_{21}} - \sinh(BX) \frac{N_{21}}{D_{21}} \quad [21]$$

$$Y_2 = (X - L)^2 \frac{(-N_{12} - XN_{22} - N_{32})}{D_{12}} + (X - L) \cot(\theta) + \sin(\theta) \quad [22]$$

where N_{11} , N_{21} , D_{11} , D_{21} , N_{12} , N_{22} , N_{32} , and D_{12} are all constants determined by solving for the integration constants in [18] and [20]. In this case, placeholders N and D represent numerators and denominators in the solution where the subscripts denote the order that it shows up in each solution, respectively. For further clarification, the notation can be described as follows: N_{11} represents the first numerator in our Y_I solution and D_{12} denotes

the first denominator in the Y_2 solution. These expressions are too bulky to display in the main text and, thus, can be found in appendices.

Once these equations were solved with the boundary and continuity conditions, we established a piecewise function stating that from positions 0 to l , the solution [21] for zone 1 was to be used and likewise, from l to L , the solution [22] for zone 2 was used. The sensitivity of the piecewise solution has been discussed in Chapter 3.1.2.6. After inputting all of the experimental constants into the piecewise solution, we were able to fit the profiles of the beams with our theory to extract the materials properties of the fibers. The results are presented in Chapter 4.

3.1.2.6 Adhesion Forces

To gather the desired adhesion forces acting to hold the galeae together, we must establish a free-body-diagram (FBD) as shown by Figure 4 previously. This FBD has been setup by making cuts at both the left and right sides of the galeae which exposes the internal forces present in the beam, specifically those from the shear forces along the beam. Additionally, to establish the shear forces in the beam, we must go back to equation [12] which is the non-dimensionalized general form of the solution for zone 1. We also must remember that when considering a constant distributed moment along the beam, as is assumed in this works, the right hand side of [12] is equal to dV/dx shown by equation [7]. Therefore, we can multiply everything in [7] by dx and integrate along the length of the beam as shown below:

$$EIy''' = -F_1 + F_2y(x) = \frac{dV}{dx}$$

$$\int_0^{L_{crack}} EIy''' dx = \int_0^{L_{crack}} \frac{dV}{dx} dx . \quad [23]$$

But since the forces F_1 and F_2 are only acting in the liquid column, integration for this term is limited to the length l :

$$EI(Y'''(L) - Y'''(0)) = V(L) - V(0)$$

$$= \int_0^{l_{wet}} (-F_1 + F_2y(x)) dx \quad [24]$$

which accounts for the capillary forces due to surface tension and capillary pressure. Now, to use this equation with our model, we have to input $y(x) = YR$ into [24] which leaves us with a our capillary force, F_c :

$$F_c = \int_0^l (-F_1 + F_2Y(X)R) R dX . \quad [25]$$

This leaves us with units of [N] as is expected for this force. Now, we have one of the forces acting on our system. However, we still need to account for the normal force F_{ny} as well as the adhesion forces V_{ady} and V_{adx} , the Y -component of which can be found from the shear force at the crack position:

$$V_{ady} = EIy'''(0) = \frac{EI}{R^2} Y'''(0) . \quad [26]$$

Likewise, we can evaluate the third derivative at position A to determine the Y -component of the normal force acting between the separation post and the galea, F_{ny} :

$$F_{ny} = \frac{EI}{R^2} Y'''(L) . \quad [27]$$

Now, if we consider Figure 4, we can create a vertical force balance from the exposed forces in the FBD which can be used as a check since they need to sum to zero. We have already found F_c , V_{ady} , and F_{ny} and, thus, we can sum forces in the Y-direction as:

$$\begin{aligned}\uparrow \sum F_y &= 0: \\ F_{ny} - V_{ady} - F_c &= 0 \\ EI(Y'''(L) - Y'''(0)) &= F_c\end{aligned}\tag{28}$$

and due to the geometry of the galea on the post, we can assume

$$F_{nx} = F_{ny} \tan\left(\frac{\pi}{2} - \theta\right)\tag{29}$$

where F_{nx} is the X-component of the normal force due to the contact between the wire and the galea. Finally, if we sum forces in the X-direction, we can calculate the X-component of the adhesion force, V_{adx} , which is something that is never accounted for by the energy approach used by pioneers of adhesion and fracture such as Obreimoff (54) and Kinloch (3, 31). This horizontal summation gives:

$$\begin{aligned}\rightarrow \sum F_x &= 0: \\ V_{adx} &= -F_{nx}\end{aligned}\tag{30}$$

and as shown in [30], V_{adx} is an equivalent and opposite force of F_{nx} . Thus, we have firmly established all of the forces in our system and created a means to determine the adhesion forces, something which has not yet been documented. However, to be able to determine the forces found in experiments, we first must have a robust video analysis algorithm that can easily gather all of the experimental parameters and calculate the flexural rigidity D of the galeae. Moreover, we can use this flexural rigidity in combination with the area moment of inertia, I , to calculate the modulus of elasticity, E , of the galeae to get a sense

of the real-world strength of the proboscis. This video analysis procedure is discussed in Chapter 3.2.

3.1.3 Sensitivity of the Model

When remembering the relation established for B , $B = \sqrt[4]{\frac{F_2 R^4}{D}}$, we can state that for lower B values we should encounter more rigid beams and vice-versa due to the presence of the flexural rigidity D in the denominator. Moreover, small changes in B can be associated with large changes in D spanning orders of magnitude due to the fourth root. Physically, this entails that for a lower B , we would have less deformation of the beams and vice-versa. Our model corroborated this physical phenomena and the results are displayed in Figure 7 where for a lower B we have a much higher D and thus, a more rigid beam.

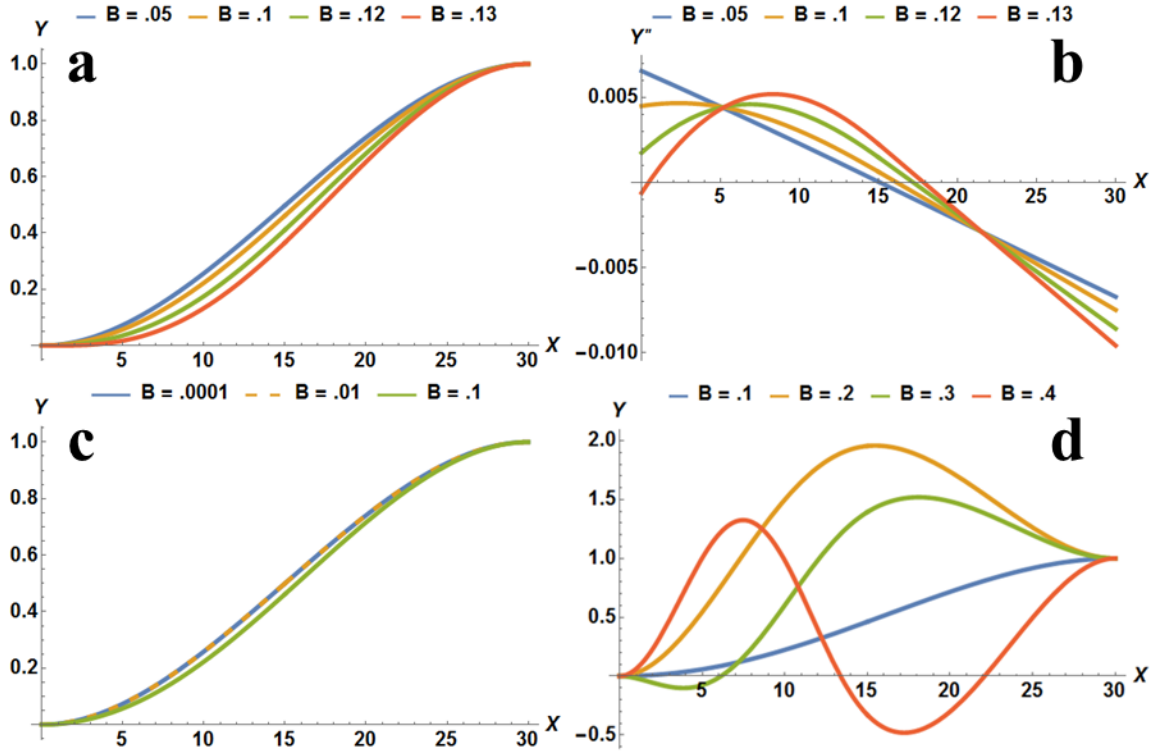


Figure 7. Sensitivity of the model against fitting parameter B . a) Deflection profiles with $\theta = \pi/2$, $L=30$, $\gamma=.62$, and varying B from .05 to .13. b) Second derivative of the deflection profile (curvature) with the same parameters as mentioned in a). c) Deflection profiles with the same parameters as in a), but varying B from .0001 to .1 to investigate the effects of B at very low values. d) Deflection profiles with same parameters as in a), but varying B from .1 to .4 to show that waves start to propagate in our solution above a certain threshold of B . For different inputted parameters, we will have different usable ranges of B .

In Figure 7.a, the crack length L and meniscus position l have been held constant while varying B to show that for more flexible beams (i.e. higher values of B), much more deflection occurs towards the X -axis. Figure 7.b displays the second derivative of the solutions shown in Figure 7.a and is a good representation of the curvature of the beam, which can be used to better visualize profile differences in areas of small deflection.

Despite the agreement between theory and physics shown by Figure 7.a and our expected profiles of the separated proboscis, our model does have limitations. Due to the trigonometric functions used in our solutions, either the profile is not affected by changes in meniscus length (the beam is too rigid) or the profile takes on a wave form propagating

at certain B thresholds which depends on l , θ , and γ . For instance, in Figure 7.c&d, we have kept L , l , θ , and γ constant and equivalent to what was used in Figure 7.a&b, but have varied the B parameter to determine regions of sensitivity, or lack thereof. We have found that for this particular set of parameters, little deviation can be found when moving from $B=.0001$ to $B=.01$ shown in Figure 7.c; only after reaching somewhere close to $B=.1$ do we see any noticeable deflection from its original location.

On the other hand, when using that same set of parameters and increasing our B to values above .1, such as the .2, .3, or .4 shown in Figure 7.d, waves start to propagate in our solution which is a non-physical phenomenon and, thus, indicates that for this particular set of parameters, somewhere between .1 and .2 lies a B threshold which we cannot surpass for a reliable fitting. Therein lies a difficulty of this model; the range of useable B values depends on the parameters inputted and changes slightly for each frame in each video. The sensitivity of the model to variations in parameters l , θ , and γ can be seen in Figure 8.a-c below where the meniscus front is indicated by the blue circles.

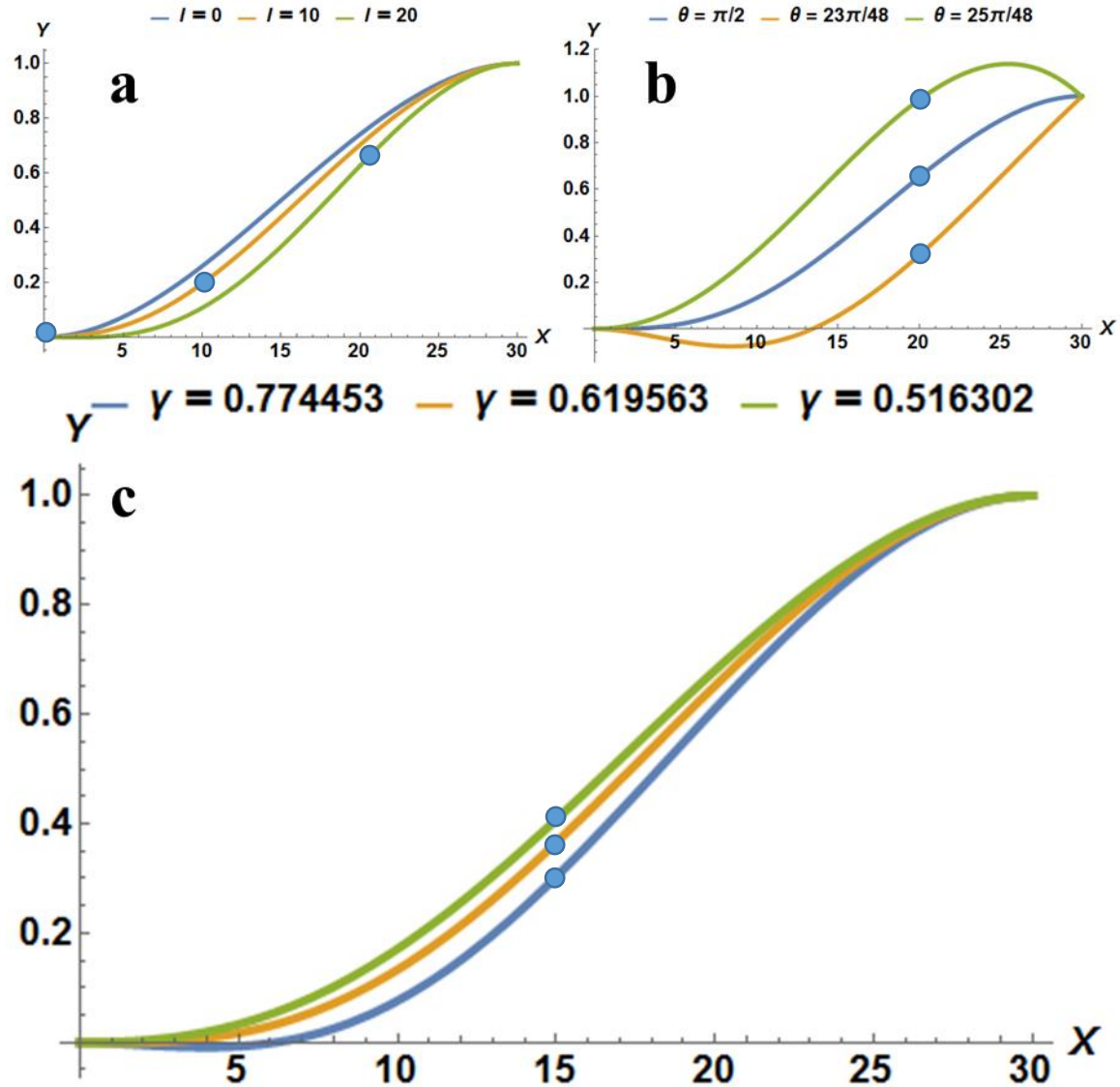


Figure 8. Sensitivity of fittings to other parameters where $L=30$, $B=.13$, and other parameters are varied. a) Varying length of the wet region from $l=0$ to $l=20$ for $\gamma=.62$ and $\theta = \pi/2$. b) Varying the angle θ from $\theta = 23\pi/48$ to $\theta = 25\pi/48$ for $l=20$ and $\gamma=.62$. c) While keeping other parameters stable and $l=15$, varying the dimensionless parameter γ from $\gamma=.52$ to $\gamma=.77$ by changing the values of the post radius in the parameter. For $\gamma=.52$, $.62$, and $.77$, post radii of $R=50 \mu\text{m}$, $62.5 \mu\text{m}$, and $75 \mu\text{m}$ were used, respectively.

Typically, if the profile of the graph goes below the X-axis, we will not be able to use that fitting because we would not have symmetry between the galeae at that point relative to this axis. An example of such a case is shown by the yellow line in Figure 8.b. In this case, we would have to numerically solve for a better L parameter to find a more

accurate fit or move to another frame in which the galeae touch the post at an angle closer to $\pi/2$. As one can see by Figure 8.c, when γ changes in a small amount we have slight deviations in the theoretical profiles. These small deviations were a result of using different separation post radii in the normalized γ parameter, but what if we were to create larger deviations in γ by, for instance, changing the surface tension of the wetting liquid used? In such a case, we would see much larger deviations in the profile and this can be visualized by Figure 9 where, when propagating the meniscus through different lengths up to L , the profiles using different γ values diverge and some become unusable.

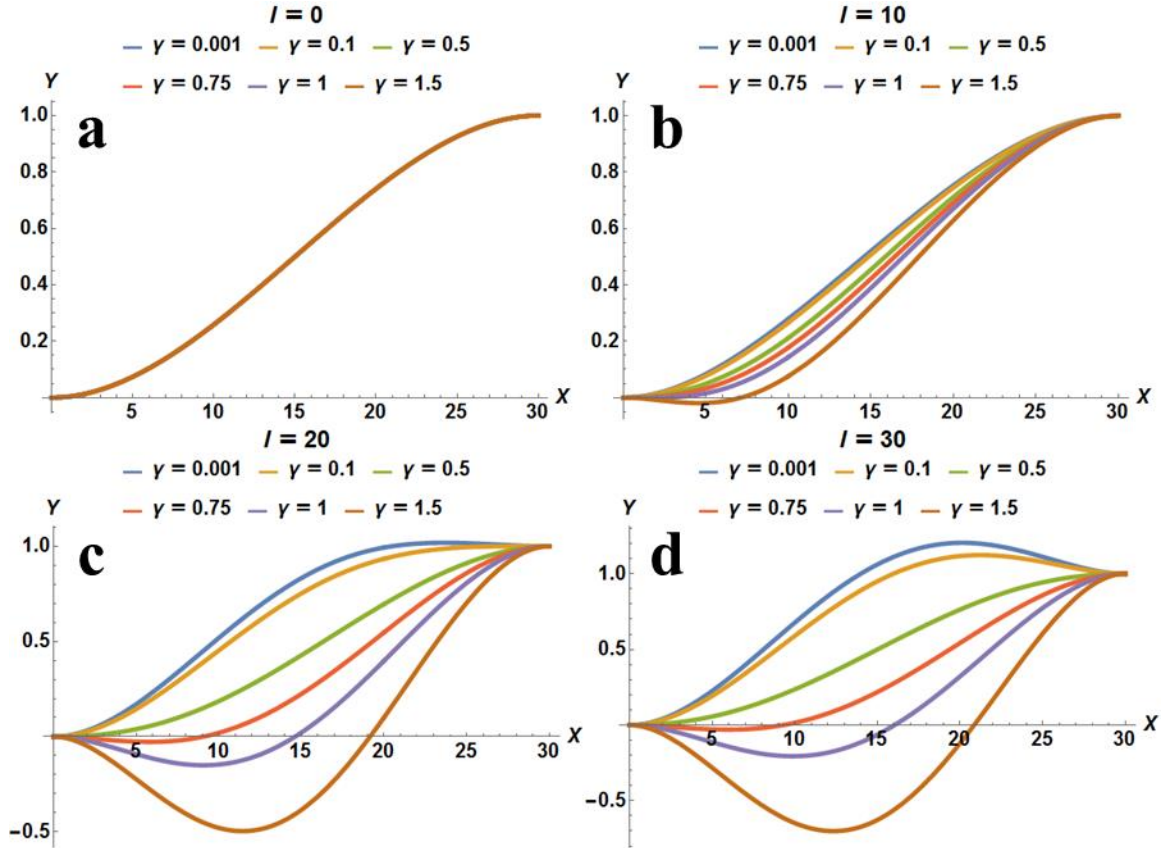


Figure 9. Displaying the effect of γ on the profile. Varying γ from .001 up to 1.5. Parameters used were $\theta = \pi/2$, $L=30$, $B=.13$, and l is being varied from a) $l=0$, b) $l=10$, c) $l=20$, and d) $l=30$.

However, when increasing L , say to $L=60$, which is the length scale typically found for longer proboscises, and keeping the ratio between meniscus length and crack length consistent with Figure 9, these γ values have a completely different effect (Figure 10). Additionally, B and θ were kept constant to easily compare the two figures.

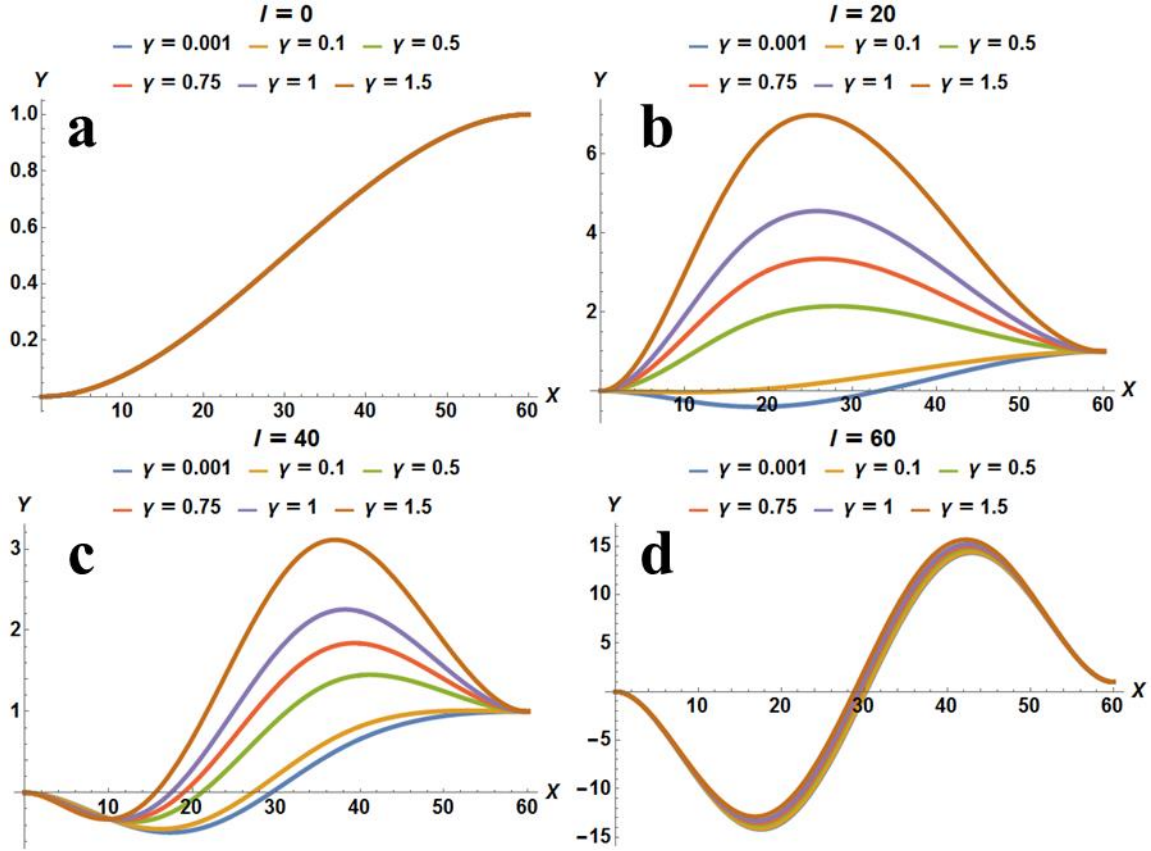


Figure 10. Displaying the effect of γ on the profile. In this case we are varying γ from .001 up to 1.5. Parameters used were $\theta = \pi/2$, $L=60$, $B=.13$, and l is being varied from a) $l=0$, b) $l=20$, c) $l=40$, d) $l=60$.

This comparison (Figures 9 and 10) indicates that there is a usable range of γ values available for each combination of B , L , l , and θ . These effective ranges are laid out in Table 1.

Table 1. Ranges of usable γ values when changing parameters B and L , or the crack length, are shown by $n1/n2$ in the table; any B - L pairs where waves always propagate in our solution are unusable and are shown by the red blocks in the table. This table can be read as follows: for a certain B - L pair, we have $n1/n2$ in the table and the $n1$, or number before the backslash, is the first γ value that can be used for this pair. Similarly, $n2$, or the number after the backslash, is the largest value that can be used for this pair. These $\gamma=n1$ and $\gamma=n2$ values were found by plugging the designated

B and L values into our solution, setting the meniscus length, or length of the wet region, equal to the length of the crack L, and then searching through γ values until profiles matching our physical case were found. If the profile dipped below the axis of symmetry (shown by the dotted line in Figures 4 and 5) at any point, then we couldn't use that γ value. Additionally, if waves start to propagate in our solution for a certain γ , then we also cannot use this γ value. This table was made for $\theta = \pi/2$ and values are subject to change for other θ values. The cells in green display that for different B-L pairs corresponding to different fiber shapes, lengths, and rigidities, ranges of gamma values can remain similar. Therefore, in our data fitting we have used $\gamma=0.62$ which seems to fit the most fiber types.

		Ranges of Usable γ Values							
		L							
		10	15	20	25	30	40	50	60
B	0.25	.8/3	.6/.74						
	0.2	1.5/6	.61/1.4	.55/.7					
	0.15	5/19	.9/4	.7/1.4	.6/.75	.48/.51			
	0.1	15/90	3/20	1.5/7	.8/2.5	.6/1.4	.6/.64		
	0.05	100/1000	35/250	15/92	5/35	3/18	1.5/6	.6/2.6	.8/1.5

Table 1 displays ranges of usable γ values for different sets of parameters, namely B - L pairs. In this case, the term ‘usable’ is defined by there being a lack of wave formations in our solutions and by deflection occurring from capillary force when propagating the saliva meniscus, l , through the entire crack length, L . This table can be read by first choosing an L and B value corresponding to the fiber being used, then go to the cell where the B -row and L -column overlap to see the minimum and maximum values of gamma (separated by a /). For example, if we have a crack length of $L=30$ and a $B= 0.1$, then the range of usable gammas would be between 0.6 and 1.4. The cells in green indicate that for different B - L pairs, the solution can have similar ranges of usable γ values and thus, in our experiments we will use a value that falls within all of the ranges laid out in the green cells, $\gamma=0.62$, in order to fit the most fiber types (lengths, rigidities, and shapes). Additionally, this table can be used to predict whether or not capillary forces would have an effect on

galeae of different shapes and sizes. For instance, for a very short and thick proboscis, say for $B=.05$ and $L=10$, our solution predicts that the capillary force created by the galeae will have an influence in a certain range of γ values, but for extreme cases the table would have to be extended outside of the range of L values shown here. However, before any of this was able to be used for data analysis, a program capable of gathering all of the experimental parameters from the videos and video analysis was needed and this is shown in the Data Acquisition and Analysis section, Chapter 3.2.

3.1.4 Experimental Design and Methods

3.1.4.1 Butterfly Storage and Feeding

Before any experiments could take place, we had to set up a consistent feeding procedure and schedule for the butterflies. At the start of every day, the butterflies were taken out of the refrigerator, where they were stored overnight, and their containers were cleaned with water while the butterflies were still inactive. Then paper towels were placed inside the containers and 15% sucrose-water solution (measured by mass) was pipetted onto the paper towels. The butterflies were allowed about an hour to feed *ad libitum* and afterwards one was chosen for testing. This particular butterfly was then hand-fed for 5-10 minutes (depending on butterfly) about 20 minutes prior to the test. Once testing on this butterfly was completed (at a room temperature of $\sim 22^\circ\text{C}$), it was placed back into its container, another butterfly was chosen for testing, and the same procedure was followed. At the end of the day, all butterflies were placed back into their respective containers (they were labelled according to the date of emergence) along with a wet, tightly-balled-up paper

towel of about 10 cm in diameter to keep the containers at adequate humidity levels and then these containers were placed back into the refrigerator until the next day. This procedure was followed on all weekdays until the butterflies passed away; however, they were not fed on the weekends. Butterflies were also used more than once for the splitting experiment but they were given ample time to repair their proboscis in their food containers before being used again or being placed back into the fridge.

3.1.4.2 Galeae Separation Procedure

The protocol of the proposed method to investigate the repair mechanism and material properties of the butterfly proboscis is as follows. The experiment is designed to investigate whether or not the liquid travels all the way to the tip of the proboscis or not, to determine if the saliva plays any noteworthy role in the repair of the proboscis, and furthermore, to gather the materials properties of the proboscis, such as the longitudinal modulus of elasticity.

First, we take a butterfly, insert it into a paper holder encompassing its legs, body, and wings, and then we restrain its wings with a clothespin to restrict movement as much as possible. Next, we uncoil its proboscis, straighten it out, and use two PDMS (Polydimethylsiloxane) strips, which are much larger than the proboscis, and slide the proboscis between the two polymer layers. The procedure up to this point is similar to that of a saliva collection method mentioned in a previous work (55). To keep the proboscis from sliding out of the PDMS while running experiments, we used a custom clamp made of spring steel (304V S/S S/T Alloy), which puts just enough pressure on the PDMS to

restrict proboscis movement while preserving the structural integrity of the proboscis. After completing the tasks specified above, a small split is created by hand with a round-tipped pin in both the dorsal and ventral legulae, the interlinking mechanisms of proboscises, of approximately 3 mm in length. This split is 3 mm from the tip of the proboscis initially. After the separation procedure, a wire-post of known diameter is placed between the two galeae to keep them from repairing into one component. Once the butterfly has been restrained properly with its galeae split around the post, a video acquisition program (Point Grey FlyCapture®) is run with a video camera (Point Grey Grasshopper GS3-U3-91S6C-C®) and lens (Meiji Techno® Short UNIMAC MacroZoom Lense MS-40) to capture the shape and deflection of the galeae around the post along with the meniscus propagation through the food canal. Subsequently, the post is moved towards the head in .5 mm steps every 10 seconds until the proboscis is fully separated; at this point it is translated in the opposite direction where one can study the repair mechanisms of the proboscis including the role of the menisci in proboscis self-repair.

After carrying out this experiment, a few important observations must be mentioned. First, moments after the galeae of a healthy butterfly are split, a liquid meniscus can be seen propagating back and forth through the food canal which indicates that the pump in the head is acting upon the saliva (Figure 11). Second, when studying the liquid meniscus between the two separated galeae, the contact angle between the galea and the saliva was much lower than 90° , which is indicative of a hydrophilic relationship. The hydrophilicity leads one to believe that the liquid wants to wet the entire interior surface of the food canal, and thus, supports the argument that capillary forces aid in the repair of the proboscis.

Figure 11.a&b portray the side and top view of the experimental schematic respectively, while c displays the meniscus propagation through the food canal of the live butterfly from experiment.

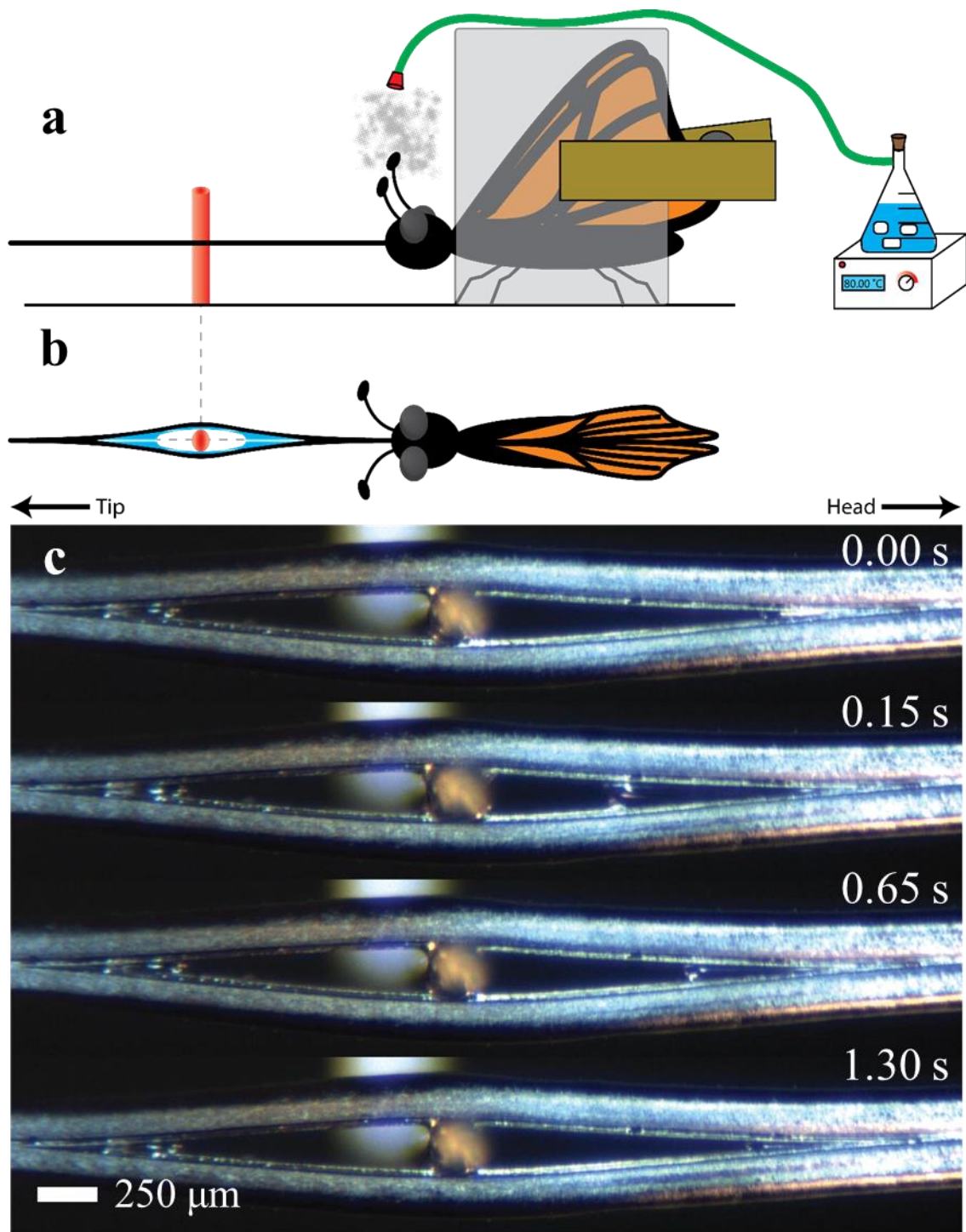


Figure 11. Experimental setup for proboscis separation and butterfly sedation. *a*) Side view of the setup where the butterfly is shown with its wings in paper (shown by the transparent rectangle) and held together with a clothespin (brown). The proboscis (black line extending off of the head of the butterfly) was extended and placed in a PDMS clamp (not pictured) to ensure stability of the galeae. The butterfly was sedated by using dry ice in a warm water bath (beaker on a hot-plate shown to right of the butterfly) to create a CO₂ gas which flowed out of the tube (green) via a showerhead

configuration to surround the butterfly with the gas. After sedation the butterfly recovers completely within a few minutes. b) Top view of the galea separation experiment where the blue regions between the galeae represent the saliva menisci and the red signifies the separation post. c) Experimental frames of the separated galeae showing saliva propagation of a butterfly in the “active” state, or before it has been dosed with CO₂.

By glancing at Figure 11.c, it can be seen that there are liquid menisci to the left (tip side) and right (head side) of the separation wire and one can glean that saliva has run all the way to the tip and consequently filled the food canal. This can be said with confidence due to the hydrophilicity of the interior of the food canal where a liquid finger running along the interior surface of the canal must travel all the way down to the tip and subsequently fill the canal; only afterwards can a liquid meniscus can be seen between the galeae on both sides of the wire.

To determine if this phenomenon is prevalent in other butterflies, we tested Monarchs (*Danaus plexippus*) and American Painted Ladies (*Vanessa virginiensis*) (56, 57) where, despite variability in size of the butterflies, shapes of the proboscises, and feeding habits, we saw similar results between both types; henceforth, we can say that it is common for butterflies to have the ability to completely wet their food canals with saliva. Furthermore, when taking Figure 12.c into account, liquid pumping from the butterfly can be observed; in the first frame at 0.00 s, there is no visible meniscus, but less than a second later liquid can be seen on both sides of the wire, and finally, at 1.30 s, the meniscus has receded on both sides.

We have seen another interesting phenomenon; some butterflies do not send liquid down to the tip of their proboscis. The butterflies producing saliva can be observed repairing their proboscis just minutes after the separation wire was withdrawn. However, in some butterflies, no meniscus can be found and their proboscises are dry and inflexible

which, after putting in the experimental apparatus, running the test, and drawing the post back to supposedly initiate repair, leads to a permanently separated and deformed proboscis. This further supports our hypothesis that the saliva not only aids in the repair of the proboscis, but seems to play an essential role in the self-repair of the galeae into one component.

3.1.4.3 Butterfly Sedation

To say with confidence that the saliva of the butterfly plays a significant role in the repair of the proboscis, we needed to separate the muscular forces from the capillary forces acting upon the galeae in the repair process. To accomplish this goal, we used a CO₂ sedation method (58) to minimize muscular action of butterflies (Figure 12.a). With the exception of the addition of CO₂, the second experimental procedure closely followed the steps outlined in Chapter 3.1.4.2 where the galeae were separated by a post moving in small steps. This additional step exploits the sublimation of CO₂ from a solid form (dry ice) into that of a gas by submerging pellets of dry ice into a warm water bath (~80 °C). The resulting CO₂ gas emissions were directed onto the head and body of the Lepidoptera for the purpose of sedation by positioning the outflow opening of the tube towards the body of the butterfly. This was specifically carried out when the saliva meniscus was close to, or touching, the post so that a long liquid column could be seen and it was carried out until the movement of the butterfly became inhibited, i.e., when there were no muscular actions or hydrostatic deviations in the galeae from hemolymph (blood of insects) propagation. Once no movements were visible, the butterfly was considered to be sedated. Afterwards,

the pressure produced by the butterfly onto the liquid column seemed to relax and the saliva wanted to retract towards the head, a process that results in the further separation of the galeae from which the effects of the capillary action can be gleaned. Thus, we are investigating the inverse situation of repair by observing the galea deflection of the sedated butterfly as the visible saliva meniscus is drawn away from the crack. The entire process was filmed via the same camera and software that was mentioned previously, Chapter 3.1.4.2, to maintain consistent quality in the videos at a frame rate of 40 fps.

3.2 Data Acquisition and Analysis

3.2.1 Video Editing

VirtualDub video editing software was used for simple video modifications such as cropping, rotation, and compression. To keep the videos consistent, we always used the same procedure as follows. First, we opened the video in VirtualDub, we went to the ‘video’ tab, and opened up the ‘compression’ window where we chose the ‘XVid compression codec’ with a target compression of 8 (between 0 and 20) which decreased the file size of the videos and helped them run smoothly in the LabVIEW program. Lower numbers for the target compression correspond to less compression and, therefore, a smaller decrease in file size. After compression, we went to the ‘filter’ tab and added a filter called ‘null transform’ which is a blank filter that doesn’t adjust the frames in any way until we hit the ‘cropping’ button. In the ‘cropping’ window, we selected the region of interest for the video by adjusting the height and width of what was shown in each frame; however, each quantity must be a product of four due to the compression algorithm used

in the XVID Codec. Post cropping, we went through the video and separated it into three parts; awake, sedating, and sleeping which correspond to regions in the video where the butterfly can be seen moving and pumping saliva between the galeae, where CO₂ gas can be seen moving across the camera and less movement occurs, and where there is no muscular action at all, i.e. the butterfly is completely anesthetized, respectively. These three segments were saved as separate video files with names matching their region in the video for easy identification later on in analysis. Once all of the segments were identified and saved, a new video was opened and the steps were repeated.

3.2.2 LabVIEW Video Analysis Algorithm

After successfully acquiring the experimental videos, we were met with the task of analyzing the frames in the videos by rotating the images so that the galeae were horizontal, determining the angle at which the galeae touched the post, and extracting the profiles of the galeae as *X-Y* coordinates. To do this, we created a custom code in National Instruments LabVIEW®, using many features from their Vision Development Module, and paired it with an analysis code developed in Wolfram Mathematica®. The data flow can be seen in Figure 12 below where the green boxes correspond to steps done in LabVIEW (outlined below) and the red ones relate to tasks completed in Mathematica (described further in Chapter 3.2.3).

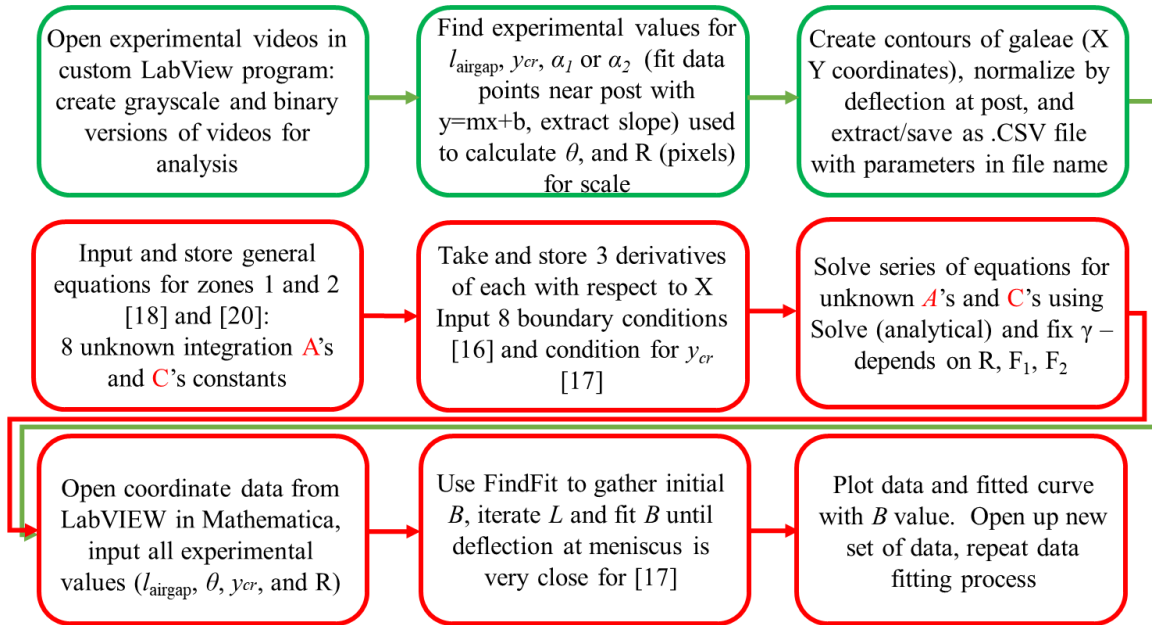


Figure 12. Flow-chart displaying data flow between LabVIEW (green) and Mathematica (red) to outline the general steps used in video/data analysis. The steps for LabVIEW analysis can be found in this chapter, but those used for data analysis in Mathematica can be found in Chapter 3.2.3.

The image processing procedure is as follows. First, we imported a video file by adding the desired file path to an input text string which was fed into IMAQ AVI2 Open and then to IMAQ AVI2 Get Info. This opens the video and gives information on each image such as the number of frames and image size.

Once the video has been imported, it was directed into an IMAQ Create where we created a mirror of a frame in the video and turned the RGB frames into grayscale for easier processing. Even though the frames were grayscale, they were still complicated by undesired artifacts such as a non-uniform background, the presence of the post behind the galeae, and other foreign objects due to the lack of controlled environment. Therefore, a set of binary (black and white) images was created via the IMAQ Local Threshold to deal with image complications and the window size for the threshold was left adjustable to best visualize each frame.

To gather the profiles of each galea in steps further down the road, the images had to be broken up into two adjustable rectangular regions of interest (ROI). One rectangle was used for each galea (stacked on top of each other) which spanned the entire horizontal length of the image. After creating a series of binary images composed of pixel values of 0 (black) and 255 (white) and creating the ROIs, these images were then rotated so that the proboscis was aligned as horizontally as possible.

Next, a contour line was created for each ROI by using the IMAQ Extract Contour algorithm and the direction of the contour search was set to top-to-bottom for the top galea in the image and vice-versa for the bottom galea. This contour algorithm finds the first largest length of contrast in each ROI, the external wall of each galea in this case, and maps them with contour lines so that the coordinates of the lines can be used to create plots for each individual galea. An example frame of the grayscale and binary, contoured images can be seen in Figure 13.

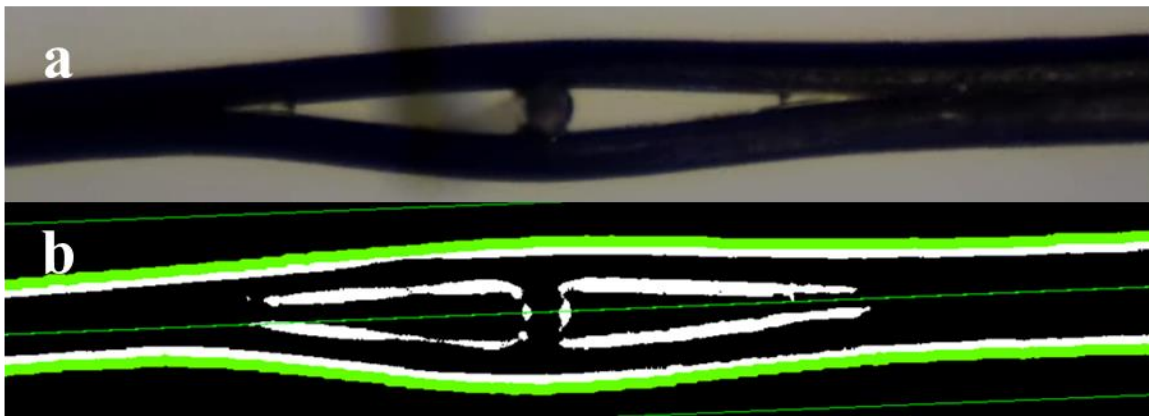


Figure 13. a) Original, sample image of the butterfly proboscis which had been split by a tungsten wire and b) the binary (black and white) image with contours (thick green lines) on the exterior of the proboscis and the regions of interest shown by the thin green rectangles situated at an angle parallel to the length of the proboscis.

Next, the extracted coordinates of the profiles were normalized by the quantity $(R + T_g)$ consisting of the post radius and the thickness of a galea at the post, which were both manually measured parameters for each video. Likewise, we manually measured the air gap between the meniscus front and the middle of the separation post, l_{airgap} . The rightmost point of this line (typically at the middle of the wire) was used as a cutoff point in the coordinates so that the normalized profiles only go up to the center of the post and therefore only extend to 1 on the Y -axis. The thickness of a galea at this point had to be introduced since the contours used were those of the exterior walls of the galeae; had we not done so, the profiles normalized by the post radius would've extended well past 1 and fitting would not have been possible. Once doing so, we were left with profiles of the top and bottom galeae, which could then be fitted by the solutions, [21] and [22].

In Figure 13, one can see the transition from grayscale to the binary, contoured image, which is necessary to gather data in future steps. However, in many of the frames (especially for active butterflies), the galeae deflections were not symmetric relative to the neutral axis between them (shown by the interface between the top and bottom regions of interest, thin green lines, in Figure 13.b). Furthermore, the galeae often touch the post at positions before or after the center of the separation post leaving the galea at a tangent angle other than $\frac{\pi}{2}$. Therefore, it was necessary to extract the slope of the tangent line between the galea and the post. This was done by taking the rightmost coordinate points (found from the contours), fitting them with a linear line, and then taking the derivative of that linear line. We then realized that there were three scenarios of galeae shape that had

to be taken into account and dealt with differently in order to gather the correct angle θ (Figure 5).

The first case is the one where the galea is laying on the post completely parallel with the X-axis; as such, the tangent angle θ is perpendicular to the horizontal axis, or $\theta = \frac{\pi}{2}$ and $\frac{dY}{dX} = 0$.

The second case was defined as the situation in which $\theta < \frac{\pi}{2}$ and, in such a case, the slope of the galea at the post is $\frac{dY}{dX} > 0$. Now defining angle α_1 as $\alpha_1 = \arctan\left(\frac{dY}{dX}\right)$ and using simple geometry we can see that $\theta = \frac{\pi}{2} - \alpha_1$ and hence, we are left with:

$$\theta = \frac{\pi}{2} - \arctan\left(\frac{dY}{dX}\right) \quad [31]$$

where $\frac{dY}{dX}$ is our measurable parameter from the experimental videos. Thus, our tangent angle θ for case 2 has been defined by [31]. By following similar methods for case 3 where

$\theta > \frac{\pi}{2}$ and therefore $\frac{dY}{dX} < 0$. The $\alpha_1 = \arctan\left(\frac{dY}{dX}\right)$ condition still applies, but here we must establish new angles α_2 and φ which are shown in Figure 9. The former can be

defined as $\alpha_2 = \pi - \arctan\left(\frac{dY}{dX}\right)$ while the latter can be found as

$\varphi = \frac{\pi}{2} - \alpha_2 = \arctan\left(\frac{dY}{dX}\right) - \frac{\pi}{2}$ and, thus, we can find the tangent angle for this case as

shown by [32] below.

$$\theta = \pi - \varphi = \frac{3\pi}{2} - \arctan\left(\frac{dY}{dX}\right) \quad [32]$$

Once all of the necessary experimental parameters have been measured, namely l_{airgap} and θ , a text string was created that included all of the important values along with the video name and frame analyzed for identification purposes. Then the normalized profile coordinates were exported as a spreadsheet file with the previously created text string as the file name. This file was then opened with a custom Wolfram Mathematica® program for further analysis.

3.2.3 Mathematica Data Analysis

The main goal for the Mathematica program was to use our mathematical model to analyze the normalized profiles that were extracted from the experimental videos via LabVIEW. The data flow in this program can be briefly described by Figure 12, but is laid out in detail as follows. First, the normalized equations [14] and [15] were inputted along with the set of boundary and continuity conditions shown by [16]. Then, two derivatives of [14] and [15] were taken for use with the boundary conditions. Then, the first two boundary conditions in [16] were used to solve for two of the integration constants for [18]. Additionally, the next two boundary conditions were used to solve for two of the integration constants in [20]. Thus, we were left with four integration constants and can use the four remaining continuity conditions in [16] to solve for them. The Solve function in Mathematica was used for all of the analytical solutions. Next, a piecewise function was

created and the analytical solution of [21] was set to be used in the domain $0 \leq X \leq l$, the portion of the galea described by Zone 1, while [22] was used from $l < X \leq L$.

Now that the piecewise function describing the galeae along the length of the proboscis was created, we can analyze the experimental data. First, we had to import the extracted coordinates (created in LabVIEW) into Mathematica and save all of the experimental parameters (present in each experimental filename) as certain parameters in Mathematica. Then, after inputting all of the experimental parameters into the theoretical piecewise solution, the FindFit command was used to fit the experimental curve and gather B which could later be used to calculate the flexural rigidity D of the proboscis. This FindFit algorithm numerically minimizes the sum of residuals squared, which is a summation of the differences between the experimental and theoretical deflection over all data points, i , $\sum_i (Y_i^{\text{exp}} - Y_i^{\text{th}})^2$ where Y_i^{exp} and Y_i^{th} are the experimental and theoretical deflections at point i . However, one difficulty we had here was that the length of the crack, L , is moveable and unknown and therefore, we were left with a moving boundary problem. Thus, we needed to create a numerical, iterative technique using the previously gathered B parameter as the initial fitting value and the largest value in our coordinate array as the preliminary L . This is possible since the deflection in $Y(X)$ is normalized by R and hence, the largest value in the array will always be the length of the galea up to the post. After this we could start the iteration process with L as our iterative term and [17] as our iterative condition to be met in the While loop. Depending on the accuracy of the first fit, we could adjust the iteration step according to the distance required to create a better fit. However, we usually gathered accurate fittings ($R^2 > .95$) with our initial fitting method, so when

running our data in the iterative process we would receive values that are the same as with the initial; therefore, we only used the iterative process when necessary, for instance, when the initial fit was poor. Through these means, we've collected all of the data in Chapter 4.

CHAPTER FOUR

RESULTS AND DISCUSSION

4.1 Materials Properties of the Butterfly Proboscis

4.1.1 Saliva Movement Paradox: Where does the saliva go when receding at the tip?

During this experiment, a saliva meniscus can be seen on each side of the post indicating that it travels to the tip prior to the splitting of the proboscis. After separating the galeae, saliva gets trapped on the tip-side (Figure 11.c) and a meniscus can be seen propagating back and forth. However, when the butterfly is sedated, the saliva meniscus can be seen retracting towards the tip, which creates the following questions: why does the saliva move to the tip and is there some reservoir where the saliva can move? If so, is this reservoir a feature of the proboscis, similar to a pore, or is the saliva moving elsewhere?

To answer these questions, we modified the previous experiment described in Chapter 3.1.4. The experiment remains largely the same in that the butterfly was placed in the holding apparatus, the proboscis was straightened out, and the tip was placed in the PDMS clamp; however, the main difference here is that the proboscis was not split. Instead, the enclosed tip was brought under the same PointGrey camera and focused on through the transparent PDMS. After carrying this out, almost immediately the saliva was seen leaving from the tip region of the proboscis and moving into the small opening between the PDMS layers. This process is illustrated in Figure 14. This simple experiment demonstrated that the saliva withdrawal from the post at the tip side of the proboscis is due to capillary wicking of the saliva between the two PDMS layers, and thus, we conclude that the reservoir we were searching for was actually the gap in the PDMS clamp.

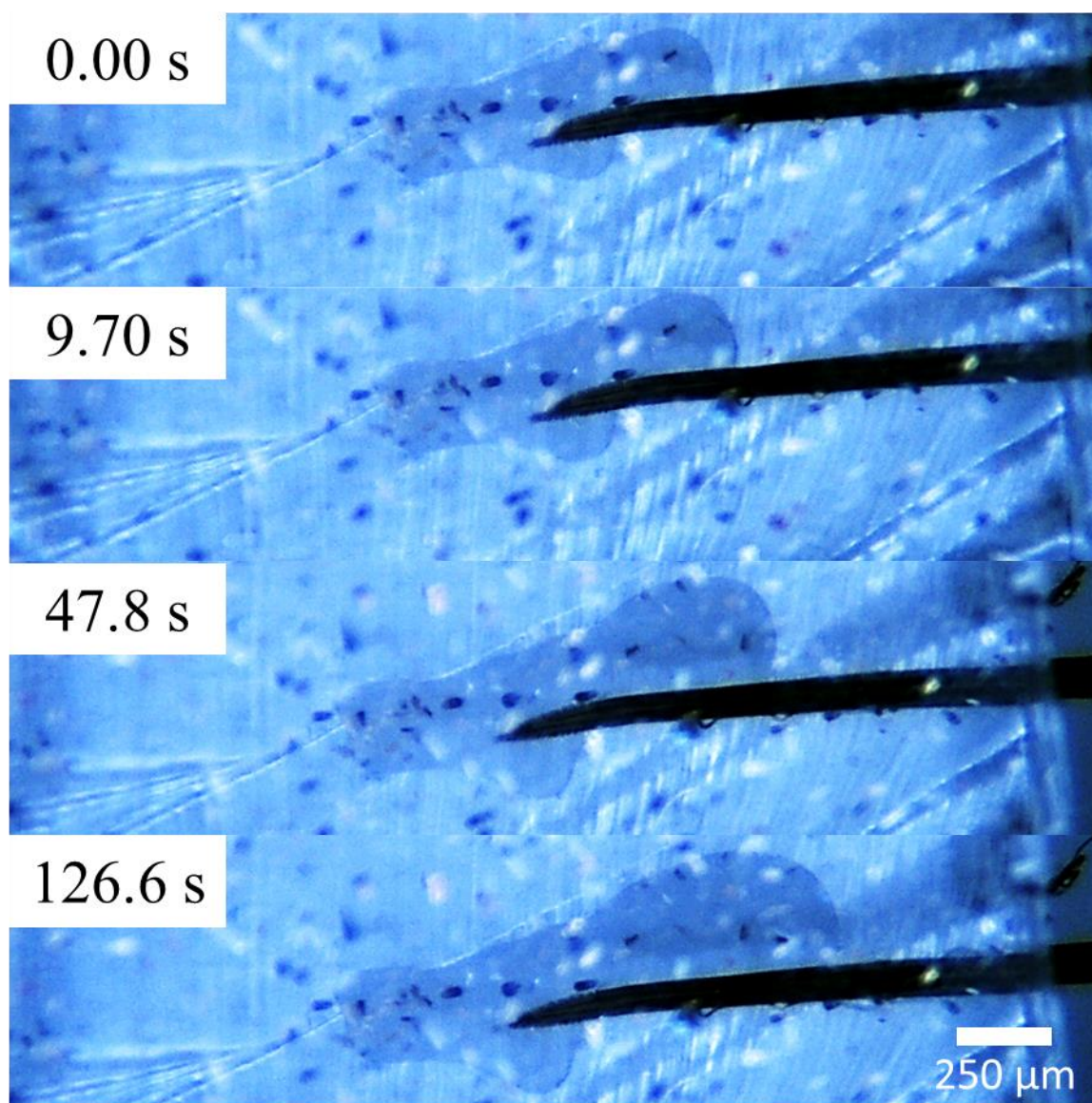


Figure 14. Displaying the escape of saliva from the tip of the proboscis and its propagation inside of the PDMS clamp over time. The video was recorded at 30 FPS.

This saliva propagation into the PDMS clamp piqued our interest and led us to study the kinetics of these snapping-off moments in the videos of sedated butterflies further due to the supposed correlation between the two. To do so, we used the custom LabVIEW software to measure the air gap between the center of the post and the meniscus front for

each frame in the snapping period of the videos. To measure the retraction length, the change in air gap length from the first frame to the desired frame was quantified for each frame and this quantity was denoted as the Meniscus Retraction Length, L_R . The retraction length normalized by the radius of the post, $62.5 \mu\text{m}$ in this case, plotted against time can be seen in Figure 15 and the data points are shown by the hollow circles.

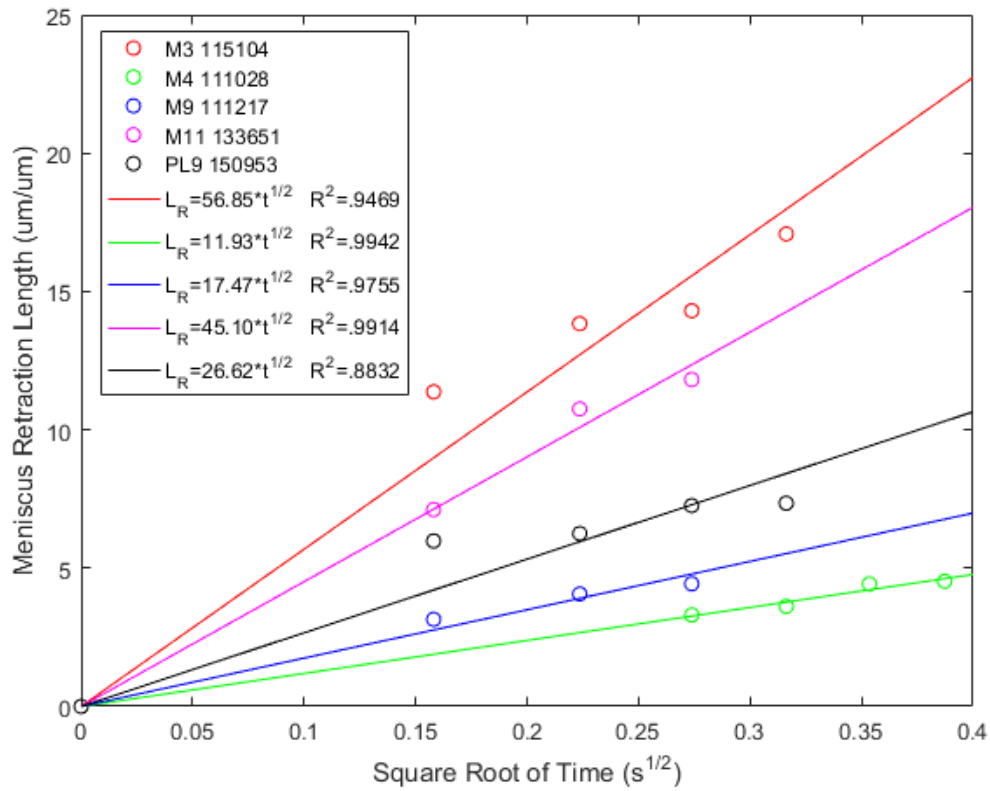


Figure 15. Displaying the increasing of the meniscus retraction length (L_R) (normalized by the diameter of the post) over time (t) and where the L_R is measured by the change in distance between the meniscus front and the center of the post for butterflies in the sedation process. The data (hollow circle points) were fit with square-root-of-time kinetics as can be seen by the solid colored lines. In this graph, each color is representative of a single butterfly in a single video and the data points were taken at each frame in the videos where saliva retraction was seen.

The data were then fitted with square-root-of-time kinetics, assuming capillary flow into the small gap shown by [33] and the solid, colored lines in Figure 15. In this case, a is the fitting parameter and t is time.

$$L_R(t) = at^{1/2} \quad [33]$$

As one can see in Figure 15, we have good agreement between theory and experiment, which validates our hypothesis that capillary wicking of the saliva into the gap in the PDMS clamp from the liquid column near the tip does occur. However, the wicking of the saliva does not occur at constant rates as can be seen by the wide distribution of data as well as their respective fitting parameters (shown in front of the $t^{1/2}$ in the legend inside of Figure 15). This mystery will not be addressed in this work.

4.1.2 Results from Data Fitting and Mechanical Testing of Galeae

After the video analysis was completed, we performed the data fitting with the solutions [21] and [22] to gather the desired materials parameters of the butterfly proboscis, which lie in our fitting parameter B . The data fitting algorithm is a multiple step process that can be found described in Chapter 3.2. Figure 16.a-c shows a variety of satisfactory fits for the curves extracted from butterflies undergoing the sedation process (shown in blue data points). The shape of the sedated butterfly's proboscis did not change much between frames due to the lack of muscular action; this lead to relatively unchanging profiles between frames. However, the shape was different between the bottom galea and the top galea due to the asymmetry of the galeae with respect to the neutral axis. Due to this asymmetry, we have left these data out of the final data set, but they are still useful for illustrating the robustness of our model.

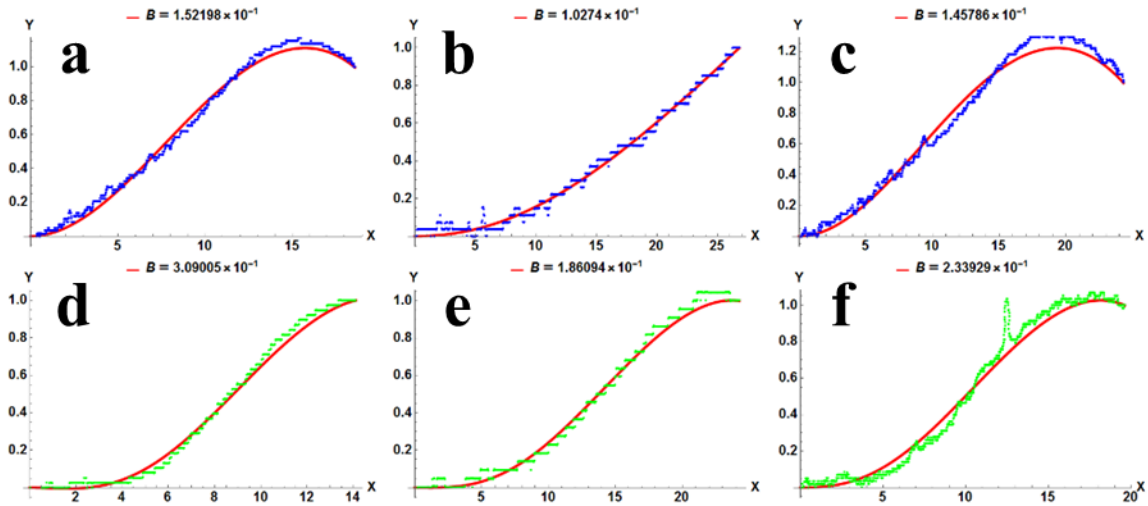


Figure 16. Butterflies undergoing sedation process: a) M213 141820 Sedating BG Frame 123, b) M213 141820 Sedating TG Frame 142. Video 2: c) M213 141820 Sedating BG Frame 124. Active butterflies: d) M12 120131 Awake BG Frame 0, e) M12 120131 Awake TG Frame 14, and f) M18 170354 Awake BG Frame 301.

Now that we have discussed the sedated butterflies, we can move on to a more difficult scenario, at least in the data fitting sense, when the butterflies are active. The butterflies are considered active when little or no CO_2 has been used to sedate them and the proboscis is twitching or moving in the videos. These deviations in contour profile led to difficulties in data fitting, particularly because muscular action in the proboscis prevents the galeae from having the desired shape as established by the Euler-Bernoulli beam model. For instance, if the slope of the galeae at the start of the fitting region (left side) is not close to zero, as our boundary conditions require, or if the butterfly manually separates the galeae in the middle of the fitting region, we will have difficulty in getting a satisfactory match between the data and the fit. With that said, in frames where the butterfly does not seem to apply large muscular forces, we can see agreement between the experimental and theoretical profiles as shown by the green data points in Figure 16.d-f.

Next, we must discuss the variability of the B parameter found for both species of butterflies tested and the state that they were tested in (active, sedating, and sleeping). The average B values from each butterfly in all three states can be found in Figure 17.

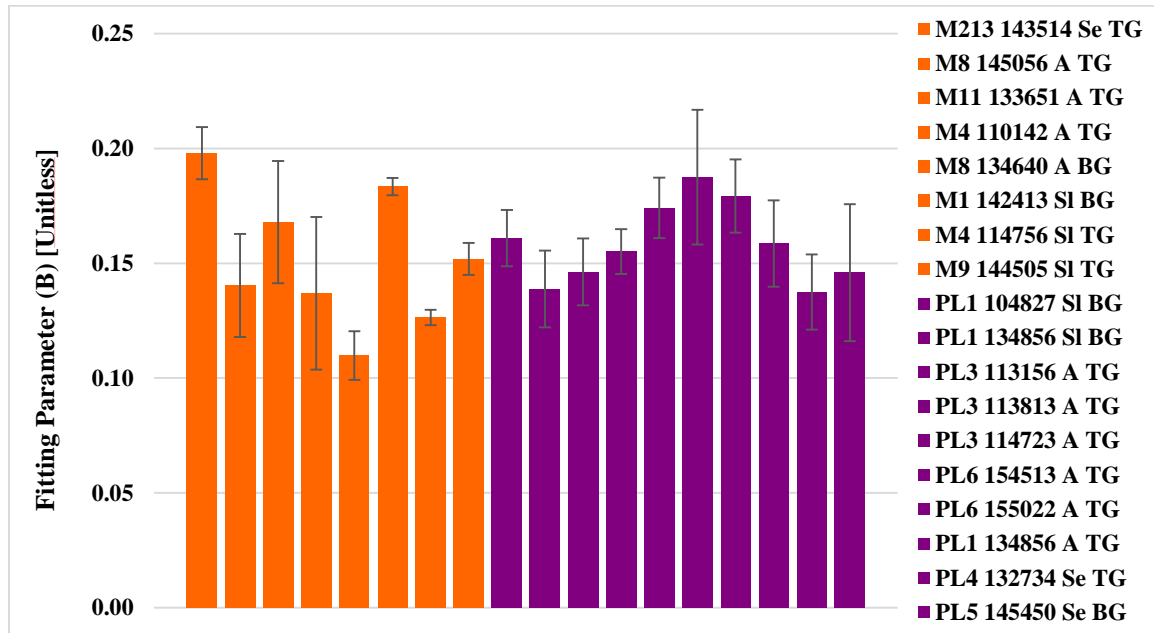


Figure 17. Displaying the average B values for Monarchs (shown in orange and M on the legend) and Painted Ladies (shown in purple and PL on the legend) in the active state (A on legend), sedating state (Se), and sleeping (anesthetized) state (SI). It can be seen by the error bars overlaying the data bars that for the case of active butterflies, there is much more variability than there is for sedated butterflies. Also, it is worth noting that TG and BG signify Top Galea and Bottom Galea, respectively.

In this set of bar graphs, one can see the B values found for each particular butterfly species and number, video number, and galea (top or bottom). The Monarchs are shown by the orange bars and the Painted Ladies are shown by the purple bars. At this point it is also worth clarifying how the legend can be read. As an example, let us choose the first item on the legend (from top to bottom), namely ‘M213 143514 Se TG’. In this line of text, ‘M213’ represents Monarch #213 that was tested, ‘143514’ is a string of numbers generated by the video camera when acquiring a video for this particular butterfly and is used for video identification purposes, ‘Se’ indicates that the butterfly was being sedated

in this video, and ‘TG’ states that the top galea was tested (Figure 17). In this figure, it can easily be seen that active, sedating, and sleeping (fully anesthetized) butterflies of both species, Monarchs and Painted Ladies, span about an order of magnitude, from $B=.07\sim.19$, which means that we can use this model for sedated butterflies as well as active ones. However, the variability of active butterflies is much greater than that of sedating or sedated butterflies. For instance, if observes the two sets of data, one awake butterfly, M11 133651 A TG, and one anesthetized, PL1 104827 SI BG, the standard deviations of the B for the awake butterfly is about twice the size of the standard deviation for the sleeping butterfly. This is possibly due to the changing muscular actions inside of the proboscis for the active butterfly and therefore the dm/dx which was previously ignored (Chapter 3.1.2) would have to be taken into account in further iterations of the model. Furthermore, the overall average B including both Monarchs and Painted Ladies was $B_{overall}=.1520$ with a standard deviation of .0161 while the average B for Monarchs and Painted Ladies were $B_M=.1519$ and $B_{Pl}=.1520$ with standard deviations of .0148 and .0171, respectively. All table of collected B values and standard deviations can be found in Table 2 below.

Table 2. B values (data shown in Figure 17) collected for each butterfly with their corresponding standard deviations. The standard deviations were found by considering each video and taking measurements of B frame by frame. In this data set, 6 Monarchs and 5 Painted Ladies were tested to make up the 8 and 10 videos tested for each species, respectively. All other collected data can be found in the appendices.

Monarch	B	Painted Lady	B
M213 143514 Se TG	0.20	PL1 104827 SI BG	0.16
Standard Deviation	0.01	Standard Deviation	0.01
M8 145056 A TG	0.14	PL1 134856 SI BG	0.14
Standard Deviation	0.02	Standard Deviation	0.02

M11 133651 A TG	0.17	PL3 113156 A TG	0.15
Standard Deviation	0.03	Standard Deviation	0.01
M4 110142 A TG	0.14	PL3 113813 A TG	0.16
Standard Deviation	0.03	Standard Deviation	0.01
M8 134640 A BG	0.11	PL3 114723 A TG	0.17
Standard Deviation	0.01	Standard Deviation	0.01
M1 142413 SI BG	0.18	PL6 154513 A TG	0.19
Standard Deviation	0.00	Standard Deviation	0.03
M4 114756 SI TG	0.13	PL6 155022 A TG	0.18
Standard Deviation	0.00	Standard Deviation	0.02
M9 144505 SI TG	0.15	PL1 134856 A TG	0.16
Standard Deviation	0.01	Standard Deviation	0.02
		PL4 132734 Se TG	0.14
		Standard Deviation	0.02
		PL5 145450 Se BG	0.15
		Standard Deviation	0.03
Monarch Average	0.1519	Painted Lady Average	0.1520
Standard Deviation	0.0148	Standard Deviation	0.0171
Overall Averages			0.1520
Overall Standard Deviation			0.0161

Now that the non-dimensional B values have been found from fitting, we can calculate the Longitudinal Young's Modulus of Elasticity E of the galeae for Monarchs

and Painted Ladies by solving the relation $D = \frac{F_2 R^4}{B^4} = EI$ for E , inputting an estimated value for the area moment of inertia I , using the known post radius R of 62.5 μm , and entering the calculated values for the force per unit area F_2 with a value of 11010.9 N/m^2 .

For moment of inertia calculations, the galea was approximated as a hollow semi-ellipse with a half-circle cut out of it to account for the food canal. The derivation for the equation used can be found in supplemental information, but the simplified model of the equation (shown before subtracting out overlapping regions) is in equation [34]

$$I_y = \frac{1}{8} \pi \left(R_{g1}^4 - (h - R_{g1})(h - R_{g2})^3 + R_{g1} R_{g2}^3 - (h - R_{g1})^4 \right) \quad [34]$$

where R_{g1} , R_{g2} , and h are the radius of the minor and major axes of the ellipse and the thickness of the walls respectively. The radius of the food canal in our simplified case is considered to be the same as the radius of the minor axis of the ellipse and is thus taken to be $R_{g1}=35 \mu\text{m}$, the average radius of the food canal in the distal region of the proboscis with a standard deviation of $\pm 5 \mu\text{m}$ as established in (38). In our estimate for I , we have also used $R_{g2}=100 \mu\text{m}$ as the radius of the major axis of the ellipse and $h=20 \mu\text{m}$, which are good parameter estimates for the distal region. This leads to an estimated moment of inertia of $I = 1.13 \times 10^{-17} \text{ m}^4$ which is to be used in the E calculations. Using this value for I and those mentioned previously for R , F_2 , and B , we have calculated E (Table 3). This table displays the range of expected Young's Modulus of Elasticity values for Monarchs and Painted Ladies.

Table 3. The Modulus of Elasticity, E , values calculated from equation [30] with average B values for each butterfly species tested. The column indicated 'Average' is calculated with the Average B value for each species whereas

the 'Low Estimate' and 'High Estimate' are calculated with the upper and lower B values that would be found based on our standard deviation respectively. For further clarification, higher B values lead to lower E values.

MODULUS OF ELASTICITY (E) [MPa] – Tip			
Butterfly Species	Average	Low Estimate	High Estimate
Overall	27.88	18.63	43.66
Monarch	27.96	19.28	42.14
Painted Ladies	27.83	18.18	44.81

Now, one can compare the calculated E values for Monarchs and Painted Ladies to those found by tensile testing. A Dynamic Mechanical Analyzer (TA Instruments© DMA Q800-0907) was used for tensile testing experiments with the help of the MS&E materials characterization expert, Kim Ivey. The DMA was run in a controlled strain rate mode (0.25% strain/min to 25% at temperature of 22°C) where it simulated an ordinary tensile test by extending a sample and measuring the resulting force until the sample fractures or slips out.

These experiments were run on dead butterflies (usually no longer than two days after they perished) and the galeae were separated, similarly to how it was described in Chapter 3.1.4, severed from the head of the butterfly, and then the tip of each galea was placed in an epoxy putty (J-B WELD® PlasticWeld™ or SteelStik™, succeeded with both) that was attached to a plastic clamp with flat external surfaces to prevent slippage of the sample during testing. During testing, the sample typically extended to between 1% and 3% strain before breakage occurs. All DMA data can be found in the appendices. Figure 18 shows a sample of the data taken from DMA.

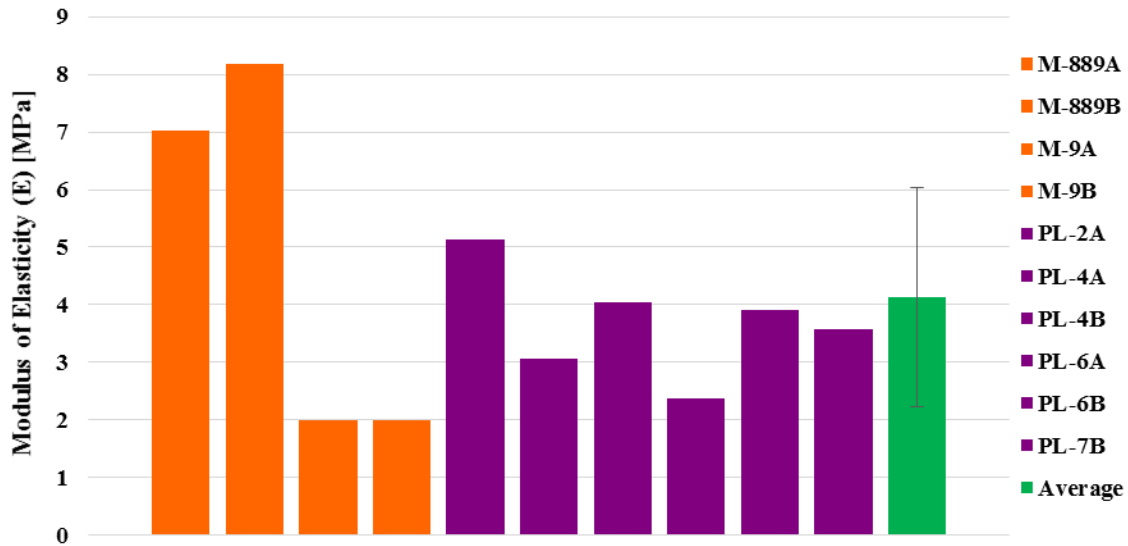


Figure 18. Modulus of Elasticity values taken from DMA tensile testing. This bar graph follows previous conventions; orange represents monarchs tested, purple represents the painted ladies tested, and the green represents the average modulus of all butterflies tested with an error bar showing one standard deviation above and below the average. The legend can be read as such; M stands for Monarch and PL stands for Painted Lady, the number afterwards represents the number of butterflies tested, and A or B signifies the galea that was tested from that butterfly.

When comparing the results from our method to the DMA, one can see that our estimations from curve fitting are an order of magnitude greater than that of the DMA. There may be two possible reasons for this: 1. The butterfly tested in our galea separation experiment is thought to have had an internal pressure created by the hemolymph (blood of butterflies) that flows inside the proboscis. This internal pressure is also thought to increase the rigidity of the galeae and thus, the effective modulus of elasticity that is measured by our experiment would also increase. In the DMA experiments, we were testing proboscises that were severed from the head of the dead butterfly and the hemolymph was dry, so we did not have any pressure from the hemolymph. Measuring the pressure inside the galeae is not in the scope of this work, so this question will remain unanswered. 2. The modulus E calculations from our data fitting with B are sensitive to

the moment of inertia I that is inputted into the equation $E = \frac{F_2 R^4}{B^4 I}$, so since we are using parameters for the moment of inertia that are found near the distal region (or tip) of the proboscis, it would make sense that E would be larger than what is experienced with experiments. Therefore, if we were to use typical parameter values that can be found in the knee region (middle of the proboscis), we should be able to increase I and thus decrease E to garner better agreement between our theoretical results and mechanical testing. These parameters can be found in Table 5. Additionally, new estimations for E with the moment of inertia near the middle of the proboscis can be found in Table 4.

Table 4. Comparison between the Modulus of Elasticity E values found from the theoretical curve fitting and the mechanical testing after calculating the moment of inertia with parameter values for $Rg1$, $Rg2$, and h found near the middle of the proboscis. Values for these parameters can be found in Table 5. This table shows that when using shape estimates for the galeae near the middle of the proboscis instead of the tip, we find much better agreement between our theory and mechanical experiments in both the averages and the lower and upper bounds (when using one standard deviation to calculate them).

MODULUS OF ELASTICITY (E) [MPa] – Middle			
Butterfly Species	Average	Low Estimate	High Estimate
Overall	3.14	2.10	4.92
Monarch	3.15	2.17	4.75
Painted Ladies	3.14	2.05	5.05
MODULUS OF ELASTICITY (E) [MPa] – DMA			
Average	4.13	2.24	6.03

As one can see from Table 3, the calculated E values of the butterfly proboscis for both Monarchs and Painted Ladies are similar, and when calculated with an I near the middle of the proboscis, are in agreement with the values from tensile testing with the DMA and thus, we can glean from these data that the pressure of the hemolymph inside the galeae does not play a large role in the stiffness of the organ. For reference, this range of E values (under 10 MPa) is a few orders of magnitude lower than that of human hair,

which has an average value of about 3 GPa based on Quan’s observations (59). Therefore, based on our calculations, we can say that in nature these butterflies, Monarchs and Painted Ladies, do not need a rigid proboscis for drinking nectar from flowers and actually, the flexibility of the proboscis facilitates the coiling and uncoiling needed for feeding as well as the assembly/repair process. However, there are butterflies with much shorter or longer proboscises than those studied here and these butterflies may need a more rigid proboscis for purposes such as insertion into narrow flower tubes. The parameters used in the modulus of elasticity calculations can be found tabulated in Table 5 below.

Table 5. Tabulated parameters used in modulus of elasticity E calculations where the symbol is shown in parenthesis and the corresponding units are shown in brackets.

FITTING PARAMETER (B) [Unitless]		
Butterfly Species	Average	Standard Deviation
Overall	0.1520	0.0161
Monarch	0.1519	0.0148
Painted Ladies	0.1520	0.0171
OTHER PARAMETERS USED IN CALCULATIONS		
Parameter Name and (Symbol)	Values used in calculations	[Units]
Radius of the separation wire (R)	62.50	[μm]
Force Per Unit Area (F_2)	11010.90	[N/m ²]
Tip – Distal Region of Proboscis		
Moment of Intertia (I_y)	1.13×10^{-17}	[m ⁴]
Radius of the Minor Axis of the Ellipse (R_{g1})	35.00	[μm]
Radius of the Major Axis of the Ellipse (R_{g2})	100.00	[μm]
Wall Thickness (h)	20.00	[μm]
Middle – Knee Region of Proboscis		
Moment of Intertia (I_y)	1.00×10^{-16}	[m ⁴]
Radius of the Minor Axis of the Ellipse (R_{g1})	40.00	[μm]
Radius of the Major Axis of the Ellipse (R_{g2})	200.00	[μm]
Wall Thickness (h)	27.00	[μm]

4.1.3 Adhesion Forces Between the Galeae

The galeae separation experiment was first designed to determine the mechanical properties of the butterfly proboscis, but by investigating the shear forces in the galea, or beam, along its length, we can actually gather the normal force created by the contact between the galeae and the post and consequently determine the adhesion forces at the crack location between the galeae and the capillary forces bringing them together. Most of the forces are acting in the orders of magnitude between mN and μN , which is what was expected for fibers of such small size, capillary forces, and small deflection of the galeae from the post. Additionally, when looking at the capillary force data, as the meniscus length l , or the length of the wet region, increases, we have an increase in magnitude of our capillary force, which can be seen in Figure 19. The capillary force, F_c , was found from an integration of forces from the crack position ($X=0$) up to the meniscus; therefore, all capillary forces in our experiment were taken into account. These calculations can be found in Chapter 3.1.2.5.

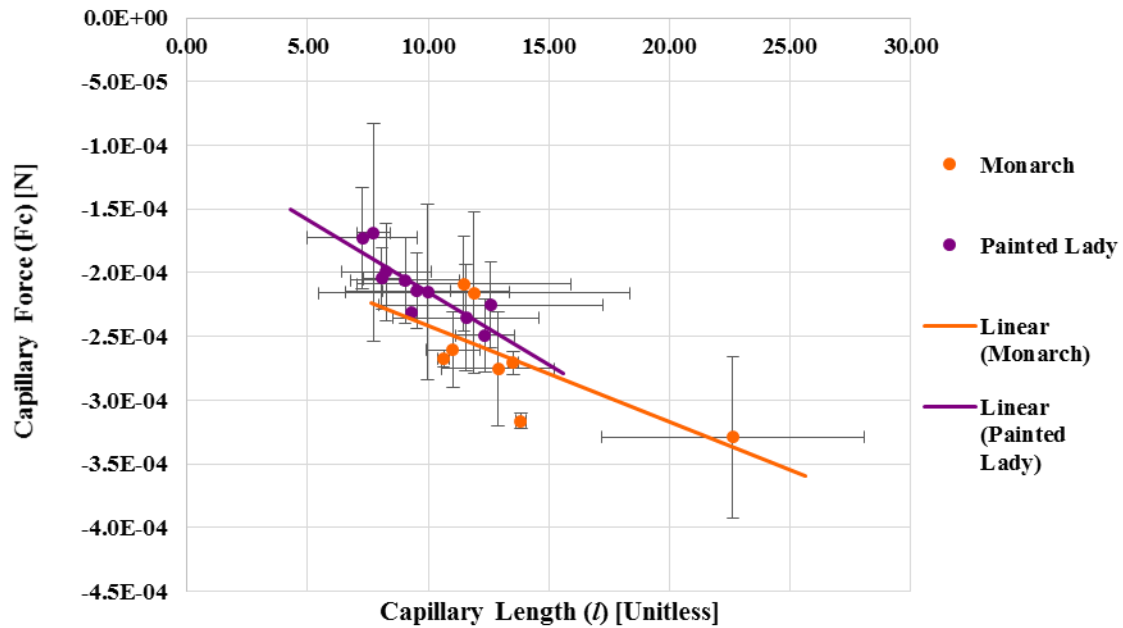


Figure 19. Displaying the Capillary force (F_c) against the length of the wet region along the length of the galeae. As capillary length increases, we have a corresponding increase in magnitude of capillary force and, thus, a greater restoring force. In this figure, the orange and purple dots represent data from Monarchs and Painted Ladies, respectively. Additionally, the error bars in the x and y directions are showing one standard deviation for each of the data points. The larger error bars correspond to tests on active butterflies while those with smaller error bars are typically sedated or sleeping butterflies. The linear trendlines were added to guide the eye as to how the data was acting. This raw data can be found in supplemental information.

Now we can introduce the adhesion force in the horizontal and vertical directions with Figure 20. These forces were gathered from the shear force profile along the length of the beam (third derivative with respect to displacement) and these calculations can be found in Chapter 3.1.2.

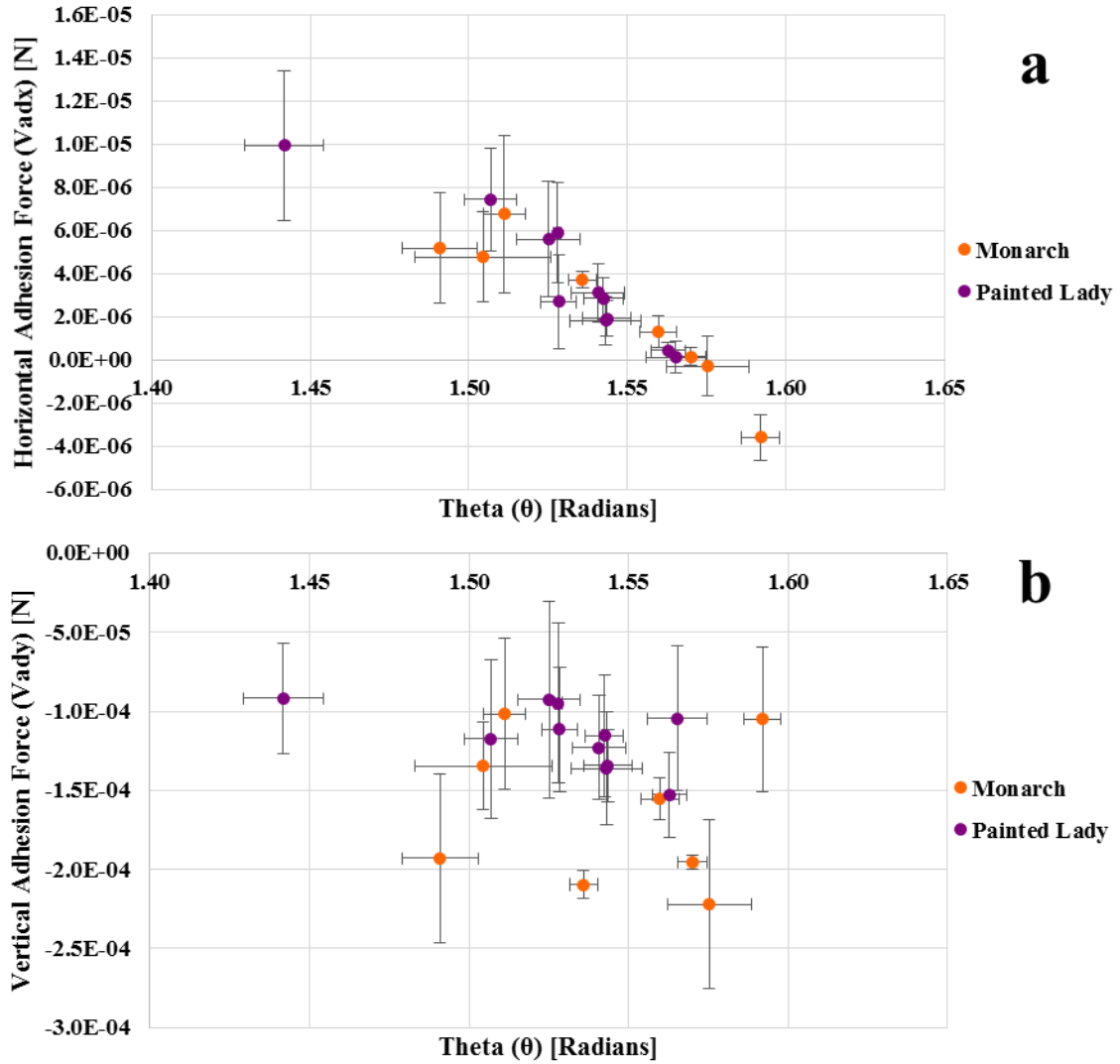


Figure 20. Adhesion forces plotted against θ in the a) Horizontal direction (V_{adx}) and b) Vertical direction (V_{ady}). In these figures, orange and purple dots correspond to tests with Monarchs and Painted Ladies, respectively. Error bars use the same conventions as in previous figures.

The horizontal adhesion force data shows a noteworthy trend (Figure 20.a). As θ , or the angle between the normal vector at the point of contact between the galea and post and the axis of symmetry goes to $\pi/2$ (~ 1.57 radians), the horizontal component of the adhesion force diminishes to zero and actually, as the angle surpasses $\pi/2$, we get negative values. This is displaying exactly what was expected for the three cases that were

mentioned previously. For instance, at angles below $\pi/2$, our horizontal adhesion force is pointing towards the post and thus creating a compression scenario in the beam. On the contrary, for angles above $\pi/2$, we see a reverse in the sign showing that the force is acting in the opposite direction and thus, the case has switched to the tensile scenario. Likewise, in between these two cases, we are left with extremely small adhesion forces that tend to zero as we get closer and closer to $\pi/2$; and therefore, we have only vertical components of the forces in this case as expected.

The vertical adhesion data is not easy to interpret (Figure 20.b). It was conjectured that as θ tended to $\pi/2$, we would see an increase in vertical adhesion forces due to the horizontal component going to zero. This is not the case for a couple of reasons. First, since the vertical component is at least an order of magnitude larger than the horizontal component in most of our cases, the increase in vertical force from the decrease in horizontal force as the angle moves towards $\pi/2$ would be much smaller than that of the original vertical force and thus, the deviation would not be noticeable in our data. Second, since the profile of the proboscis is unique in every video and the vertical adhesion force is directly related to this profile, it is likely that we would have a scatter of data due to this and, thus, we do not have any direct trends between our vertical adhesion force and θ . However, the range of vertical adhesion data points lie between 0.09 mN and .25 mN (Figure 20.b), which coincidentally sits in the range exhibited by the capillary force data points between .15 mN and .35 mN (Figure 19), but is always less than its corresponding capillary force. This, along with the presence of liquid saliva and lack of other external stimuli, suggests that the adhesion is most likely caused by capillarity.

CHAPTER FIVE

CONCLUSIONS

In this work, we have successfully created an adhesion characterization method founded on the concept of Euler-Bernoulli Beam Theory and the treatment of fibers, namely the lepidopteran galeae, as beams undergoing small deflections. We developed an experimental protocol that enabled a quantitative analysis of capillary adhesion between complex-shaped fibers of living organisms that can be extended to man-made fibers. We developed a code in LabVIEW for the image analysis and contour fitting/extraction of the galeae profile for use with the mathematical model. Alongside the LabVIEW code, a data analysis code was developed in Mathematica which found solutions to the Beam Theory, imported the contour data, and fit the data with the theory.

To find the adhesion forces holding the galeae together, we have taken the third derivatives of the deflection solutions for each butterfly to determine the shear forces acting on the galeae along its entire length. Then we investigated the shear force at the crack location between the galeae ($X=0$) and at the position of contact between the galeae and the wire, point A' , to determine the vertical adhesion force V_{ady} in the beam acting to keep the galeae together and the normal force F_n at the post acting to separate them. Furthermore, we have found the capillary force acting to bring the separated galeae back together by integrating the distributed force from the crack to the meniscus location. Finally, we have found a horizontal adhesion force acting on the beam with a force balance since the angle between the neutral axis and normal vector at the point of contact between

the galea and the wire is not always $\pi/2$; thus, we have exposed the horizontal forces acting on the beam in the compression and tension states.

The measured vertical adhesion force is on the same order of magnitude as the capillary forces found through integration along the meniscus length, which indicates that the adhesion is due to capillarity and that capillary forces play a significant role in bringing the galeae together and keeping them together in the repair and assembly processes. Although the adhesion forces are feasible and the data exhibit the expected trends, it still requires a secondary experiment for validation purposes to ensure that the data are correct; however, this is a point of discussion for another work and an experimental method for carrying this out along with some preliminary results can be found in Chapter 6.

Additionally, we have extracted the Young's Modulus of Elasticity E of the lepidopteran proboscis (for Monarchs and Painted Ladies that were active, being sedated, and sleeping) from the profile of the deflected butterfly galeae by using Euler-Bernoulli beam theory to relate the shape of the galea or 'beam' with the shear and moments acting on it. The modulus was around 3.14 MPa for Monarchs and 3.15 MPa for Painted Ladies based on data from video analysis and curve fitting using our solutions to the differential equations in this theory and an estimation for I (taken from the knee region of the proboscis). These data were corroborated with the moduli found from the tensile testing of the butterfly galeae via DMA, which yielded an average modulus of 4.13 MPa between species. Although we had good agreement between the DMA and the E values found from B -fittings, we cannot confidently say the extracted moduli are correct due to our simple approximation of the galeae shape (I), the lack of knowledge about F_1 and F_2 in [5], and

the assumption that E and I are constant along the length of the beam which is inherent in this type of beam theory; however, as was mentioned previously, the proboscis shape is tapered along its length and thus, it should not have a constant I . The further study of E and I of the lepidopteran proboscis is the point of discussion for another work.

CHAPTER SIX

SIGNIFICANCE OF WORK

In this work we successfully determined the modulus of elasticity of a complex bio-fiber known as the butterfly galea by using Euler-Bernoulli beam theory to relate the shape of the fiber with the moments acting on the beam and the materials properties of the beam. Also, we have created an adhesion characterization method based on this beam theory that works by investigating the shear forces inside the beam and using force balances of the galea free-body diagram to determine the horizontal and vertical components of the adhesion force. This method, when validated with another experiment or force transducers (to directly measure the applied force on the beams and wire), could potentially be used for a wide range of composite materials such as fibers embedded onto/into matrices. Since there is a plethora of adhesion characterization methods that do not produce repeatable and easily analyzable results, we suggest there is a great need for a new adhesion experiment and that this new method based on the shape of a deflected fiber could possibly help to fill in that void. Therefore, to show that this method can be extended to other non-biological materials, we have done a preliminary investigation with well characterized, tungsten fibers.

6.1 Reference Adhesion Experiment using Ribbons of Well-Characterized Materials

6.1.1 Experimental Motivation

The goal of this reference experiment is to recreate the setup made for the butterfly proboscis, but with other, non-biological fibers instead. This will help to validate the

method and display that with a well characterized material such as tungsten, which has a modulus of elasticity of about 400 GPa, fiber deflection via capillary forces can still be realized and this deflection can be used as a measure of adhesion forces. This would also show that our model isn't limited by the rigidity of the materials being tested and that our model can extract the materials properties from more stiff materials as long as they're in the same experimental configuration. Additionally, in the future when adding a force transducer to various points on the fiber/setup, we will be able to determine the adhesion forces in the horizontal and vertical directions and relate them with what is being measured via our deflection method.

6.1.2 Experimental Protocol

To produce an experiment that is a reliable means of determining the materials parameters from these complex, biological fibers, we must have a reference fiber to validate our findings with the proboscis. We have mimicked the setup of the galeae separation experiment with ribbon-like fibers. With ribbons there are two flat sides with an edge in between that prevents droplets from moving from one flat surface to the other due to the pressure singularity at the edge. Thus, to simulate the proboscis experiment, we have used two ribbons of similar length to the proboscis (between 3 and 4 cm) and have placed them together such that one face of each is touching the other. Then we have taped both ends together with single sided scotch tape so that they stay together near the edges but can be separated in the middle. The taped ends were placed in two clothespins that were attached to a wooden block such that the fibers are straightened out (Figure 21.a).

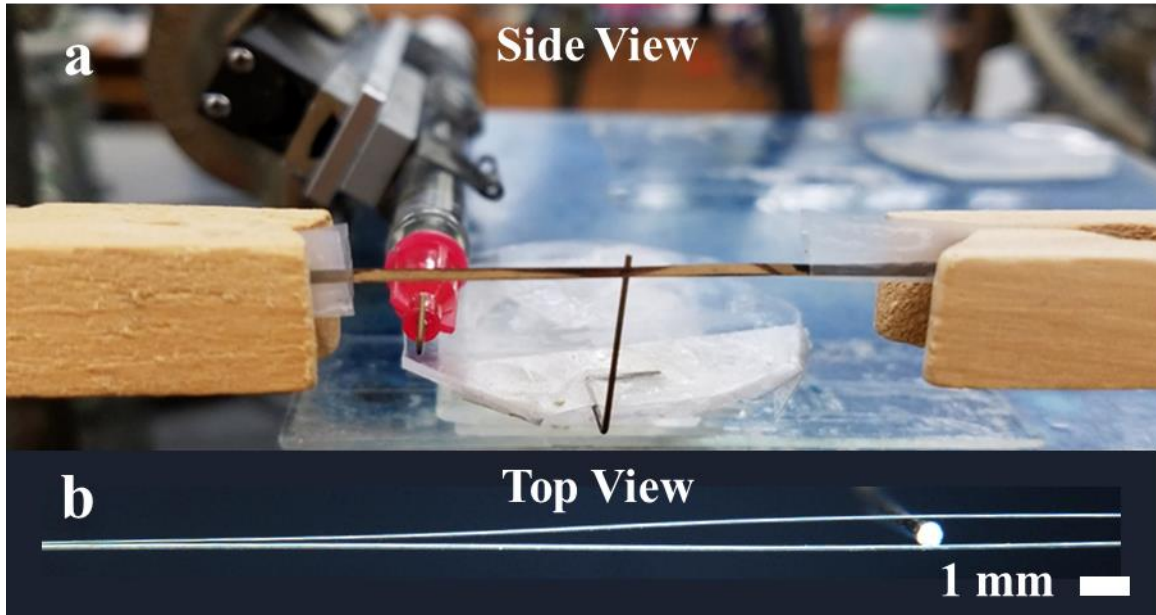


Figure 21. Experimental setup for the reference experiment. a) Side view of the experiment showing the wooden clothespins, the syringe holder, syringe, and 90° angled needle used to send water between the ribbons, the 500 μm separation tungsten wire (shown by the vertical wire in the middle), the tungsten ribbons (shown by the horizontal metallic strip), and the tape holding them together at the ends. b) Top view of the experiment showing the top edge of the ribbons which have been separated by the wire (500 μm).

Next, the fibers were separated by a tungsten wire of known diameter, which was attached to a 2-D manipulator so that different profiles could be realized (Figure 21.b). Following the separation of the ribbons, the camera was used to take a few images to be used as reference images before moving to the next step, the placement of a controlled amount of liquid between the ribbons to mimic saliva propagation. Liquid had to be used to measure the modulus of elasticity of the materials because when looking back to our differential equation for the dry region [15], the EI drops out of the equation and we are left with a polynomial solution [20].

To successfully place controlled amounts of liquid between the ribbons, we used a specialized setup including a syringe (Cadence Science, inc. 1 mL Glass Tuberculin Syringe), syringe holder with adjustable knobs to produce droplets (disassembled from

Krüss DSA10), and 90° angled needle (EFD SS Tip 15 Gauge Blue) which were combined appropriately and positioned horizontally and perpendicular to the ribbons. The tip of the needle was positioned directly below the ribbons and pointed vertically such that if a droplet was made it would be able to enter the gap between the ribbons; however, the needle tip had to be placed out of the image frame because the creation of droplets would impede image analysis in future steps. The setup can be seen in Figure 21.a. The wetting agents used were water and n-hexadecane, which is an oil based solvent that has a low surface tension and thus wets surfaces easily. Hexadecane was chosen with the aim to easily penetrate into the gap between the ribbons.

For experiments to be carried out reliably with these ribbons, we must inject the same amounts of liquid for every trial (turned the knob on the syringe holder 5 tick marks, repeated 10 times per trial/video) and the ribbons must remain symmetric with the neutral axis that extends from the crack location between ribbons through the center of the separation wire to the crack location on the opposite side. We have used tungsten ribbons (Scientific Instrument Services, Inc. Part numbers W339, W341, and W344) for the first replication trial, but the ribbons came wrapped up in a circle and, thus, the ribbons have an initial bend to them. Therefore, we had to minimize this bend by straightening it with the procedure mentioned above.

6.1.3 Surface Activation via Silanization

To show the validity of this reference experiment and test our adhesion model, we have changed the surface properties of these ribbons by treating them with three different

types of silanes (CHEM-IMPEX INT'L INC. 3-Methacryloxypropyltrimethoxysilane, SIGMA-ALDRICH CO. (3-Glycidyloxypropyl) trimethoxysilane, and TOKYO CHEMICAL INDUSTRY CO. (TCI) Trimethylethoxysilane) to change the contact angle between the liquid phase and the solid. With a change in contact angle, we expect to see a wealth of different ribbon profiles and adhesion forces between the ribbons in not only the vertical, but also longitudinal direction. The silanization procedure consists of the following.

Before any silanization could take place, it was necessary to activate the surfaces of the ribbons. To do this, we have placed the ribbons in small plastic petri dishes (about 4 per dish) at an angle so that they were resting on the lip of the dish. Next they were placed in a Plasma cleaner/sterilizer (Harrick Scientific Corp. model number) and the chamber was closed with the specified cap and the attached vacuum pump was started to reduce the pressure inside of the chamber to below 200 mTorr (working vacuum level for this instrument). Next, the plasma cleaner was turned onto the High setting for 5 minutes and afterwards, the vacuum was slowly released and the samples were taken out of the chamber.

During the 5 minutes of plasma treatment, the silane containers were prepared. This was done by placing 5 droplets of each silane being used for surface activation into separate centrifuge tubes. Next, when the plasma treatment was successfully completed, the ribbons were placed into each of the containers with silanes and the containers were closed for a week. This gave enough time for the chemical vapor deposition of the silanes onto the

surface of the ribbons to uniformly cover the ribbons. Prior to use in experiments, the ribbons were washed with methanol.

To prove that the silanes correctly bonded to the surface, contact angle measurements were performed on each of the coated ribbons with deionized water as the liquid phase. The general procedure followed for contact angle measurements is as follows. First, the Krüss Drop Shape Analyzer (DSA10) was turned on and the corresponding Drop Shape Analysis program was opened. Then a glass syringe (Cadence Science, inc. 1 mL Glass Tuberculin Syringe) was filled with deionized water and a 0.718 mm needle (Nordson EFD 22GA Blue Tips) was fitted to the end. Afterwards, a surface treated ribbon was taken out of its silane container, cleaned with methanol, and placed directly in front of and perpendicular to the camera (attached to DSA10) on the stage such that one of the flat sides was face up and the ribbon was flush with the surface.

Then, it was necessary to perform the software setup. First, one had to go into 'File', open the 'FG-Window', and click the 'Live' button (resembling a camcorder) to display the live image. Next, the drop type had to be selected by going into the menu 'Option/Subtype' and selecting the 'Normal Sessile Drop' option. After doing this, a sample droplet was created, placed on the stage directly below the needle, and then focused on so that the droplet took up most of the screen and the edges were sharp. Subsequently, the ribbon substrate of choice was repositioned directly below the needle and a droplet was formed on the needle tip by turning the knob on the syringe holder exactly 10 tick-marks clockwise (for consistency). Once the droplet was formed on the tip, the substrate was slowly raised up to the droplet via the knob on the stage until the ribbon touched the droplet.

Afterwards, the stage was lowered back to its original position, a still image was taken of the droplet by clicking the camera button, and the contact angle was measured by clicking the ‘Contact Angle – Method 2’ button (resembling a droplet on a surface). Next, the ribbon substrate was moved horizontally and perpendicular to the camera to situate a clean area on the surface below the needle tip. The procedure was repeated until 5 droplets were made on the surface. Once all droplets were completed, the ribbon was cleaned with methanol, placed back in its original container, and a new sample was positioned below the needle for testing. This was done until all of the samples were tested. A sample contact angle measurement can be seen in Figure 22 and the results for all of the silanes treated ribbons can be found in Table 6. These results show that the ribbons were successfully surface treated and that by using them with our reference experiment, we should get varying contact angles and thus, differing restoring capillary and adhesion forces.

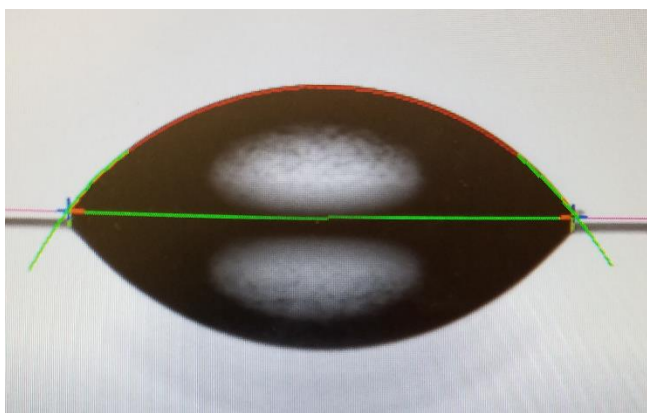


Figure 22. Typical contact angle measurement on the tungsten ribbon. This particular image was taken of a ribbon surface treated with trimethylethoxysilane and had a contact angle of 49.5° .

Table 6. Contact angle measurements on the surface of treated tungsten wires.

Surface Treatment	Average Contact Angle [°]	Standard Deviation
Untreated	58.5	9.7
3-Methacryloxypropyltrimethoxysilane	81.6	2.4
(3-Glycidyoxypropyl) trimethoxysilane	51.0	3.6
Trimethylthoxysilane	59.3	7.9

6.1.4 Future of the Project

Experimental videos with this reference experiment have been gathered with various combinations of tungsten ribbons, surface treatments, and wetting agents (mentioned in Chapters 6.1.2 and 6.1.3); however, the experimental videos have not been analyzed with our Mathematica code. This is due to a difference in the capillary forces between the flat ribbons (compared to the c-shape food canal of the galeae). The capillary force between the galeae for small distances of separation could be approximated by the linear equation seen previously [5]; however, due to the flat surfaces of the ribbons, there is a singularity in the theoretical capillary force profile (goes to infinity as the distance between the two faces come close together) and as such, we cannot approximate this force with a linear equation. Due to this non-linearity, we will have to change the model and use the Euler-Elastica (51), which is the subject of another set of work. Another suggestion could be to use non-ribbon-like fibers for future testing and as such, our model could continue to be used. In conclusion, with slight modifications to either our model or sample shape, the proposed adhesion method can be verified and used for multifunctional composites to evaluate the fiber-matrix interface along with the adhesion properties.

APPENDICES

Appendix A

Table of Collected Data

Butterfly/Video Tested	B	Lcrack	/wet	Theta [rads]	Vady [N]	Fny [N]	Fnx [N]	Vadx [N]	Fny-Vady [N]	Fc [N]	R2
M213 143514Se TG	0.20	18.38	11.02	1.49	-1.9E-04	6.74E-05	-5.17E-06	5.2E-06	-2.60E-04	-2.6E-04	0.995
Standard Deviation	0.01	2.18	1.13	0.01	5.3E-05	2.80E-05	2.57E-06	2.6E-06	2.97E-05	3.0E-05	0.007
M8 145056 A TG	0.14	29.69	22.64	1.58	-2.2E-04	1.07E-04	4.64E-07	-3.1E-07	-3.29E-04	-3.3E-04	0.996
Standard Deviation	0.02	5.32	5.47	0.01	5.3E-05	1.93E-05	1.34E-06	1.4E-06	6.36E-05	6.4E-05	0.001
M8 145056 A BG	0.07	59.02	47.76	1.55	-6.6E-04	3.15E-04	-5.77E-06	5.8E-06	-9.74E-04	-9.7E-04	0.944
Standard Deviation	0.01	7.36	7.57	0.01	1.1E-04	5.78E-05	2.03E-06	2.0E-06	1.63E-04	1.6E-04	0.036
M11 133651 A TG	0.17	18.60	11.48	1.50	-1.3E-04	7.44E-05	-4.77E-06	4.8E-06	-2.09E-04	-2.1E-04	0.996
Standard Deviation	0.03	2.09	4.44	0.02	2.8E-05	2.59E-05	2.11E-06	2.1E-06	3.73E-05	3.7E-05	0.002
M4 110162 A TG	0.14	21.04	11.90	1.51	-1.0E-04	1.14E-04	-6.77E-06	6.8E-06	-2.16E-04	-2.2E-04	0.997
Standard Deviation	0.03	2.47	6.46	0.01	4.8E-05	5.67E-05	3.65E-06	3.7E-06	6.32E-05	6.3E-05	0.002
M8 134640 A BG	0.11	33.02	12.90	1.59	-1.0E-04	1.70E-04	3.60E-06	-3.6E-06	-2.75E-04	-2.8E-04	0.998
Standard Deviation	0.01	5.42	2.35	0.01	4.6E-05	1.23E-05	1.04E-06	1.0E-06	4.49E-05	4.5E-05	0.001
M1 142413 S1 BG	0.18	23.74	10.64	1.57	-2.0E-04	7.19E-05	-1.33E-07	1.3E-07	-2.67E-04	-2.7E-04	0.995
Standard Deviation	0.00	0.44	0.24	0.00	4.2E-06	2.08E-06	4.09E-07	4.1E-07	6.12E-06	6.1E-06	0.000
M4 114756 S1 TG	0.13	27.06	13.84	1.54	-2.1E-04	1.07E-04	-3.72E-06	3.7E-06	-3.16E-04	-3.2E-04	0.990
Standard Deviation	0.00	0.37	0.19	0.00	8.6E-06	4.81E-06	3.86E-07	3.9E-07	5.69E-06	5.7E-06	0.001
M9 144505 S1 TG	0.15	23.32	13.52	1.56	-1.6E-04	1.15E-04	-1.29E-06	1.3E-06	-2.71E-04	-2.7E-04	0.998
Standard Deviation	0.01	0.35	0.20	0.01	1.3E-05	6.31E-06	7.29E-07	7.3E-07	9.00E-06	9.0E-06	0.001
PL1 104827 S1 BG	0.16	26.96	8.07	1.56	-1.5E-04	5.16E-05	-4.40E-07	4.4E-07	-2.04E-04	-2.0E-04	0.993
Standard Deviation	0.01	2.56	0.77	0.01	2.7E-05	7.02E-06	3.46E-07	3.5E-07	2.44E-05	2.4E-05	0.002
PL1 134856 S1 BG	0.14	24.13	12.35	1.57	-1.0E-04	1.44E-04	-1.27E-07	1.3E-07	-2.49E-04	-2.5E-04	0.996
Standard Deviation	0.02	2.42	1.23	0.01	4.6E-05	3.41E-05	7.56E-07	7.6E-07	2.87E-05	2.9E-05	0.001
PL5 145450 S1 TG	0.09	30.40	9.30	1.53	-9.5E-05	1.36E-04	-5.90E-06	5.9E-06	-2.31E-04	-2.3E-04	0.997
Standard Deviation	0.01	0.00	0.00	0.00	5.1E-05	4.99E-05	2.32E-06	2.3E-06	9.94E-07	9.9E-07	0.000
PL3 113156 A TG	0.15	22.34	12.59	1.54	-1.2E-04	1.02E-04	-3.10E-06	3.1E-06	-2.25E-04	-2.3E-04	0.996
Standard Deviation	0.01	2.19	4.64	0.01	3.3E-05	3.03E-05	1.36E-06	1.4E-06	3.35E-05	3.3E-05	0.001
PL3 113813 A TG	0.16	21.19	9.52	1.54	-1.2E-04	9.87E-05	-2.84E-06	2.8E-06	-2.14E-04	-2.1E-04	0.995
Standard Deviation	0.01	2.11	1.39	0.01	3.8E-05	2.00E-05	9.60E-07	9.6E-07	2.93E-05	2.9E-05	0.001
PL3 114723 A TG	0.17	21.81	8.25	1.54	-1.4E-04	6.31E-05	-1.78E-06	1.8E-06	1.99E-04	-2.0E-04	0.999
Standard Deviation	0.01	2.16	1.86	0.01	3.6E-05	2.05E-05	1.11E-06	1.1E-06	3.83E-05	3.8E-05	0.000
PL6 154513 A TG	0.19	19.80	7.27	1.53	-1.1E-04	6.09E-05	-2.69E-06	2.7E-06	1.72E-04	-1.7E-04	0.998
Standard Deviation	0.03	1.79	2.27	0.01	3.9E-05	4.30E-05	2.18E-06	2.2E-06	3.99E-05	4.0E-05	0.001
PL6 155022 A TG	0.18	20.66	9.05	1.54	-1.3E-04	7.16E-05	-1.92E-06	1.9E-06	2.06E-04	-2.1E-04	0.998
Standard Deviation	0.02	1.44	2.25	0.01	2.3E-05	2.32E-05	8.01E-07	8.0E-07	3.38E-05	3.4E-05	0.001
PL1 134856 A TG	0.16	13.53	7.74	1.44	-9.2E-05	7.68E-05	-9.94E-06	9.9E-06	1.69E-04	-1.7E-04	0.999
Standard Deviation	0.02	1.09	0.69	0.01	3.5E-05	2.58E-05	3.46E-06	3.5E-06	1.50E-05	8.5E-05	0.000
PL4 132734 Se TG	0.14	20.04	11.57	1.51	-1.2E-04	1.18E-04	-7.43E-06	7.4E-06	2.35E-04	-2.4E-04	0.999
Standard Deviation	0.02	2.23	3.01	0.01	5.0E-05	3.88E-05	2.37E-06	2.4E-06	4.17E-05	4.2E-05	0.001
PL5 145450 Se BG	0.15	20.74	9.97	1.53	-9.3E-05	1.22E-04	-5.59E-06	5.6E-06	2.15E-04	-2.1E-04	0.996
Standard Deviation	0.03	3.89	3.38	0.01	6.2E-05	5.13E-05	2.70E-06	2.7E-06	6.88E-05	6.9E-05	0.002
Overall Averages	0.1520	22.970	11.242	1.535	-1.36E-04	9.86E-05	-3.13E-06	3.14E-06	-1.09E-04	-2.35E-04	0.996
Overall Standard Devs	0.0161	2.131	2.209	0.008	3.66E-05	2.63E-05	1.61E-06	1.61E-06	3.23E-05	3.60E-05	0.001
Monarch Average	0.1519	24.354	13.492	1.542	-1.65E-04	1.03E-04	-2.22E-06	2.24E-06	-2.68E-04	-2.68E-04	0.996
Standard Deviation	0.0148	2.329	2.560	0.009	3.18E-05	1.94E-05	1.53E-06	1.54E-06	3.24E-05	3.24E-05	0.002
Painted lady Average	0.1520	21.96	9.61	1.53	-1.16E-04	9.51E-05	-3.80E-06	3.80E-06	6.59E-06	-2.11E-04	0.996818
Standard Deviation	0.0171	1.99	1.95	0.01	4.00E-05	3.13E-05	1.67E-06	1.67E-06	3.22E-05	3.86E-05	0.000915

Appendix B

Glossary of Parameters

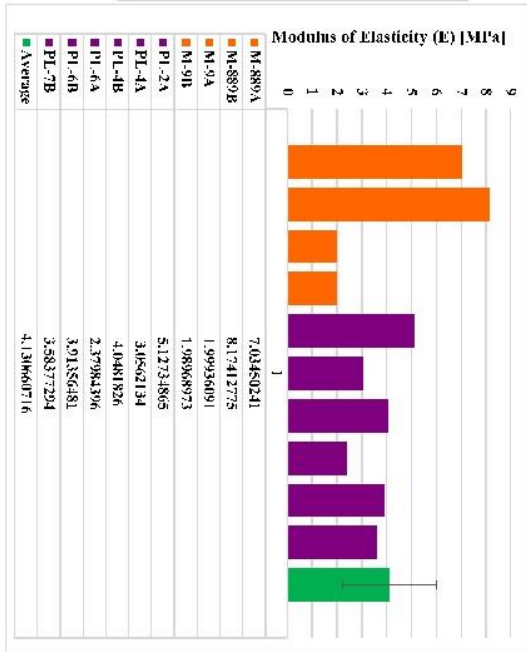
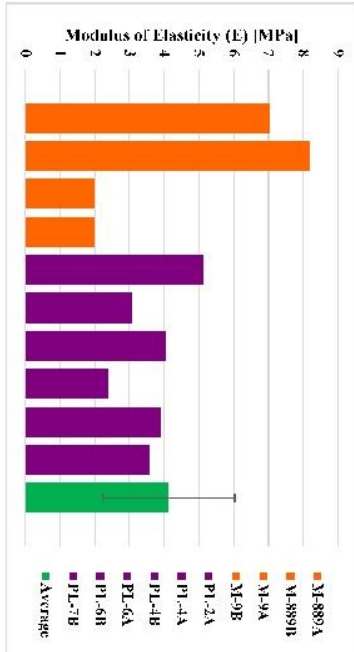
<i>A (state of butterfly)</i>	Active - butterfly is moving its head and pumping saliva between its galeae
<i>A (position)</i>	Position where galea/fiber touches the post
<i>B</i>	Normalized fitting parameter including F_2 , R , E , and I
<i>D</i>	Flexural Rigidity
<i>E</i>	Modulus of Elasticity (Young's Modulus)
<i>F₁</i>	Force per unit length accounting for pressure and surface tension in the saliva column
<i>F₂</i>	Force per unit area accounting for pressure and surface tension in the saliva column
<i>F_c</i>	Total capillary force acting on the beam/ galea
<i>F_{nx}</i>	X component of normal force created at point A
<i>F_{ny}</i>	y component of normal force created at point A
<i>h</i>	Galea wall thickness
<i>I</i>	Area moment of inertia
<i>L</i>	Crack length normalized by R
<i>l</i>	Length of wet region normalized by R
<i>l_{airgap}</i>	Length of air gap between saliva meniscus and post
<i>L_{crack}</i>	Crack length between $x=0$ and A'
<i>L_R</i>	Retraction length of the saliva
<i>l_{wet}</i>	Length of the wet region from $x=0$ to meniscus location
<i>M</i>	Monarch
<i>m</i>	Distributed moment along the beam accounting for muscular forces (considered constant)
<i>M(x)</i>	Internal moment
<i>p(x)</i>	Force density acting on beam
<i>PL</i>	Painted Lady
<i>R</i>	Radius of the separation wire-post
<i>r_{fc}</i>	Radius of the food canal in proboscis
<i>Se (state of butterfly)</i>	Sedated - Butterfly is undergoing sedation

<i>Sl</i> (<i>state of butterfly</i>)	Sleeping - Butterfly is completely anaesthetized
<i>t</i>	Time
<i>V(x)</i>	Internal shear force
<i>V_{adx}</i>	Horizontal Adhesion Force - x component of adhesion force (tangential)
<i>V_{ady}</i>	Vertical Adhesion Force - y component of adhesion force (normal)
<i>X</i>	Horizontal position normalized by radius of the post
<i>x</i>	Horizontal position along the galeae
<i>Y(X)</i>	Deflection normalized by radius of the post
<i>y(x)</i>	Deflection of the galea from the x-axis
<i>y_{cr}</i>	Measured deflection of the galea at the meniscus position
<i>γ</i>	Dimensionless parameter relating F1, F2, and R
<i>θ</i>	Angle between x-axis & inwards normal vector of the tangent line positioned at intersection of galea and post

Appendix C

DMA Data

Sample	Young's Modulus (N/m ²)	Young's Modulus (MPa)	Cross Sectional Area (m ²)	Epoxy Type	Comment
PL-2A	5127348.65	5.12734865	6.87814E-09	steel	
PL-4A	3056213.4	3.0562134	5.76189E-09	steel	Tested sample 5 days after death
PL-4B	4048182.6	4.0481826	5.76189E-09	steel	
PL-6A	2379843.96	2.37984396	6.852E-09	plastic	
PL-6B	3913564.81	3.91356481	5.43407E-09	plastic	
PL-7B	3583772.94	3.58377294	7.16821E-09	plastic	
M-889A	7034502.41	7.03450241	3.77718E-09		
M-889B	8174127.75	8.17412775	2.42651E-09		
M-9A	1999360.91	1.99936091	1.67599E-08		
M-9B	1989589.73	1.98958973	1.35708E-08		
Average		4.130660716	7.43906E-09		
St. dev		1.894353345	3.97022E-09		
upper		6.025014061			
lower		2.236307371			



Appendix D

Wolfram Mathematica® Code

Deflection Model - Euler Bernoulli Beam solution

Starting the code, inputting boundary conditions, solving equations, and getting forces due to pressure.

Background Code - finding solutions to our differential equations

```
in[1]= (*equations describing the saliva region from X=0 to lwet*)
(*normalized equations by R, and D=E*I, the bending moment of the beam*)
Y1[X_, γ_, B_, A1_, A2_, A3_, A4_] =
  (γ) + A1 * Cos[B * X] + A3 * Cosh[B * X] + A2 * Sin[B * X] + A4 * Sinh[B * X];
D1Y1[X_, γ_, B_, A1_, A2_, A3_, A4_] = D[Y1[X, γ, B, A1, A2, A3, A4], {X, 1}];
(*inserting the two boundary conditions for this case at X=0*)
BCsetY1[γ_, B_, A1_, A2_] =
  Solve[{Y1[0, γ, B, A1, A2, A3, A4] == 0, D1Y1[0, γ, B, A1, A2, A3, A4] == 0}, {A3, A4}];
A3new[γ_, B_, A1_, A2_] = A3 /. BCsetY1[γ, B, A1, A2][[1]];
A4new[γ_, B_, A1_, A2_] = A4 /. BCsetY1[γ, B, A1, A2][[1]];
(*inputting Anew's into Y1 to get rid of 2 integration constants*)
Y1new[X_, γ_, B_, A1_, A2_] = Y1[X, γ, B, A1, A2, A3new[γ, B, A1, A2], A4new[γ, B, A1, A2]];
(*now for the equations describing the air gap region from X=lwet to Lcrack*)
Y2[X_, C1_, C2_, C3_, C4_] = C1 * X^3 + C2 * X^2 + C3 * X + C4;
D1Y2[X_, C1_, C2_, C3_, C4_] = D[Y2[X, C1, C2, C3, C4], {X, 1}];
(*using 2 boundary conditions for this case at the post X=L*)
BCsetY2[L_, C1_, C2_, θ_] =
  Solve[{Y2[L, C1, C2, C3, C4] == Sin[θ], D1Y2[L, C1, C2, C3, C4] == Cot[θ]}, {C4, C3}];
C3new[L_, C1_, C2_, θ_] = C3 /. BCsetY2[L, C1, C2, θ][[1]];
C4new[L_, C1_, C2_, θ_] = C4 /. BCsetY2[L, C1, C2, θ][[1]];
(*inputting Cnew's into Y2 to get rid of 2 integration constants*)
Y2new[X_, C1_, C2_, L_, θ_] =
  Simplify[Y2[X, C1, C2, C3new[L, C1, C2, θ], C4new[L, C1, C2, θ]]];
(*Introducing Boundary Conditions to solve for remaining integration constants*)
CCset[γ_, B_, L_, l_, θ_] = Solve[{Y1new[l, γ, B, A1, A2] == Y2new[l, C1, C2, L, θ],
  {D[Y1new[X, γ, B, A1, A2], {X, 1}] /. X -> l ==
    {D[Y2new[X, C1, C2, L, θ], {X, 1}] /. X -> l},
  {D[Y1new[X, γ, B, A1, A2], {X, 2}] /. X -> l ==
    {D[Y2new[X, C1, C2, L, θ], {X, 2}] /. X -> l},
  {D[Y1new[X, γ, B, A1, A2], {X, 3}] /. X -> l ==
    {D[Y2new[X, C1, C2, L, θ], {X, 3}] /. X -> l}}, {A1, A2, C1, C2}];
```

```

(*establishing new expressions for the integration constants*)
A1new[γ_, B_, L_, l_, θ_] = A1 /. CCset[γ, B, L, l, θ][[1]];
A2new[γ_, B_, L_, l_, θ_] = A2 /. CCset[γ, B, L, l, θ][[1]];
C1new[γ_, B_, L_, l_, θ_] = C1 /. CCset[γ, B, L, l, θ][[1]];
C2new[γ_, B_, L_, l_, θ_] = C2 /. CCset[γ, B, L, l, θ][[1]];
(*plugging new integration constants back into original equation*)
Y1F[X_, γ_, B_, L_, l_, θ_] = Y1new[X, γ, B, A1new[γ, B, L, l, θ], A2new[γ, B, L, l, θ]];
Y2F[X_, γ_, B_, L_, l_, θ_] = Y2new[X, C1new[γ, B, L, l, θ], C2new[γ, B, L, l, θ], L, θ];
D2Y1F[X_, γ_, B_, L_, l_, θ_] = D[Y1F[X, γ, B, L, l, θ], {X, 2}];
D3Y1F[X_, γ_, B_, L_, l_, θ_] = D[Y1F[X, γ, B, L, l, θ], {X, 3}];
(*creating a piecewise function to account
for the two equations required in the step above*)
Ytot[X_, γ_, B_, L_, l_, θ_] =
Piecewise[{{Y1F[X, γ, B, L, l, θ], 0 ≤ X ≤ l}, {Y2F[X, γ, B, L, l, θ], l ≤ X ≤ L}}];
D1Ytot[X_, γ_, B_, L_, l_, θ_] = D[Ytot[X, γ, B, L, l, θ], {X, 1}];
D2Ytot[X_, γ_, B_, L_, l_, θ_] = D[Ytot[X, γ, B, L, l, θ], {X, 2}];
D3Ytot[X_, γ_, B_, L_, l_, θ_] = D[Ytot[X, γ, B, L, l, θ], {X, 3}];
D4Ytot[X_, γ_, B_, L_, l_, θ_] = D[Ytot[X, γ, B, L, l, θ], {X, 4}];

(*calculations from Chengqi for total force in the saliva column*)
(*normalized force by 2 times the surface tension
of water and the distance by the radius of the food canal*)
a2[alpha_] := 2 * alpha + Sin[2 * alpha];
b2[alpha_, theta_] := 4 * Sin[alpha] - 2 * Pi * Cos[theta];
c2 = Pi;
d2[alpha_, theta_] := b2[alpha, theta]^2 - 4 * a2[alpha] * c2;
s2[alpha_, theta_] :=
(-Sqrt[d2[alpha, theta]] - b2[alpha, theta]) / (2 * a2[alpha]) * Sin[alpha];
f2[alpha_, theta_] := Cos[alpha] + Sin[alpha] / s2[alpha, theta];
data = Table[{s2[n, 0], f2[n, 0]}, {n, 0.01, Pi/2, Pi/1000}];
data2 = Cases[data, {x_, y_} /; x <= 0.5];
ListPlot[data];
ListPlot[data2];
f11 = b /. FindFit[data2, a * x + b, {a, b}, x];
f22 = a /. FindFit[data2, a * x + b, {a, b}, x];
normforce =
Show[ListPlot[data2], Plot[-2.64467 X + 2.92596, {X, 0, .5}, PlotStyle -> {Red, Bold},
PlotLegends -> Placed[{ $\frac{f}{2\sigma} = -2.64467 \frac{Y}{r_{fc}} + 2.92596$ }, {Top, Center}],
LabelStyle -> Directive[Bold, 18], ImageSize -> Large, AxesLabel ->
{HoldForm[" $\frac{Y}{r_{fc}}$ "], HoldForm[" $\frac{f}{2\sigma}$ "]}, LabelStyle -> Directive[Bold, 18, Black]];
(*redimensionalizing everything so that we can easily correlate the parameters,
72.86 mN/m used for surface tension of water at room
temperature and 35*10^-6m used for rfc from Dasha's paper*)
dataredim = data2 * (2 * 72.86 * 10^-3);
ListPlot[dataredim];
dataredimx = Transpose[dataredim][[1]] * ((35 * 10^-6) / (2 * 72.86 * 10^-3));
dataredimy = Transpose[dataredim][[2]];
Mat1 = Transpose[{dataredimx, dataredimy}];

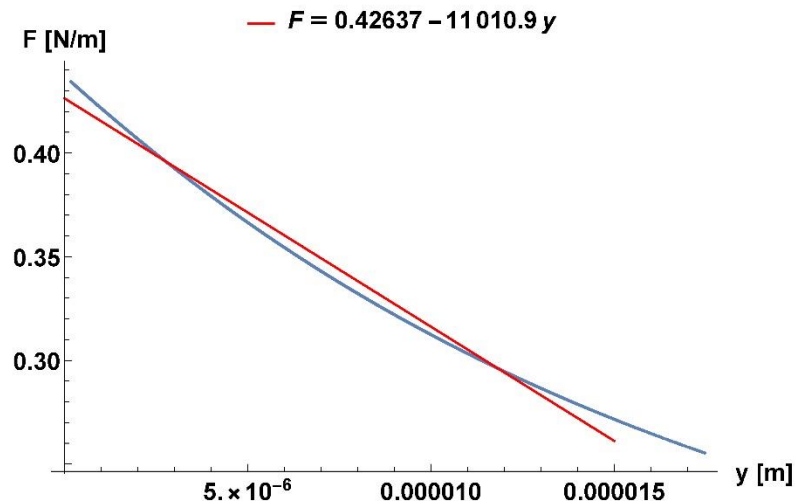
```

```

F11 = f111 /. FindFit[Mat1, f222 * x + f111, {f111, f222}, x]
F22 = f222 /. FindFit[Mat1, f222 * x + f111, {f111, f222}, x]

Show[ListPlot[Mat1], Plot[F22 * X + F11, {X, 0, .000015},
  PlotStyle -> {Red, Bold}, PlotLegends -> Placed[{F == F22 * y + F11}, {Top, Center}],
  LabelStyle -> Directive[Bold, 18]], ImageSize -> Large,
  AxesLabel -> {HoldForm["y [m]"], HoldForm["F [N/m]"]},
  LabelStyle -> Directive[Bold, 18, Black]]
(*using gamma in place of eta/beta*)
γ0[F1_, F2_, R_] = (F1) / ((F2) * R);
(*calculations for F1 and F2 done with contact angle of zero*)
(*R is changing from 50 um to 75 um, on average we used 62.5 um*)
R1 = 50 * 10-6;
R2 = 62.5 * 10-6;
R3 = 75 * 10-6;
γ1 = γ0[F11, Abs[F22], R1]
γ2 = γ0[F11, Abs[F22], R2]
γ3 = γ0[F11, Abs[F22], R3];
L1 = 20;
θ1 = (Pi / 2);
0.42637
-11010.9

```



0.774453

0.619563

```

Iygalea[Rfc1_, Rout1_, h1_] :=
  
$$\frac{1}{8} \pi \left( - (h1 - Rfc1)^4 + Rfc1^4 - (h1 - Rfc1) (h1 - Rout1)^3 + Rfc1 * Rout1^3 \right);$$

Iygalea[Rfc1_, Rout1_, h1_] :=
  
$$\frac{1}{8} \pi \left( - (h1 - Rfc1)^4 + Rfc1^4 - (h1 - Rfc1)^3 (h1 - Rout1) + Rfc1^3 * Rout1 \right);$$

N[Iygalea[35 * 10^-6, 100 * 10^-6, 20 * 10^-6]];
N[Iygalea[35 * 10^-6, 100 * 10^-6, 20 * 10^-6]];
(*Manipulate[N[Iygalea[Rfc1,Rout1,h1]],{Rfc1,35*10^-6,55*10^-6},
  {Rout1,100*10^-6,300*10^-6},{h1,20*10^-6,30*10^-6}];*)

moel = (11010.9 * (62.5 * 10^-6)^4) / ((.1466^4) * (1.13 * 10^-17));
moel2 = (11010.9 * (62.5 * 10^-6)^4) / ((.1466^4) * (1.00 * 10^-16));

(*for the reference experiments*)
Rpostref = 250 * 10^-6;
γref = γ0[F11, Abs[F22], Rpostref];
γrefhex = γ0[F11hex, Abs[F22hex], Rpostref];

IW339 = N[(.76 * 10^-3 * (.01 * 10^-3)^3) / 12] (*m^4*);
IW341 = N[(.25 * 10^-3 * (.025 * 10^-3)^3) / 12];
IW119 = N[(1.500 * 10^-3 * (.2 * 10^-3)^3) / 12];
IW344 = N[(1.270 * 10^-3 * (.050 * 10^-3)^3) / 12];
Btungeestimate[Iest_, Etung_, R_] := (Abs[F22] * R^4 / ((Etung) * (Iest)))^(1/4);
BW339 = Btungeestimate[IW339, 400 * 10^9, Rpostref];
BW341 = Btungeestimate[IW341, 400 * 10^9, Rpostref];
BW119 = Btungeestimate[IW119, 400 * 10^9, Rpostref];
BW344 = Btungeestimate[IW344, 400 * 10^9, Rpostref];

(*using HEXADECANE with surface tension of 27.47*10^-3 N/m from http://
  www.surface-tension.de/ *)
dataredimhex = data2 * (2 * 27.47 * 10^-3);
ListPlot[dataredimhex];
dataredimhexx = Transpose[dataredimhex][[1]] * ((35 * 10^-6)) / (2 * 27.47 * 10^-3);
dataredimhexy = Transpose[dataredimhex][[2]];
Mathex1 = Transpose[{dataredimhexx, dataredimhexy}];
F11hex = f111 /. FindFit[Mathex1, f222 * x + f111, {f111, f222}, x];
F22hex = f222 /. FindFit[Mathex1, f222 * x + f111, {f111, f222}, x];

```


Fitting experimental data with theoretical solutions - Solving for B

```

(*Changing Bi value ranges for different L's
  L<20 use a Bi of 2.0*10^-1
  20<L<35 use a Bini of 1*10^-1
  L>35 use a Bi of .8*10^-1*)
(*Check with this plot if need be, just uncomment*)
(*Manipulate[
  Plot[{Ytot[X,γ2,Bi,15,1,01]}, {X,0,15}, AxesLabel→{HoldForm["X"], HoldForm["Y"]},
  PlotStyle→Thickness[.01], LabelStyle→Directive[Bold, 20, Black],
  PlotLabel→B=ScientificForm[Bi]], {Bi, 1*10^-1, 3.0*10^-1}, {1,0,15}]*

(*STARTING WITH EXPERIMENTAL DATA RIGHT HERE*)
(*Importing Experimental*)
data1 = Import["Y:\\Luke Sande\\Butterfly Proboscis
  Project\\Summer 2017\\Butterfly videos\\7-5-17\\PL5 sedating
  145450\\BG_FrameNum_640_PostR_26_AirGap_11.39_Theta_1.526_Rot_0.38_GT_0.57
  _SlopePts_75.csv"];
data1T = Transpose[data1];
lair1 = 11.39;
θexp = 1.526;
l1new[L_] := L - lair1;
Lini1 = Max[data1] (*taking initial L to be the largest X value that shows up*)
ListPlot[data1];
(*Gt=0.36; (*done in labview but it is calculated as (GT/(GT+P0st radius))**)
Ycrposition[L_] := Nearest[data1T[[1]], l1new[L]][[1]];
Ycrposition[Lini1];
Ycr1 = Module[{n = 1}, While[data1[[n]][[1]] < Ycrposition[Lini1], n++];
  data1[[n]][[2]]];
Bini1 = Bi /. FindFit[data1, {Ytot[X, γ2, Bi, Lini1, l1new[Lini1], θexp]},
  {Bi, .15}, X, Gradient → "FiniteDifference"]
Dini1 = (Abs[F22] * R2^4) / ((Bini1))^4 (*R2 is the radius of
  the post that we're using in this case*)
(*added part for the pressure and surface tension of
  the saliva into our adhesion calculation below*)
Show[Plot[Ytot[X, γ2, Bini1, Lini1, l1new[Lini1], θexp], {X, 0, Lini1},
  PlotStyle → {{Red, Thickness[.008]}}, AxesLabel → {HoldForm["X"], HoldForm["Y"]},
  PlotLegends → Placed[{B == Bini1}, {Top, Center}],
  LabelStyle → Directive[Bold, 20, Black]],
ListPlot[data1, PlotRange → All, PlotStyle → {Green, PointSize[.007]}], ImageSize → Large]
(*FORCES → all forces come out in units of N *)
(*Sign convention, positive is up or right,
  depending on if it is vertical or horizontal respectively*)
Vady = -Dini1 * D3Ytot[0, γ2, Bini1, Lini1, l1new[Lini1], θexp] * (1/R2^(2))
Fny = -Dini1 * D3Ytot[Lini1, γ2, Bini1, Lini1, l1new[Lini1], θexp] * (1/R2^(2))
Fc = Integrate[-F11 + Abs[F22] * R2 * Ytot[X, γ2, Bini1, Lini1, l1new[Lini1], θexp],
  {X, 0, l1new[Lini1]}] * R2;
Fnx = (-Fny) * Tan[(Pi/2) - θexp]
Vadx = -Fnx
Fcequal = Dini1 * D3Ytot[Lini1, γ2, Bini1, Lini1, l1new[Lini1], θexp] * (1/R2^(2)) -

```

```

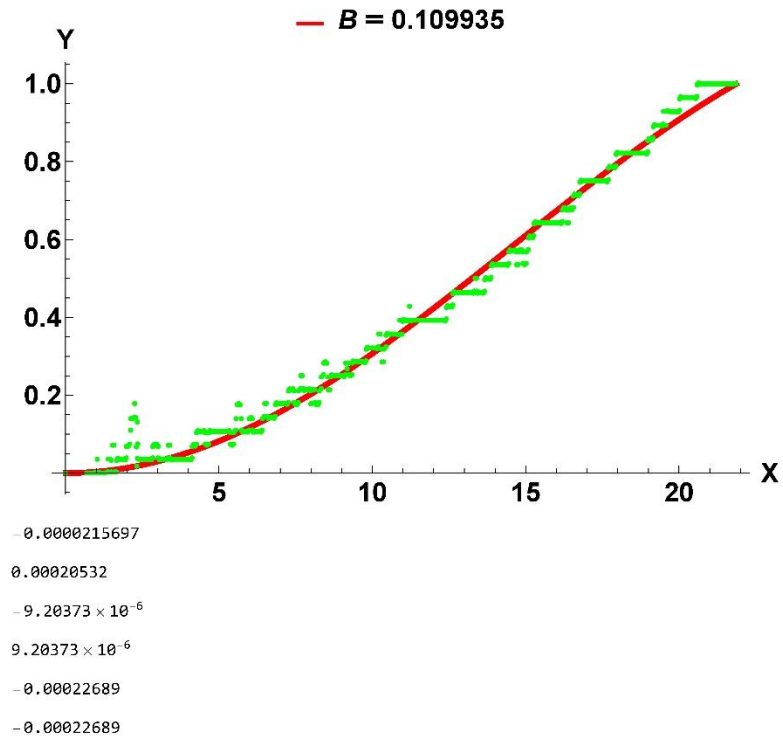
Dini1 * D3Ytot[0, γ2, Bini1, Lini1, lnew[Lini1], θexp] * (1/R2^(2))
Fc
(*Checking Fc with the other integration,
by integrating the fourth derivative instead of the actual force on the other side*)
Fcnew = -Integrate[Dini1 *
    D4Ytot[X, γ2, Bini1, Lini1, lnew[Lini1], θexp] * (1/R2^(3)), {X, 0, Lini1}] * R2;

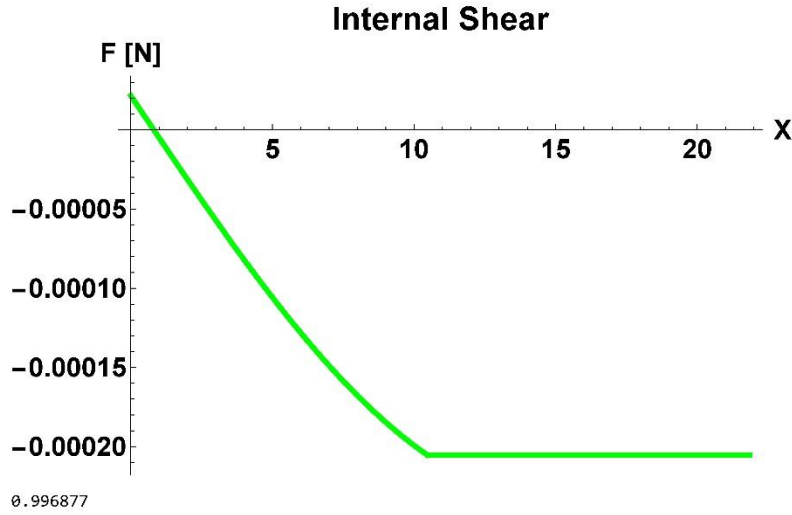
Plot[(Dini1/R2) * D2Ytot[X, γ2, Bini1, Lini1, lnew[Lini1], θexp], {X, 0, Lini1},
    PlotStyle → {{Blue, Thickness[.008]}}, AxesLabel → {HoldForm["X"], HoldForm["M [Nm]"]},
    LabelStyle → Directive[Bold, 20, Black], PlotLabel → "Internal Moment"];
Plot[(Dini1/R2^2) * D3Ytot[X, γ2, Bini1, Lini1, lnew[Lini1], θexp], {X, 0, Lini1},
    PlotStyle → {{Green, Thickness[.008]}}, AxesLabel → {HoldForm["X"], HoldForm["F [N]"]},
    LabelStyle → Directive[Bold, 20, Black], PlotLabel → "Internal Shear"]

(*adding the nonlinear model fit in order to find the RSquared values*)
nlm1 =
    NonlinearModelFit[data1, Ytot[X, γ2, Bi, Lini1, lnew[Lini1], θexp], {{Bi, .15}}, X];
nlm1["RSquared"]
(*bands95[X_] = nlm1["MeanPredictionBands", ConfidenceLevel → .95];*)
(*Show[Plot[{nlm1[X], bands95[X]}, {X, 0, Lini1}, Filling → {2 → {1}},
    PlotStyle → {{Red, Thickness[.005]}}, AxesLabel → {HoldForm["X"], HoldForm["Y"]},
    PlotLegends → Placed[{B == Bini1}, {Top, Center}], LabelStyle → Directive[Bold, 20, Black]},
    ListPlot[data1, PlotRange → All, PlotStyle → {Green, PointSize[.007]}], ImageSize → Large]*)

21.8571
0.109935
1.15025 × 10-9

```





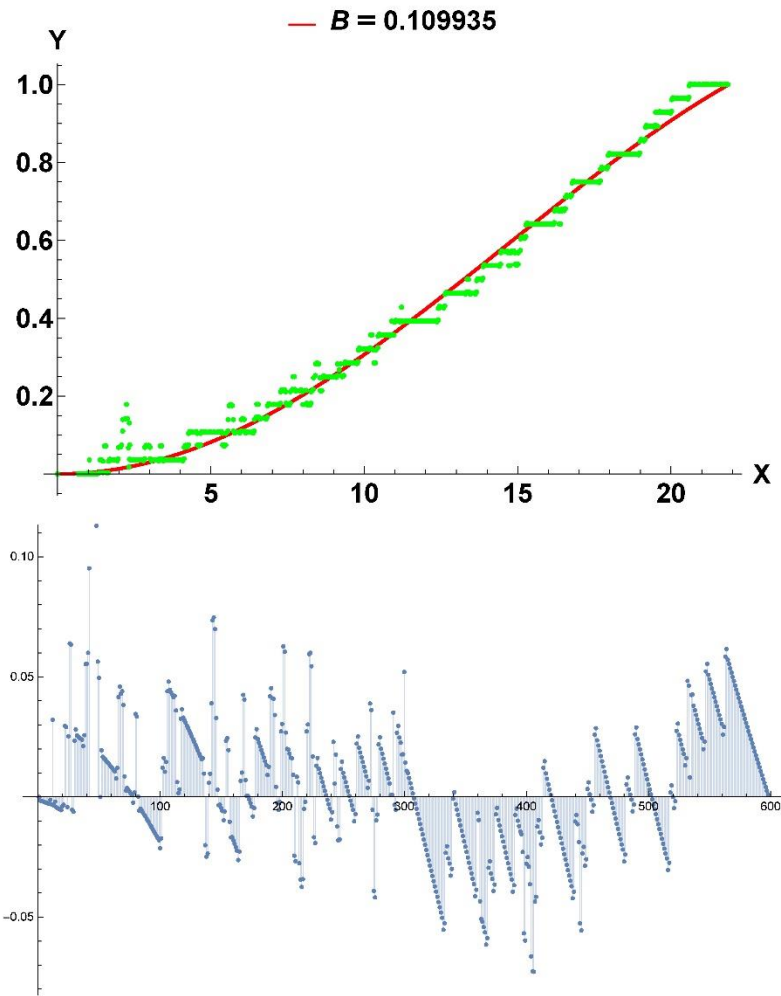
Nonlinear data fitting for comparison purposes

```
(*DATA fitting with Nonlinear model fit and finding RSquared where nlm1 is
our nonlinear model fit, Normal gives the functional form of this fit*)
(*A confidence level of 95/100 is used for parameters and predictions*)
nlm1 = NonlinearModelFit[data1,
  Ytot[X, γ2, Bi, Lini1, l1new[Lini1], θexp], {{Bi, .9 * 10^-1}}, X];
Simplify[Normal[nlm1]] [[1]]
nlm1["ParameterTable"]
nlm1["RSquared"]
bands95[X_] = nlm1["MeanPredictionBands", ConfidenceLevel → .95]; (*Confidence bands*)
Show[Plot[{nlm1[X]}, {X, 0, Lini1}, Filling → {2 → {1}},
  PlotStyle → {{Red, Thickness[.005]}}, AxesLabel → {HoldForm["X"], HoldForm["Y"]},
  PlotLegends → Placed[{B == Bini1}, {Top, Center}],
  LabelStyle → Directive[Bold, 20, Black]],
  ListPlot[data1, PlotRange → All, PlotStyle → {Green, PointSize[.007]}], ImageSize → Large]
nlm1["FitResiduals"];
ListPlot[nlm1["FitResiduals"], Filling → Axis]
nlm1["ANOVATable"]
```

```
{ {0.028616 - 0.0115515 X + 0.00509976 X^2 - 0.000116211 X^3, 10.4671 < X ≤ 21.8571},
  {0.619563 - 0.583683 Cos[0.109935 X] - 0.0358794 Cosh[0.109935 X] -
    0.0275658 Sin[0.109935 X] + 0.0275658 Sinh[0.109935 X], 0 ≤ X ≤ 10.4671} }
```

	Estimate	Standard Error	t-Statistic	P-Value
Bi	0.109935	0.00282254	38.9492	4.65191 × 10 ⁻¹⁶⁶

0.996877



	DF	SS	MS
Model	1	167.799	167.799
Error	597	0.525641	0.000880471
Uncorrected Total	598	168.325	
Corrected Total	597	60.6618	

Looping through different L values to find optimal B and L pair

```
(*here is the loop*)
(*Changing the Bj initial value from Bj to 3.2*10^-3 which is in the center of
the range where we can see visual influence of the B value on deflection*)
Lloop1[γ_, θ_, Ycr_] :=
Module[{Lii = Lini1, Bjj = Bini1},

While[Abs[Ytot[l1new[Lii], γ, Bjj, Lii, l1new[Lii], θ] - Ycr] ≥ .1,
Print[{Lii, Bjj, Abs[Ytot[l1new[Lii], γ, Bjj, Lii, l1new[Lii], θ] - Ycr]}];
Bjj = Bii /. FindFit[data1, Ytot[l1new[Lii], γ, Bjj, Lii, l1new[Lii], θ],
{Bii, Bjj}}, X, Gradient → "FiniteDifference"];
Lii += .05];

Print[{"Final B"}];
Print[{Lii, Bjj, Abs[Ytot[l1new[Lii], γ, Bjj, Lii, l1new[Lii], θ] - Ycr]}];
(*Check adhesion calculations!!*)
(*(((Bjj)^4)/(β))^(−1))*D2Y1F[0,η,β,Bjj,Lii,l1new[Lii],θ]/4*)
Show[Plot[Ytot[X, γ, Bjj, Lii, l1new[Lii], θ], {X, 0, Lii},
PlotStyle → {Red, Thickness[.007]}, AxesLabel → {HoldForm["X"], HoldForm["Y"]},
PlotLegends → Placed[{B == ScientificForm[Bjj]}, {Top, Center}],
LabelStyle → Directive[Bold, 20, Black]],
ListPlot[{data1, MovingAverage[data1 + {Gt/2}, 80], MovingAverage[data1 - {Gt/2}, 80]},
PlotRange → All, PlotStyle → {{Blue, PointSize[.007]},
{Orange, PointSize[.002]}, {Orange, PointSize[.002]}}, Filling → {2 -> {3}},
FillingStyle → Directive[Opacity[0.15], Purple]}, ImageSize → Large]]

(*running the loop now with defined eta2, beta 2, theta 1, and ycrexp*)
Lloop1[γ2, θ1, Ycr1]
{Final B}
```

Proving our solution to the equation is correct!

```
(*Proving our solution is correct*)
Y1diffeqn[X_] = Y[X] /. DSolve[{Dini/R^3}*Y''''[X] == -F1 + F2*R*Y[X], Y[X], X][[1]];
sub1 = {F1 → γ*R*F2};
sub2 = {R*F2^(1/4) → B*Dini^(1/4)};
Y1diffeqn2[X_] = Simplify[ExpToTrig[Y1diffeqn[X] /. sub1 /. sub2]]
intconstantsub = {C[1] → A1, {C[2] + C[4]} → A2, C[3] → A3, {-C[2] + C[4]} → A4};
Y1f[X_] = Y1diffeqn2[X] /. intconstantsub
γ + C[1] Cos[B X] + {C[2] + C[4]} Cosh[B X] + C[3] Sin[B X] + {-C[2] + C[4]} Sinh[B X]
γ + A1 Cos[B X] + A2 Cosh[B X] + A3 Sin[B X] + A4 Sinh[B X]
```

Plots

Appendix E

Integration Constants for Solutions to Differential Equations

$$\begin{aligned} N_{11} = & 12B\gamma + B^5l^4\gamma - 4B^5l^3L\gamma + 6B^5l^2L^2\gamma - 4B^5lL^3\gamma + B^5L^4\gamma - 12B\gamma\cos[Bl] + \\ & 6B^3l^2\gamma\cos[Bl] - 12B^3lL\gamma\cos[Bl] + 6B^3L^2\gamma\cos[Bl] + 12Bl\cos[Bl]\cot[\theta] - \\ & 2B^3l^3\cos[Bl]\cot[\theta] - 12BL\cos[Bl]\cot[\theta] + 6B^3l^2L\cos[Bl]\cot[\theta] - \\ & 6B^3lL^2\cos[Bl]\cot[\theta] + 2B^3L^3\cos[Bl]\cot[\theta] - 12B^2l\gamma\sin[Bl] + 12B^2L\gamma\sin[Bl] - \\ & 12\cot[\theta]\sin[Bl] + 6B^2l^2\cot[\theta]\sin[Bl] - 12B^2lL\cot[\theta]\sin[Bl] + \\ & 6B^2L^2\cot[\theta]\sin[Bl] + 12B\cos[Bl]\sin[\theta] - 6B^3l^2\cos[Bl]\sin[\theta] + \\ & 12B^3lL\cos[Bl]\sin[\theta] - 6B^3L^2\cos[Bl]\sin[\theta] + 12B^2l\sin[Bl]\sin[\theta] - \\ & 12B^2L\sin[Bl]\sin[\theta] + B\cosh[Bl]((-12 - 12B^2(l-L)^2 + B^4(l-L)^4)\gamma\cos[Bl] - \\ & 2((6 + B^2(l-L)^2)(l-L)\cot[\theta] + 4B^3(l-L)^3\gamma\sin[Bl] + 3(2 + B^2(l-L)^2)(-\gamma + \\ & \sin[\theta]))) + (24B^2(l-L)\gamma\cos[Bl] + 6(2 + B^2(l-L)^2)\cot[\theta] + B((-12 + \\ & 12B^2(l-L)^2 + B^4(l-L)^4)\gamma\sin[Bl] + 12B(l-L)(-\gamma + \sin[\theta])))\sinh[Bl] \end{aligned}$$

$$\begin{aligned} N_{21} = & 6(2B^2(l-L)\gamma\cos[Bl] + 2\cot[\theta] + B(-2 + B^2(l-L)^2)\gamma\sin[Bl]) \\ & (-6(2(\cos[Bl] - \cosh[Bl]) + B^2(l-L)^2(\cos[Bl] + \cosh[Bl])) - \\ & 4B^3(l-L)^3(\sin[Bl] - \sinh[Bl])) - 6B(-4B^3(l-L)^3\gamma\sin[Bl] - 6((2 + \\ & B^2(l-L)^2)\gamma\cos[Bl] + 2(-\gamma + (l-L)\cot[\theta] + \sin[\theta]))) \end{aligned}$$

$$\begin{aligned} D_{11} = & 2B(12 + B^4l^4 - 4B^4l^3L + 6B^4l^2L^2 - 4B^4lL^3 + B^4L^4 + \cosh[Bl]((-12 + \\ & B^4(l-L)^4)\cos[Bl] - 4B(3 + B^2(l-L)^2)(l-L)\sin[Bl]) - 4B(l-L)((-3 + \\ & B^2(l-L)^2)\cos[Bl] + 3B(-l + L)\sin[Bl])\sinh[Bl]) \end{aligned}$$

$$\begin{aligned} D_{21} = & -24B(12 + B^4l^4 - 4B^4l^3L + 6B^4l^2L^2 - 4B^4lL^3 + B^4L^4 + \cosh[Bl]((-12 + \\ & B^4(l-L)^4)\cos[Bl] - 4B(3 + B^2(l-L)^2)(l-L)\sin[Bl]) - 4B(l-L)((-3 + \\ & B^2(l-L)^2)\cos[Bl] + 3B(-l + L)\sin[Bl])\sinh[Bl]) \end{aligned}$$

$$\begin{aligned} N_{12} = & -4B^2L(B(-2Bl\gamma + 2BL\gamma + 2B(l-L)\gamma\cos[Bl] + B(l-L)^2\cot[\theta] - \\ & 2\gamma\sin[Bl] + B^2l^2\gamma\sin[Bl] - 2B^2lL\gamma\sin[Bl] + B^2L^2\gamma\sin[Bl] + 2Bl\sin[\theta] - \\ & 2BL\sin[\theta]) + B\cosh[Bl](2(B(l-L)\gamma + \sin[Bl](\gamma + (-l + L)\cot[\theta] - \sin[\theta]))) + \\ & B(l-L)\cos[Bl]((l-L)\cot[\theta] + 2(-\gamma + \sin[\theta]))) - (B(2 + B^2(l-L)^2)\gamma - \\ & 2\cot[\theta]\sin[Bl] - 2B\cos[Bl](\gamma + (-l + L)\cot[\theta] - \sin[\theta]))\sinh[Bl]) \end{aligned}$$

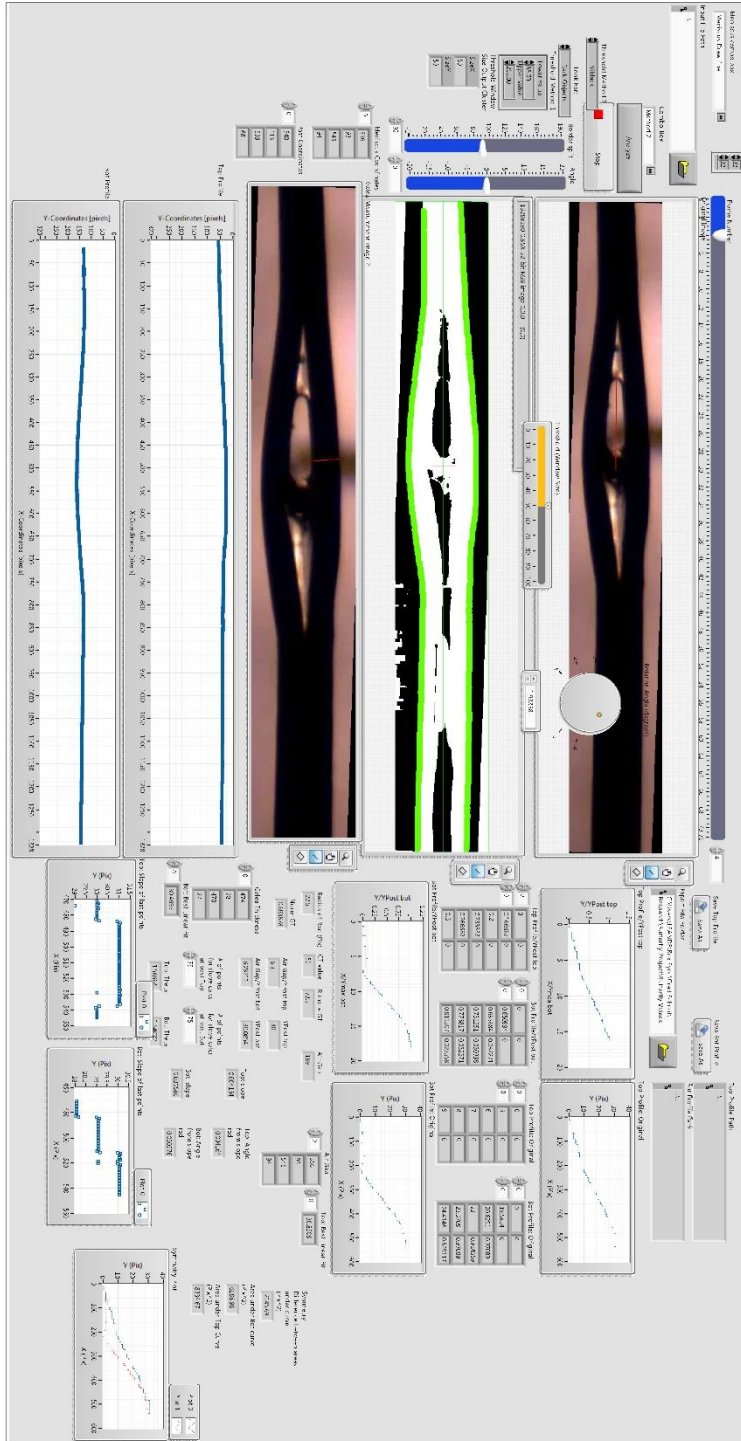
$$\begin{aligned} N_{22} = & -2B^2(B(-2Bl\gamma + 2BL\gamma + 2B(l-L)\gamma\cos[Bl] + B(l-L)^2\cot[\theta] - \\ & 2\gamma\sin[Bl] + B^2l^2\gamma\sin[Bl] - 2B^2lL\gamma\sin[Bl] + B^2L^2\gamma\sin[Bl] + 2Bl\sin[\theta] - \\ & 2BL\sin[\theta]) + B\cosh[Bl](2(B(l-L)\gamma + \sin[Bl](\gamma + (-l + L)\cot[\theta] - \sin[\theta]))) + \\ & B(l-L)\cos[Bl]((l-L)\cot[\theta] + 2(-\gamma + \sin[\theta]))) - (B(2 + B^2(l-L)^2)\gamma - \\ & 2\cot[\theta]\sin[Bl] - 2B\cos[Bl](\gamma + (-l + L)\cot[\theta] - \sin[\theta]))\sinh[Bl]) \end{aligned}$$

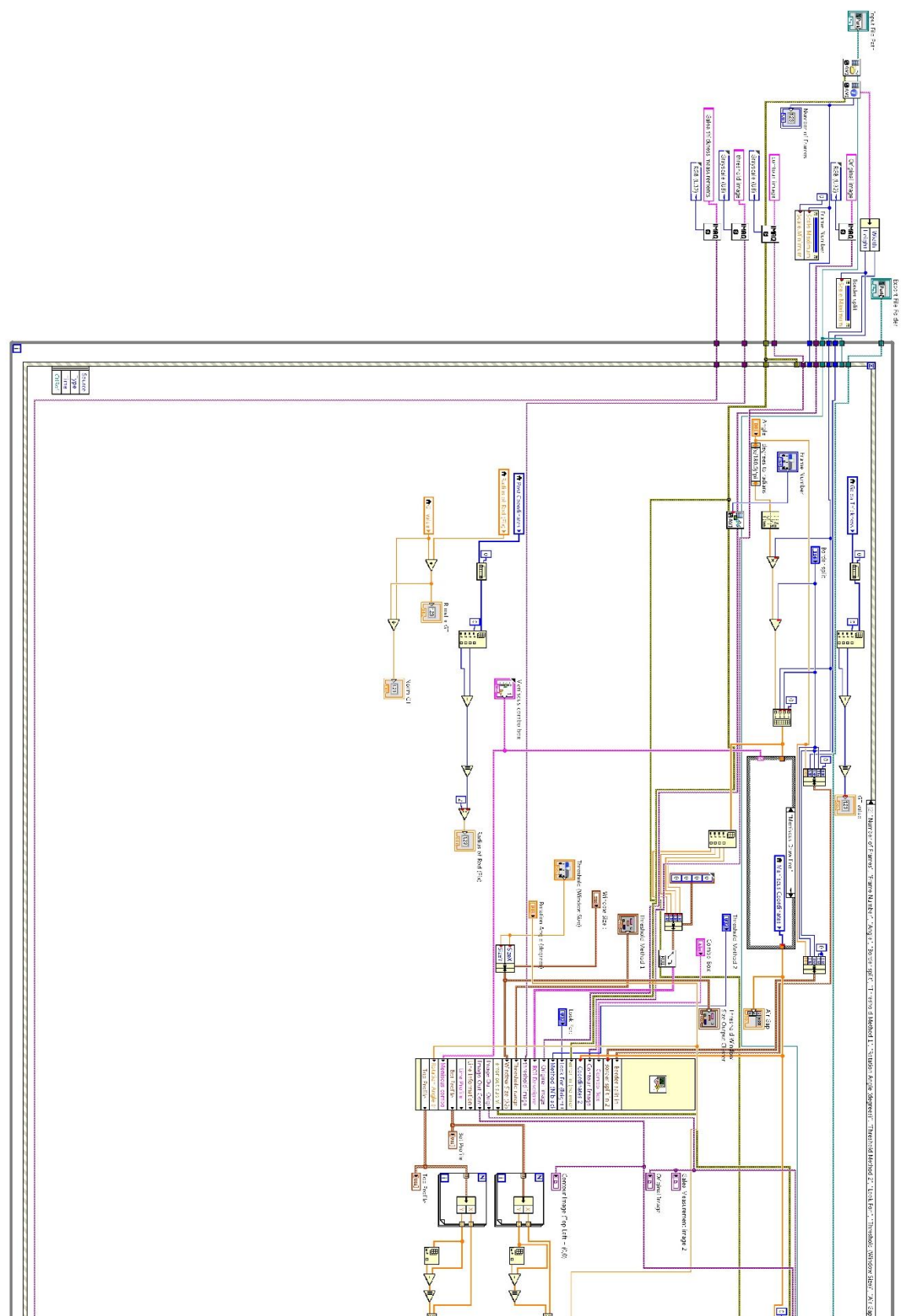
$$\begin{aligned}
N_{32} = & 2B(B(3(-2 + B^2(l^2 - L^2))\gamma \cos[Bl] + B(B(l - L)^2(2l + L)\cot[\theta] + (B^2l^3 + \\
& 2B^2L^3 - 3l(2 + B^2L^2))\gamma \sin[Bl] + 3B(l^2 - L^2)(-\gamma + \sin[\theta]))) + \cosh[Bl](3B(2 + \\
& B^2(l^2 - L^2))\gamma - 6\sin[Bl]((1 + B^2l(l - L))\cot[\theta] + B^2l(-\gamma + \sin[\theta])) - \frac{1}{2}B^3(l - \\
& L)\cos[Bl]\csc[\theta](2(-2l^2 + ll + L^2)\cos[\theta] - 6(l + L)\sin[\theta](-\gamma + \sin[\theta]))) - \\
& (B(B(B^2l^3 + 2B^2L^3 + l(6 - 3B^2L^2))\gamma + 6\sin[Bl](\gamma + (-2l + L)\cot[\theta] - \sin[\theta])) + \\
& 6\cos[Bl]((-1 + B^2l(l - L))\cot[\theta] + B^2l(-\gamma + \sin[\theta])))\sinh[Bl])
\end{aligned}$$

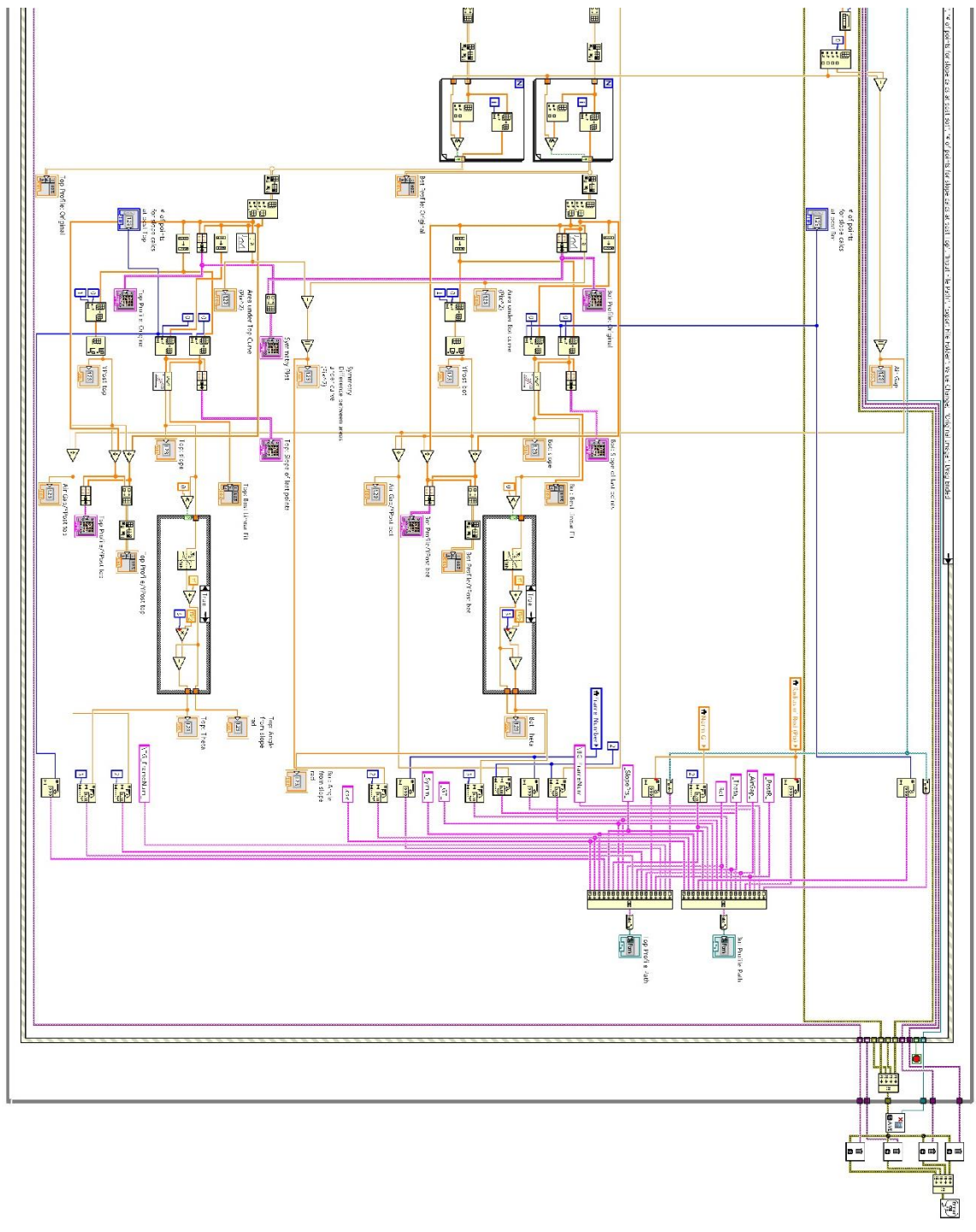
$$\begin{aligned}
D_{12} = & 2(12 + B^4l^4 - 4B^4l^3L + 6B^4l^2L^2 - 4B^4lL^3 + B^4L^4 + \cosh[Bl]((-12 + \\
& B^4(l - L)^4)\cos[Bl] - 4B(3 + B^2(l - L)^2)(l - L)\sin[Bl]) - 4B(l - L)((-3 + \\
& B^2(l - L)^2)\cos[Bl] + 3B(-l + L)\sin[Bl])\sinh[Bl])
\end{aligned}$$

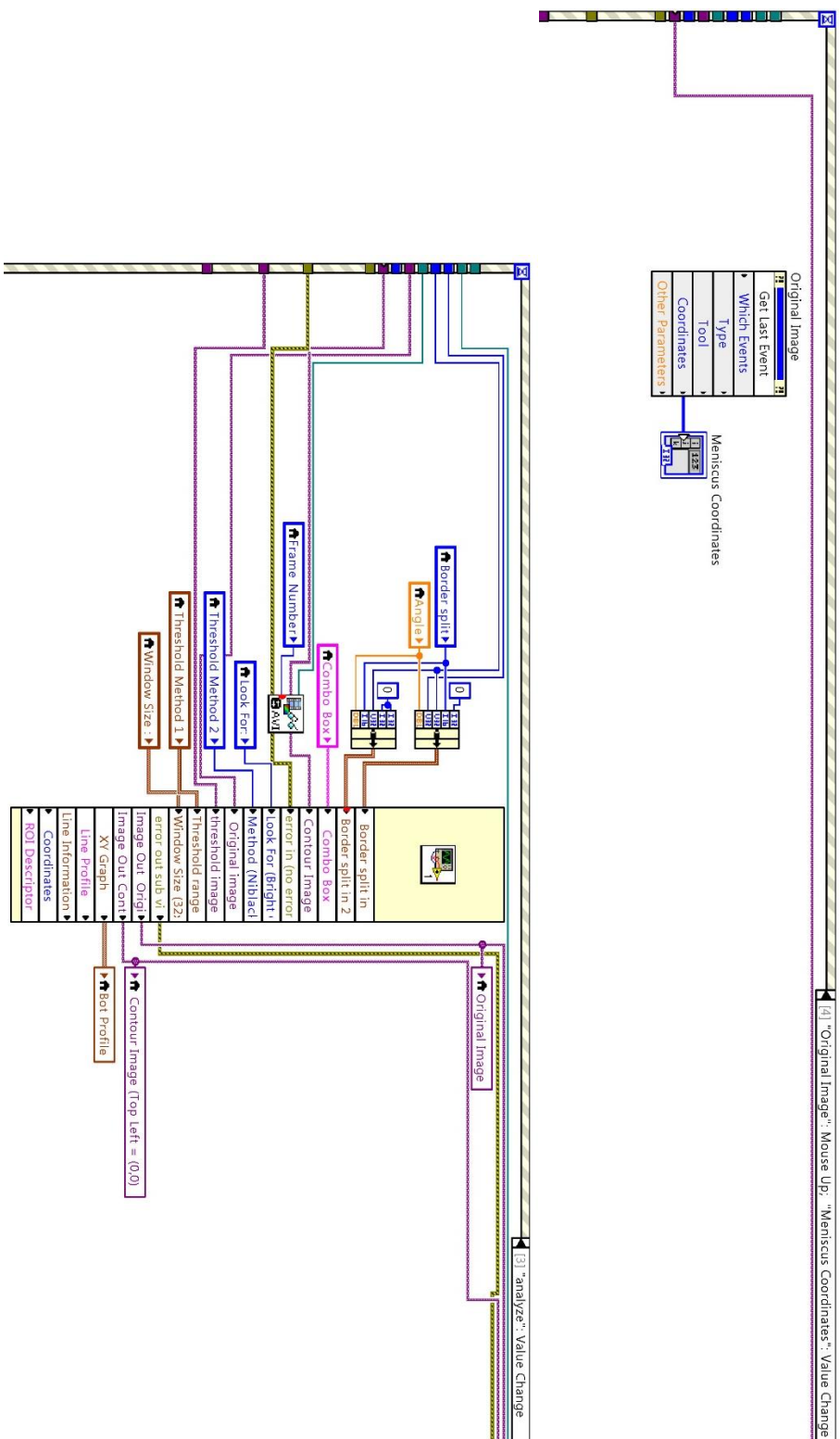
Appendix F

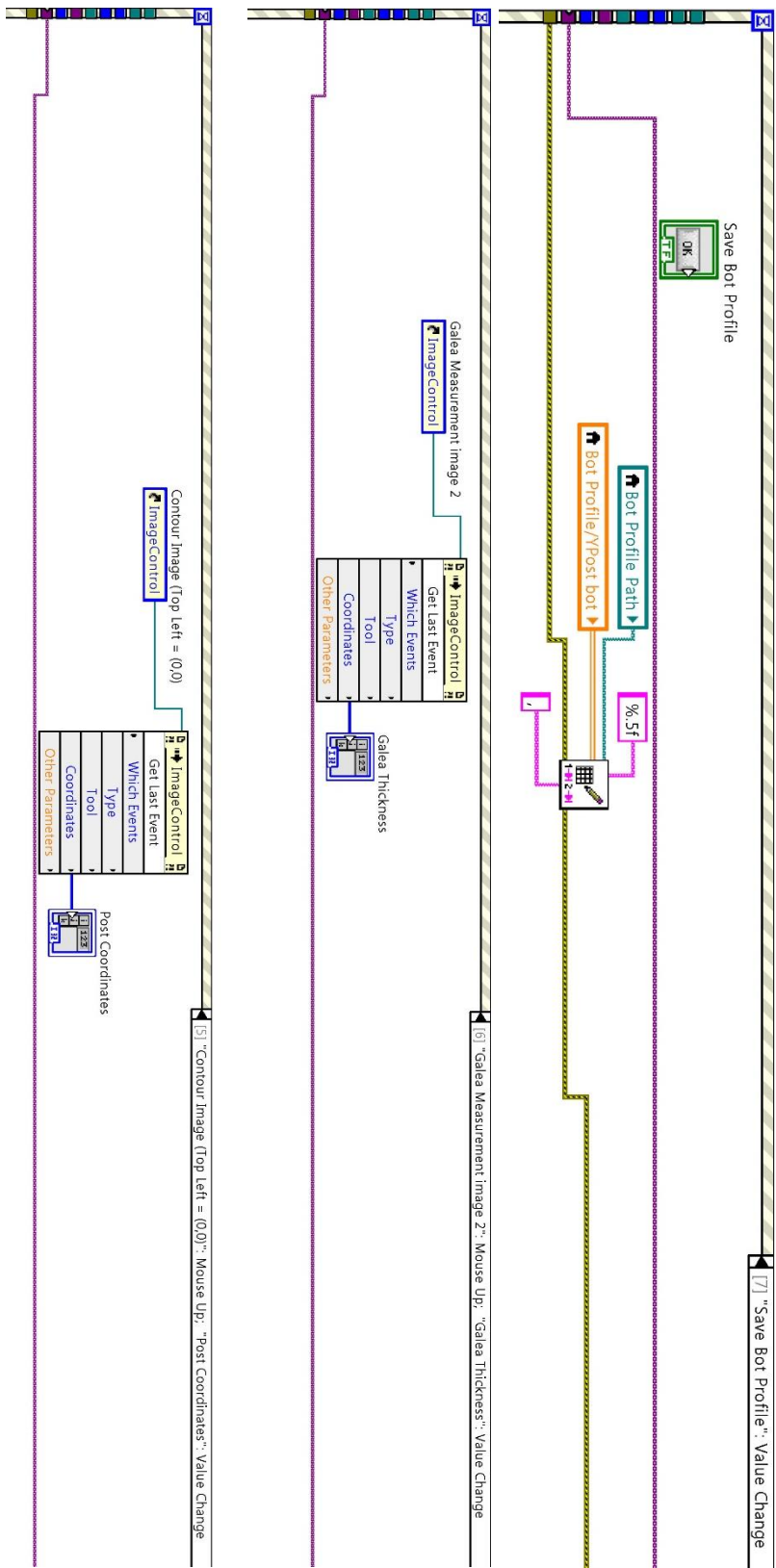
National Instruments LabVIEW® Code

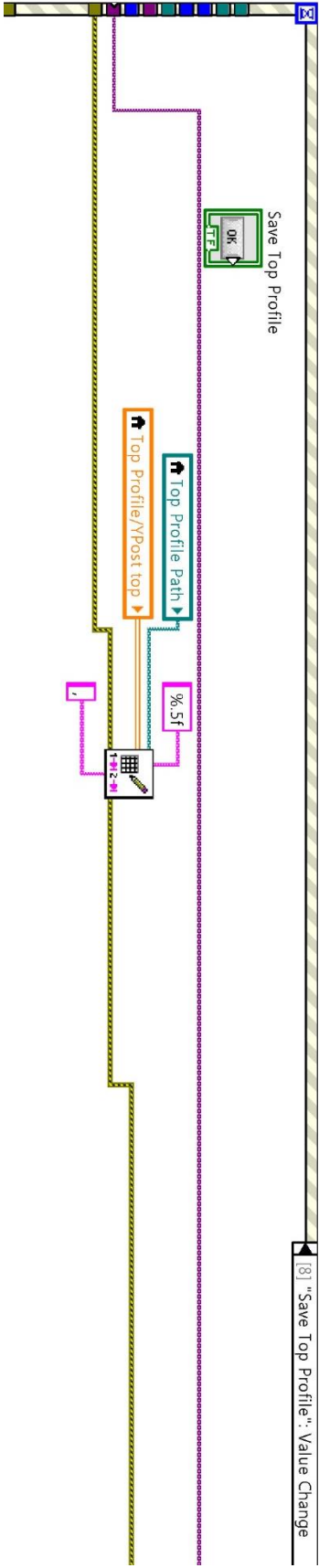












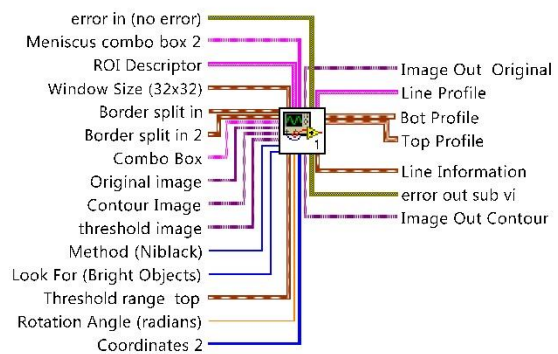
newsbVI_rotation.vi

C:\Users\LSANDE\Box Sync\Grad School\Research\Butterfly\Labview Codes\newsbVI_rotation.vi

Last modified on 4/3/2017 at 5:32 PM

Printed on 12/4/2017 at 12:04 PM

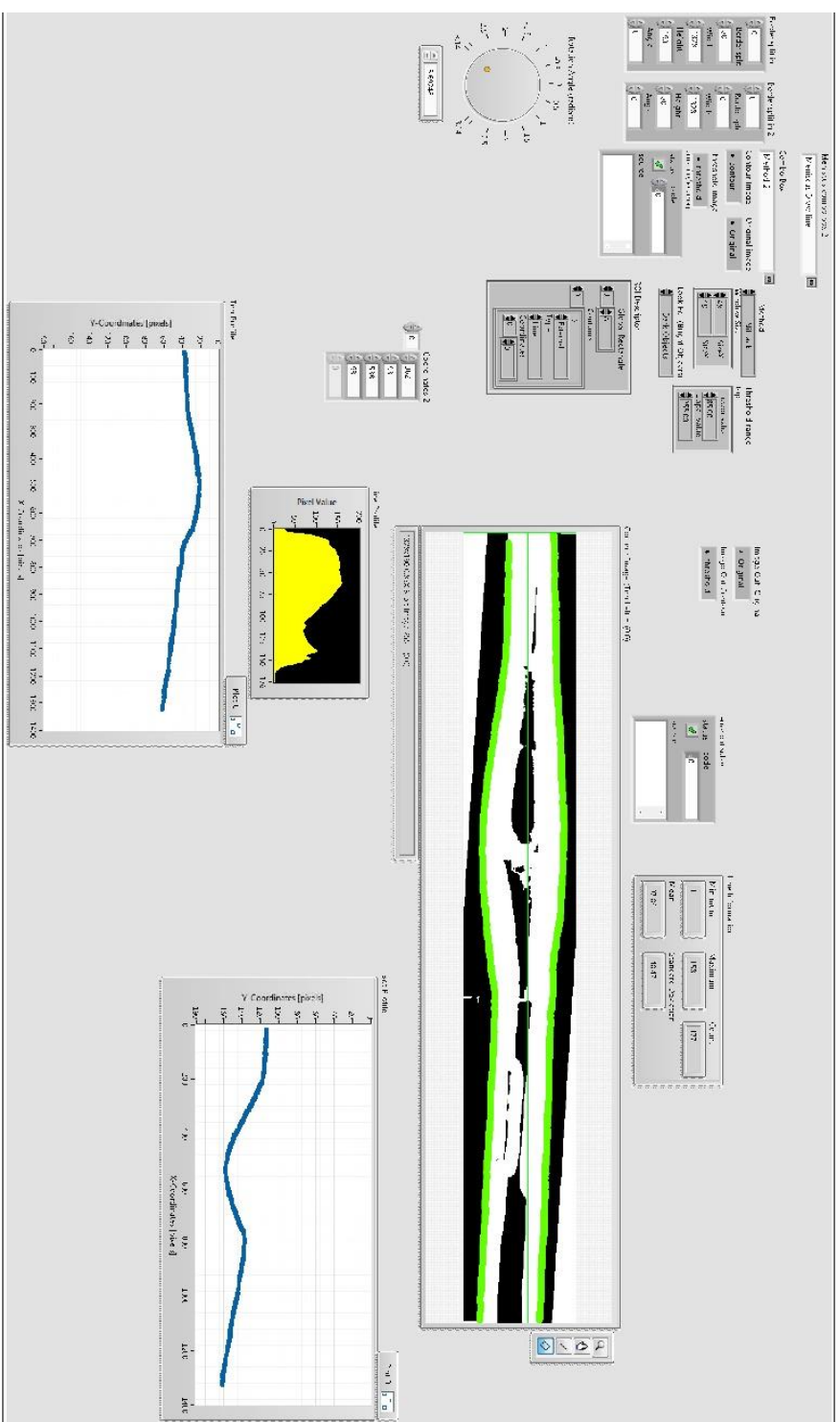
newsbVI_rotation.vi



newsbvI_rotation.vi

C:\Users\LSANDE\Box Sync\Grad School\Research\Butterfly\Labview Codes\newsuubi_rotation.vi

Printed on 12/4/2017 at 12:04 PM

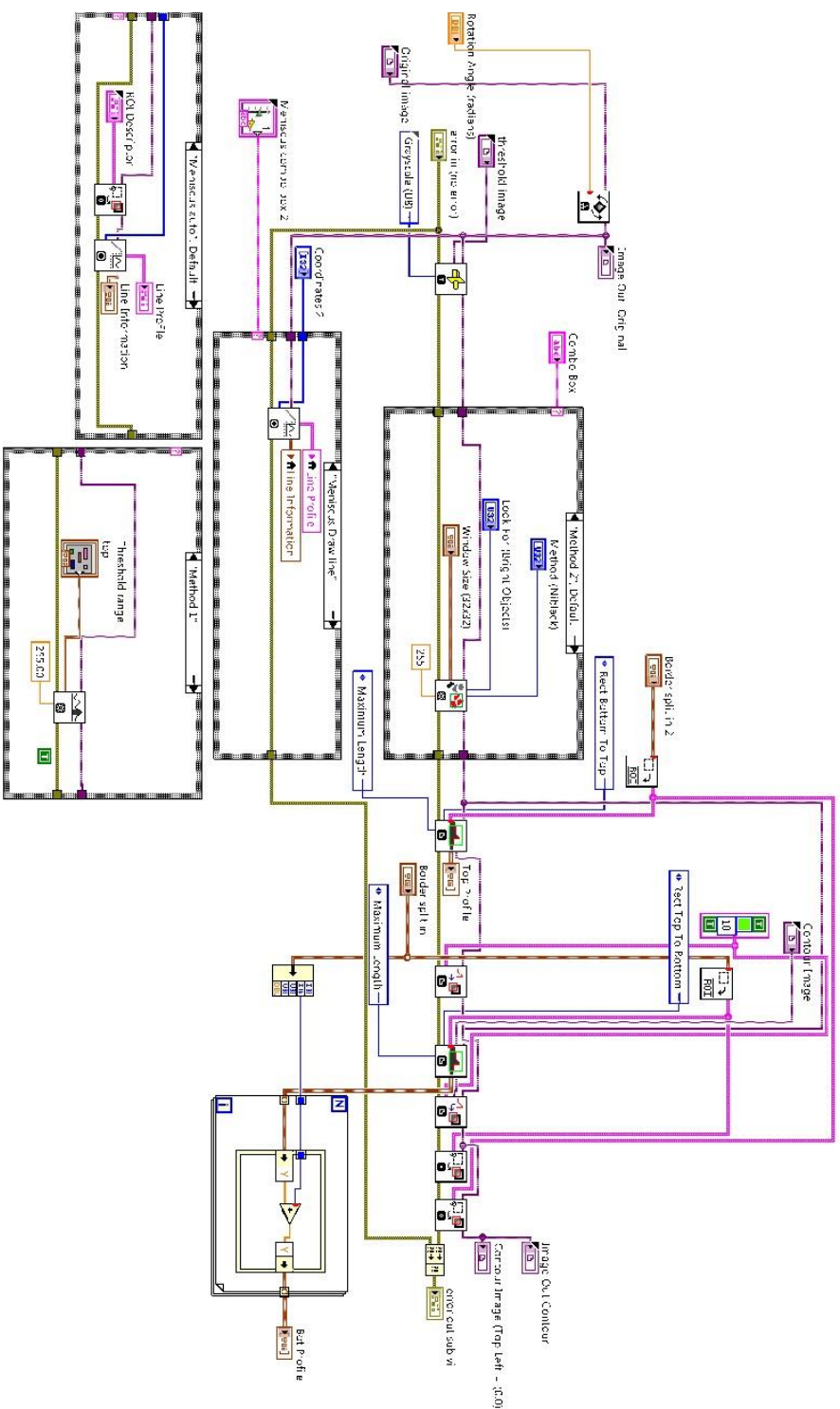


newsbvI_rotation.vi

C:\Users\LSANDE\Box Sync\Grad School\Butterfly\Labview Codes\newsbvt_rotation.vi

Last modified on 4/3/2017 at 5:32 PM

Printed on 12/4/2017 at 12:04 PM



REFERENCES

1. Kendall K. Molecular Adhesion and Its Applications: The Sticky Universe. New York: Kluwer Academic/Plenum Publishers; 2001.
2. K.R. S. Contact mechanics and the adhesion of soft solids. *Materials Science and Engineering R*. 2002;36:1-45.
3. Kinloch AJ, Williams JG. The mechanics of peel tests. 2002:273-301.
4. Kaelble DH. Theory and Analysis of Peel Adhesion: Mechanisms and Mechanics. *Transactions of the Society of Rheology*. 1959;3(1):161-80.
5. Bikerman JJ. Theory of Peeling through a Hookean Solid. *Journal of Applied Physics*. 1957;28(12).
6. Crocombe AD, Adams RD. Peel Analysis Using the Finite Element Method. *The Journal of Adhesion*. 1981;12(2):127-39.
7. Thouless MD, Jensen HM. Elastic Fracture Mechanics of the Peel-Test Geometry. *The Journal of Adhesion*. 1992;38(3-4):185-97.
8. Gibson RF. A review of recent research on mechanics of multifunctional composite materials and structures. *Composite Structures*. 2010;92(12):2793-810.
9. Zhandarov S. Characterization of fiber/matrix interface strength: applicability of different tests, approaches and parameters. *Compos Sci Technol*. 2005;65(1):149-60.
10. Hoecker F, Karger-Kocsis J. Effects of the interface on the mechanical response of CF/EP microcomposites and macrocomposites. *Composites*. 1994;25(7):729-38.
11. Hoecker F, Friedrich K, Blumberg H, Karger-Koscis J. Effects of fiber/matrix adhesion on off-axis mechanical response in carbon-fiber/epoxy-resin composites. *Compos Sci Technol*. 1995;54:317-27.
12. López-Buendía AM, Romero-Sánchez MD, Climent V, Guillem C. Surface treated polypropylene (PP) fibres for reinforced concrete. *Cement and Concrete Research*. 2013;54:29-35.
13. Chandra R, Singh SP, Gubta K. Damping studies in fiber-reinforced composites - a review. *Composite Structures*. 1999;46:41-51.
14. Lawcock GD, Ye L, Mai YW, Sun CT. Effects of fiber/matrix adhesion on carbon-fiber-reinforced metal laminates -- II. Impact behaviour. *Compos Sci Technol*. 1997;57:1621-8.
15. Effect of High Modulus Polyethylene Fibre Surface Treatment on Epoxy Resin Composite Impact Properties.
16. Sun L, Gibson RF, Gordaninejad F, Suhr J. Energy absorption capability of nanocomposites: A review. *Compos Sci Technol*. 2009;69(14):2392-409.
17. Tehrani M, Safdari M, Boroujeni AY, Razavi Z, Case SW, Dahmen K, et al. Hybrid carbon fiber/carbon nanotube composites for structural damping applications. *Nanotechnology*. 2013;24(15):155704.
18. Rajoria H, Jalili N. Passive vibration damping enhancement using carbon nanotube-epoxy reinforced composites. *Compos Sci Technol*. 2005;65(14):2079-93.
19. Gibson RF, Chen Y, Zhao H. Improvement of Vibration Damping Capacity and Fracture Toughness in Composite Laminates by the Use of Polymeric Interleaves. *Journal of Engineering Materials and Technology*. 2001;123(3):309.

20. Gottardo L, Hufenus R, Dressler M, Heuberger M. Design and development of liquid filled polymeric fibers with flexure rate viscoelastic properties. *Aip Conf Proc.* 2014;1593:60-3.
21. Khan SU, Li CY, Siddiqui NA, Kim J-K. Vibration damping characteristics of carbon fiber-reinforced composites containing multi-walled carbon nanotubes. *Compos Sci Technol.* 2011;71(12):1486-94.
22. Rao V, Herrera-Franco P, Ozzello AD, Drzal LT. A direct comparison of the fragmentation test and the microbond pull-out test for determining the interfacial shear strength. *J Adhes.* 1991;34:65-77.
23. Hassoune-Rhabbour B, Poussines L, Nassiet V. Development of an Adhesion Test for Characterizing the Interface Fiber/Polymer Matrix. *Key Engineering Materials.* 2012;498:210-8.
24. Ostrowicki GT, Sitaraman SK. Magnetically actuated peel test for thin films. *Thin Solid Films.* 2012;520(11):3987-93.
25. Vanwalleghem J, De Baere I, Huysman S, Lapeire L, Verbeken K, Nila A, et al. Effective use of transient vibration damping results for non-destructive measurements of fibre-matrix adhesion of fibre-reinforced flax and carbon composites. *Polymer Testing.* 2016;55:269-77.
26. Wu HF, Gu W, Lu G-Q, Kampe SL. Non-destructive characterization of fibre-matrix adhesion in composites by vibration damping. *Journal of Materials Science.* 1997;32(7):1795-8.
27. M. N, Chen EJJ. Review of Methods for Characterization of Interfacial Fiber-Matrix Interactions. *Polymer Composites.* 1988;9(4):245-51.
28. Eitner U, Rendler LC. The Mechanical Theory behind the Peel Test. *Energy Procedia.* 2014;55:331-5.
29. Brown HR, Yang ACM. The use of peel tests to examine the self adhesion of polyimide films. *Journal of Adhesion Science and Technology.* 1991;6(3):333-46.
30. Jang J, Sung M, Han S, Yu W-R. Prediction of delamination of steel-polymer composites using cohesive zone model and peeling tests. *Composite Structures.* 2017;160:118-27.
31. Kinloch AJ, Lau CC, Williams JG. The peeling of flexible laminates. *International Journal of Fracture.* 1994;66:45-70.
32. Zhang Y, Hazelton DW, Knoll AR, Duval JM, Brownsey P, Repnoy S, et al. Adhesion strength study of IBAD-MOCVD-based 2G HTS wire using a peel test. *Physica C: Superconductivity.* 2012;473:41-7.
33. Yang QD, Thouless MD, Ward SM. Analysis of the Symmetrical 90°-peel Test with Extensive Plastic Deformation. *The Journal of Adhesion.* 2006;72(2):115-32.
34. Krenn HW. Feeding mechanisms of adult Lepidoptera: structure, function, and evolution of the mouthparts. *Annu Rev Entomol.* 2010;55:307-27.
35. Lehnert MS, Monaenkova D, Andrukh T, Beard CE, Adler PH, Kornev KG. Hydrophobic-hydrophilic dichotomy of the butterfly proboscis. *J R Soc Interface.* 2013;10(85):20130336.
36. Krenn HW. Proboscis Morphology and Food Preferences in Nymphalid Butterflies (Lepidoptera: Nymphalidae). *The Zoological Society of London.* 2001;254:17-26.

37. Tsai CC, Mikes P, Andrukh T, White E, Monaenkova D, Burtovyy O, et al. Nanoporous artificial proboscis for probing minute amount of liquids. *Nanoscale*. 2011;3(11):4685-95.
38. Monaenkova D, Lehnert MS, Andrukh T, Beard CE, Rubin B, Tokarev A, et al. Butterfly proboscis: combining a drinking straw with a nanosponge facilitated diversification of feeding habits. *J R Soc Interface*. 2012;9(69):720-6.
39. Kingsolver JG, Daniel TL. Mechanics of Food Handling by Fluid-Feeding Insects. In: Chapman RF, de Boer G, editors. *Regulatory Mechanisms in Insect Feeding*. Boston, MA: Springer US; 1995. p. 32-73.
40. Krenn HW. Proboscis assembly in butterflies (Lepidoptera) - a once in a lifetime sequence of events. *Eur J Entomol*. 1996(94):495-501.
41. Hepburn HR. Proboscis Extension and Recoil in Lepidoptera. *Journal of Insect Physiology*. 1970;17:637-56.
42. Keis K, Kornev KG, Kamath YK, Neimark AV. Towards Fiber-Based Micro- and Nanofluidics. 2007. In: *Nanoengineered Nanofibrous Materials* [Internet].
43. Kornev KG, Adler PH. The Butterfly Proboscis as a Fiber-Based, Self-Cleaning Microfluidic System. *SPIE Newsroom*. 2014;4:6934.
44. Pometto S. Repair of the proboscis of brush-footed butterflies (lepidoptera: Nymphalidae). Tiger Prints: Clemson University; 2014.
45. Krenn HW, Kristensen NP. Evolution of proboscis musculature in lepidoptera. *Eur J Entomol*. 2004;101(4):565-75.
46. Liu J, Gong Y, Cao G. Chemical mediated elasto-capillarity of elastic sheets. *Soft Matter*. 2017.
47. Roman B, Bico J. Elasto-capillarity: deforming an elastic structure with a liquid droplet. *J Phys Condens Matter*. 2010;22(49):493101.
48. Bico J, Roman B, Moulin L, Boudaoud A. Elastocapillary coalescence in wet hair. *Nature Brief Communications*. 2004;432:690.
49. Monaenkova D, Andrukh T, Kornev KG. Bernoulli catenary and elasto-capillary effect in partially wet fibrous materials. *Textile Research Journal*. 2013;83(13):1386-97.
50. Hartog JPD. *Advanced Strength of Materials*: Dover Publications; 1987.
51. Landau LD, Lifshitz EM. *Theory of Elasticity*. 3 ed: Reed Educational and Professional Publishing Ltd.; 1986.
52. Timoshenko S, Goodier JN. *Theory of Elasticity*. 2 ed. United States: McGraw-Hill Book Company, Inc.; 1934. 35 p.
53. Kreyszig E. *Advanced Engineering Mathematics*. 10 ed: Wiley; 2011. 1280 p.
54. Obreimoff JW. The Splitting Strength of Mica. *J R Soc Interface*. 1930;127(805):290-7.
55. Pometto SF. Saliva Collection and Quantification from Adult Butterflies (Lepidoptera). *Entomological News*. 2015;124(5):305-9.
56. Capinera JL. *Encyclopedia of Entomology*. 2 ed: Springer Netherlands; 2008. 4346 p.
57. Scudder SH. *The Butterflies of the Eastern United States and Canada*. 1889;1.
58. Nicolas G. Immediate and Latent Effects of Carbon Dioxide on Insects. *Annu Rev Entomol*. 1989;34:97-116.

59. Quan C, Hu Z, Qian K, Li G, Xie H, Asundi AK, et al. Measurement of Young's modulus and Poisson's ratio of human hair using optical techniques. 2009;7522:75222Q.